Volume 66A
Number 5
Sept.–Oct. 1962

Physics and Chemistry

U.S. DEPARTMENT OF COMMERCE

SECTION A

JOURNAL OF RESEARCH

NATIONAL BUREAU OF STANDARDS

Journal of Research

of the

National Bureau of Standards

A. Physics and Chemistry

SEPT.–OCT. • 1962

VOLUME • 66A

NUMBER • 5

Editor: C. W. Beckett

Associate Editors: D. D. Wagman
J. M. Richardson

Publication dates:
Feb. 1, Apr. 1, June 1, Aug. 1, Oct. 1, Dec. 1, 1962.

JOURNAL OF RESEARCH

The National Bureau of Standards Journal of Research reports research and development in the fields of activity shown at right. Also included from time to time are survey articles on topics closely related to the Bureau's scientific and technical program.

The Journal is published in four separate sections as follows:

A. Physics and Chemistry

Contains papers of interest primarily to scientists working in these fields. Issued six times a year. Annual subscription: domestic, $4.00; foreign, $4.75.

B. Mathematics and Mathematical Physics

Presents studies and compilations designed mainly for the mathematician and the theoretical physicist. Issued quarterly. Annual subscription: domestic, $2.25; foreign, $2.75.

C. Engineering and Instrumentation

Reports research and development results of interest chiefly to the engineer and the applied scientist. Issued quarterly. Annual subscription: domestic, $2.25; foreign, $2.75.

D. Radio Propagation and Atmospheric Physics

Reports work in radio propagation, upper atmospheric physics, and communications. Issued six times a year. Annual subscription: domestic, $4.00; foreign, $4.75.

Functions and Activities

The functions of the National Bureau of Standards are set forth in the Act of Congress, March 3, 1901, as amended. These include the development and maintenance of the national standards of measurement and the provision of means and methods for making measurements consistent with these standards; the determination of physical constants and properties of materials; the development of methods and instruments for testing materials, devices, and structures; advisory services to government agencies on scientific and technical problems; invention and development of devices to serve special needs of the Government; and the development of standard practices, codes, and specifications. The work includes basic and applied research, development, engineering, instrumentation, testing, evaluation, calibration services, and various consultation and information services. The Bureau also serves as the Federal technical research center in a number of specialized fields. The scope of activities of the National Bureau of Standards is suggested in the following listing of the divisions and sections engaged in technical work.

Washington, D.C.

Electricity. Resistance and Reactance. Electrochemistry. Electrical Instruments. Magnetic Measurements. Dielectrics. High Voltage.

Metrology. Photometry and Colorimetry. Refractometry. Photographic Research. Length. Engineering Metrology. Mass and Scale. Volumetry and Densimetry.

Heat. Temperature Physics. Heat Measurements. Cryogenic Physics. Equation of State. Statistical Physics.

Radiation Physics. X-ray. Radioactivity. Radiation Theory. High Energy Radiation. Radiological Equipment. Nucleonic Instrumentation. Neutron Physics.

Analytical and Inorganic Chemistry. Pure Substances. Spectrochemistry. Solution Chemistry. Standard Reference Materials. Applied Analytical Research. Crystal Chemistry.

Mechanics. Sound. Pressure and Vacuum. Fluid Mechanics. Engineering Mechanics. Rheology. Combustion Controls.

Polymers. Macromolecules: Synthesis and Structure. Polymer Chemistry. Polymer Physics. Polymer Characterization. Polymer Evaluation and Testing. Applied Polymer Standards and Research. Dental Research.

Metallurgy. Engineering Metallurgy. Microscopy and Diffraction. Metal Reactions. Metal Physics. Electrolysis and Metal Deposition.

Inorganic Solids. Engineering Ceramics. Glass. Solid State Chemistry. Crystal Growth. Physical Properties. Crystallography.

Building Research. Structural Engineering. Fire Research. Mechanical Systems. Organic Building Materials. Codes and Safety Standards. Heat Transfer. Inorganic Building Materials. Metallic Building Materials.

Applied Mathematics. Numerical Analysis. Computation. Statistical Engineering. Mathematical Physics. Operations Research.

Data Processing Systems. Components and Techniques. Computer Technology. Measurements Automation. Engineering Applications. Systems Analysis.

Atomic Physics. Spectroscopy. Infrared Spectroscopy. Solid State Physics. Electron Physics. Atomic Physics.

Instrumentation. Engineering Electronics. Electron Devices. Electronic Instrumentation. Mechanical Instruments. Basic Instrumentation.

Physical Chemistry. Thermochemistry. Surface Chemistry. Organic Chemistry. Molecular Spectroscopy. Molecular Kinetics. Mass Spectrometry.

Office of Weights and Measures

Boulder, Colo.

Cryogenic Engineering Laboratory. Cryogenic Equipment. Cryogenic Processes. Properties of Materials. Cryogenic Technical Services.

Central Radio Propagation Laboratory

Ionosphere Research and Propagation. Low Frequency and Very Low Frequency Research. Ionosphere Research. Prediction Services. Sun-Earth Relationships. Field Engineering. Radio Warning Services. Vertical Soundings Research.

Radio Propagation Engineering. Data Reduction Instrumentation. Radio Noise. Tropospheric Measurements. Tropospheric Analysis. Propagation-Terrain Effects. Radio-Meteorology. Lower Atmosphere Physics.

Radio Systems. Applied Electromagnetic Theory. High Frequency and Very High Frequency Research. Modulation Research. Antenna Research. Navigation Systems.

Upper Atmosphere and Space Physics. Upper Atmosphere and Plasma Physics. Ionosphere and Exosphere Scatter. Airglow and Aurora. Ionospheric Radio Astronomy.

Radio Standards Laboratory

Radio Physics. Radio Broadcast Service. Radio and Microwave Materials. Atomic Frequency and Time-Interval Standards. Millimeter-Wave Research.

Circuit Standards. High Frequency Electrical Standards. Microwave Circuit Standards. Electronic Calibration Center.

U.S. DEPARTMENT OF COMMERCE
Luther H. Hodges, Secretary

NATIONAL BUREAU OF STANDARDS
A. V. Astin, Director

Order all publications from the Superintendent of Documents
U.S. Government Printing Office, Washington 25, D.C.

Use of funds for printing this publication approved by the Director of the Bureau of the Budget (June 19, 1961).

JOURNAL OF RESEARCH of the National Bureau of Standards—A. Physics and Chemistry
Vol. 66A, No. 5, September–October 1962

Calorimetric Calibration of an Ionization Chamber for Determination of X-ray Total Beam Energy*

John S. Pruitt and Steve R. Domen

(May 18, 1962)

An X-ray calorimeter has been used to determine the total energy transported by bremsstrahlung beams with maximum photon energies between 18.2 and 170 Mev. The measurements from two experiments have been used to calibrate an aluminum ionization chamber for routine determinations of total beam energy. The calibrations are compared with calibrations of the same chamber made with a scintillation spectrometer, and with calorimetric calibrations made in other laboratories.

1. Introduction

Several techniques for the determination of the energy transported by a high energy X-ray beam have been described in the literature [1].[1] The most direct method is calorimetry, which can be used to determine the total beam energy without reference to the energy spectrum of the incident photons and without knowledge of the details of the calorimeter energy absorption processes. High energy X-ray calorimeter measurements have been reported by several authors [2–5], and some of these measurements have been used to calibrate ionization chambers for routine determination of the total beam energy [3–5]. This paper is a description of an X-ray calorimeter and its use in two experiments to calibrate an aluminum ionization chamber. The determination of the fraction of energy escaping from the calorimeter is described in detail. Other calibrations of this same ionization chamber are reported and are shown to be in good agreement with the calibrations obtained in these experiments.

The first calorimeter experiment was performed with the NBS 50 Mev betatron, using bremsstrahlung beams with maximum photon energies between 18.2 and 42.1 Mev. The second experiment was performed with the NBS 180 Mev synchrotron, covering the energy range between 20 and 170 Mev. The results of these two experiments have been combined to yield average calibrations with an estimated uncertainty of the order of ± 2 percent between 20 and 170 Mev.

2. Calorimeter

Figure 1 is a schematic cross section of the X-ray calorimeter. The sensitive elements are the two cylinders, made of lead covered with thin gold-plated brass shells. The five concentric boxes and the thermoregulator provide a constant temperature environment for the cylinders, and precautions were taken to minimize heat exchange between the cylinders and the boxes. The highly polished gold surfaces of the cylinders and of box A, designed to minimize thermal radiation, are shown in figure 2. Exchange of energy by conduction and convection is practically eliminated by evacuating boxes A, B, and C and by mounting them, along with the cylinder, with thermally insulating plastics. The isolation of the sensitive elements is such that the thermal relaxation time of the cylinders is about 20 hr, almost an order of magnitude larger than the corresponding quantity reported for an earlier model [6].

Two 1,000 ohm bead thermistors with temperature coefficients of about -3.6 percent per °C and two 500 ohm carbon resistors are embedded in each cylinder. The four thermistors form the arms of a Wheatstone bridge, as shown in figure 3. Their characteristics are not identical, but the bridge can be balanced by adjusting the length of the small external manganin wire resistor, r. Bridge power is supplied by a 1.34 v mercury dry cell, and the output voltage between points a and b in the detection circuit is amplified by a breaker amplifier and displayed on a chart recorder. The circuit between amplifier and recorder adds a fixed d-c bias to the amplified signal to place the recorder pen at midscale when the amplifier input is shorted. This bias increases the average signal-to-noise ratio, for the noise was found to increase with increasing bridge unbalance.

The four carbon resistors are connected in two separate circuits, which can be used to heat the cylinders individually. The inner end of each resistor is in electrical contact with the cylinder, which forms an integral part of each circuit as shown by dashed lines in figure 3.

The detection circuit output voltage is proportional to the temperature difference between the two cylinders, and can be used as a relative measure of heat generated in one of the cylinders, if corrections are made for heat lost to the surroundings. Figure 4 shows a chart record which was obtained with maximum amplifier gain when the source of heat was a 25 Mev bremsstrahlung beam with a diameter of 4.2 cm and an intensity of 12 μw/cm^2. The absolute temperature changes in figure 4 are only approximate and are shown for illustrative purposes only. The temperature changes are normally measured in chart divisions, and are converted directly into energy units with the calibrations described below, after the change caused by irradiation has been corrected for the average drift during irradiation.

*Supported in part by AEC.
[1]Figures in brackets indicate the literature references at the end of this paper.

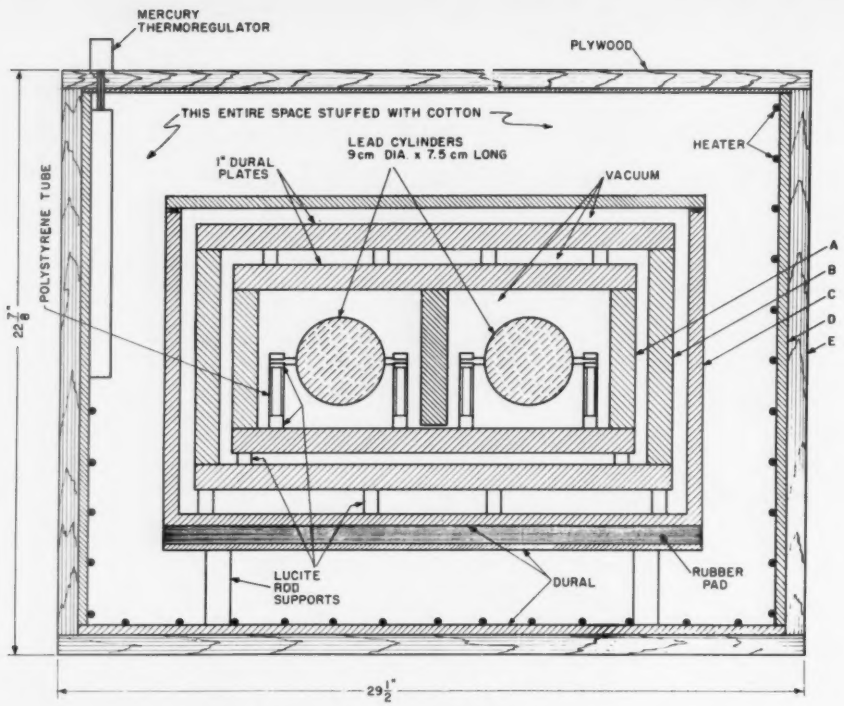

FIGURE 1. *Cross section of X-ray calorimeter.*

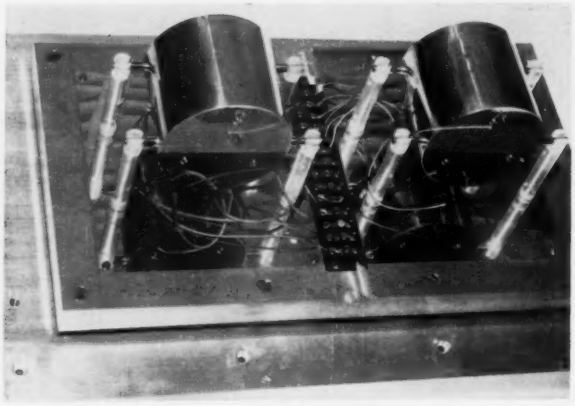

FIGURE 2. *Calorimeter cylinders mounted on base plate of inner box.*

The signal noise in figure 4 is typical for maximum gain operation and disappears when the amplifier input is shorted. The noise is less noticeable when a lower gain is used, which was feasible at higher energies where the available X-ray intensities were larger. This noise limits the precision of low energy calorimeter measurements, but these measurements are still reproducible with an rms deviation smaller than 4 percent even when the intensity is as low as 2 μw/cm^2.

The recorder pen was returned to the bottom of the chart after each exposure in preparation for the next run, by heating the dummy cylinder with the compensation circuit of figure 3. This was done in preference to adjusting the manganin wire, r, because the latter introduced spurious transients in the bridge output voltage which persisted for about 20 min, and also increased the drift correction for succeeding runs. The manganin wire was changed only at the start of each day, to minimize the initial recorder pen drift rate.

The vertical scale of the chart recorder was calibrated after each X-ray exposure, to minimize errors introduced by changes in amplifier gain and by the gradual increase of the cylinder temperatures during the course of a day. Calibration was performed by heating the previously irradiated cylinder electrically with a known power for a known time, using the calibration circuit of figure 3. The power supplied by this circuit is the product of the voltages V_R and V_C, which were both measured with a potentiometer, divided by the resistance of the precision wire wound resistor R. The net power dissipated in the cylinder was obtained by correcting for power lost in the cable (about 0.5%), heat conducted away from the cylinder by the heater and thermistor leads (0.1%), and heat radiated from the exposed ends of resistors R_3 and R_4 (0.1%). The power used for each calibration was preselected to approximate the X-ray power, to reduce the systematic errors. This preselection was done using the resistor R' in place of the cylinder.

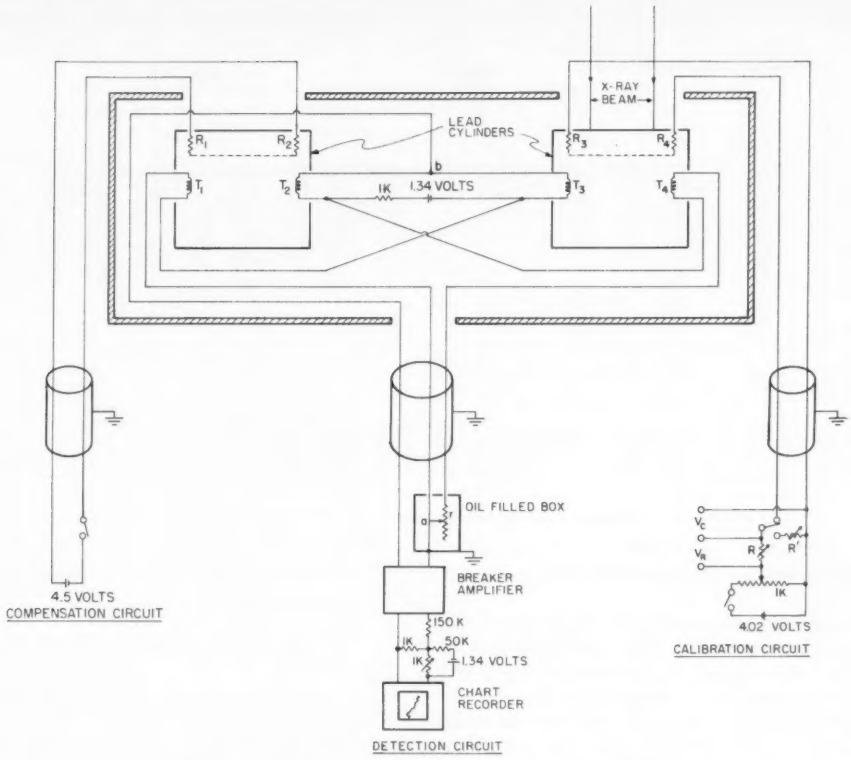

FIGURE 3. *Schematic diagram of calorimeter circuits.*

The R_i are carbon resistors and the T_i bead thermistors embedded in the calorimeter cylinders

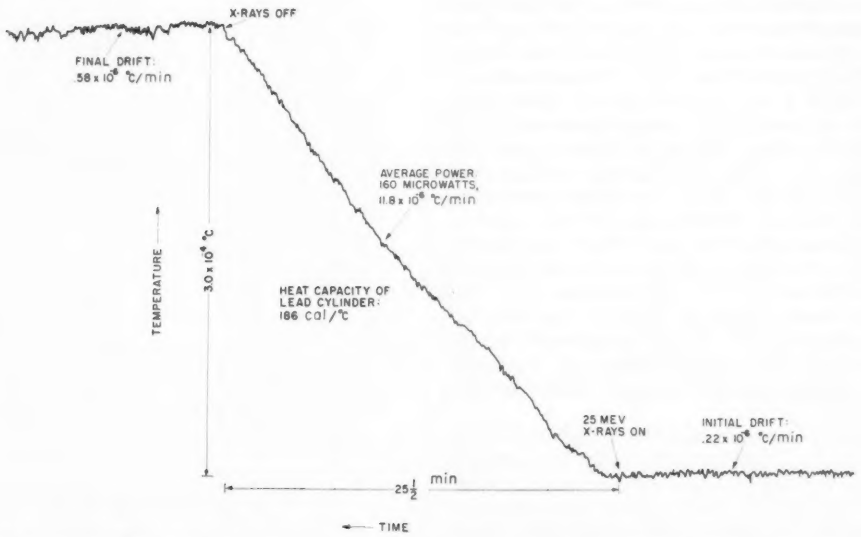

FIGURE 4. *Typical chart record of an exposure to 25 Mev X-rays, using maximum amplifier gain.*

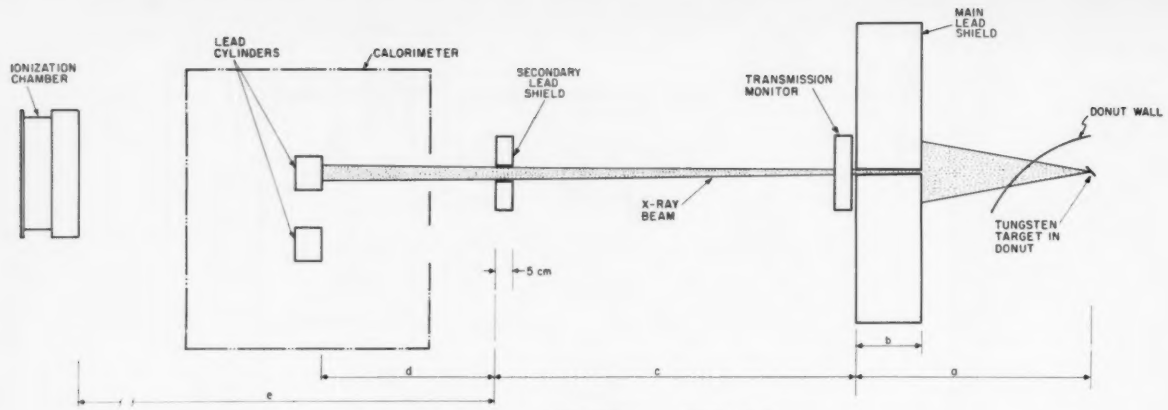

EXPERIMENT	DIMENSIONS, cm					ENERGY RANGE Mev
	a	b	c	d	e	
A	65	18	100	48	440	18.2 - 42.1
B	184	30	103	39	507	20 - 170

FIGURE 5. *Experimental arrangement for the two calorimeter experiments.*

3. Calorimeter Measurements

Figure 5 is a generalized schematic diagram of the experimental arrangements in the two calorimeter experiments. In experiment A, performed with the betatron, the bremsstrahlung beam was filtered by 1.6 g/cm² of porcelain in the wall of the electron acceleration chamber (the donut), and by 1.4 g/cm² of aluminum in transmission monitor A. In experiment B, performed with the synchrotron, the filters were 4.1 g/cm² of Pyrex in the donut wall and 0.4 g/cm² of aluminum in monitor B. In each experiment, the main lead shield was chosen to produce a 4.2 cm diam beam at the calorimeter cylinder face, and the secondary lead shield was placed so that it could absorb extra-beam electrons and photons generated by interactions in the main shield and the monitor, without interfering with the direct beam.

Both transmission monitors were ionization chambers. Their stability was periodically checked, with the calorimeter removed, by comparison with the large ionization chamber shown in figure 5 and discussed in section 5. The total charge collected in each chamber during an X-ray exposure was measured in volts with a Townsend balance circuit, using a polystyrene capacitor to collect the charge, a potentiometer to supply and measure the bucking voltage, and a vibrating reed electrometer as a null detector. The measurements were all corrected to an air temperature of 20° C and a pressure of 760 mm of mercury. The small effect of humidity changes was eliminated by using a drier in each chamber.

The calorimeter measurements at different peak photon energies, k_{max}, are listed in table 1 in units of joules absorbed by the calorimeter per monitor-volt. The rms deviations of these measurements vary from ±3.6 percent at an intensity of 2μw/cm², which required 90 min exposures with maximum amplifier gain, to ±0.7 percent at an intensity of 250μw/cm², which required 5 min exposures with the gain reduced by a factor of 7.

4. Calorimeter Corrections

The calibrations of monitors A and B were determined in joules/monitor-volt by correcting the numbers in table 1 for the fraction of incident energy which did not contribute to the calorimeter cylinder temperature rise. Part of this energy is removed from the incident beam by the calorimeter entrance foils, part is lost in nuclear transformations in the cylinder, and part escapes from the cylinder in the form of transmitted and scattered

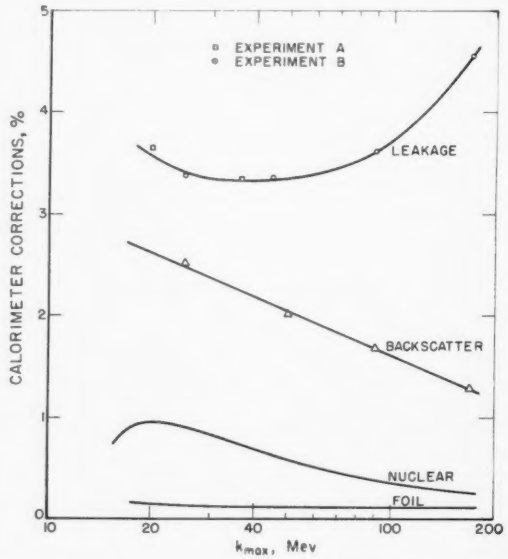

FIGURE 6. *Corrections for energy which does not appear as heat in the calorimeter.*

TABLE 1. *Calorimeter measurements of joules absorbed/monitor volt, at 20 °C and 760 mm of mercury*

k_{max} (Mev)	Experiment A							Experiment B												
	18.2	19.8	21.7	25.9	31.3	36.7	42.1	20	25	30	35	40	45	50	60	70	90	110	130	150	170
Individual measurements	0.1360	0.1463	0.1552	0.1671	0.1943	0.2169	0.2350	0.467	0.590	0.698	0.799	0.892	0.961	1.052	1.200	1.387	1.632	1.825	2.047	2.219	2.383
	.1399	.1489	.1534	.1710	.1945	.2161	.2368	.500	.572	.703	.820	.906	.957	1.087	1.198	1.361	1.677	1.821	2.044	2.214	2.374
	.1381	.1513	.1620	.1725	.1976	.2140	.2431	.490	.591	.688	.790	.861	.984	1.050	1.221	1.371	1.588	1.835	2.038	2.193	2.366
	.1341	.1417	.1604	.1726	.1993	.2181	.2374	.455	.550	.700	.809	.901	.976	1.051	1.221	1.358	1.587	1.899	2.028	2.217	2.373
	.1417	.1527	.1577	.1733	.1951	.2189	.2363	.498	.611	.710	.788	.884	.976	1.070	1.206	1.354	1.622	1.893	2.036	2.207	2.380
	.1327	.1485	.1560	.1725	.1924	.2165	.2390	.464	.605	.719	.792	.887	.966	1.065	1.232	1.288	1.579	1.820	2.026	2.202	2.364
	.1326	.1426	.1526	.1734	.1967	.2178	.2387	.491	.555	.683	.800	.883	.980	1.061	1.233	1.305	1.584	1.844	2.018	2.187	2.324
	.1365	.1388	.1548	.1771	.1957	.2118	.2382	.490	.564	.664	.797	.855	.981	1.068	1.214	1.281	1.596	1.831	2.010	2.180	2.342
	.1397	.1500	.1559		.1984	.2161	.2363	.449	.557	.704	.801	.900	.968	1.058	1.225	1.283	1.583		2.014	2.167	2.348
						.2138		.483	.569	.700	.799	.901	.967	1.061	1.223	1.376	1.580		2.003	2.197	
								.455	.602	.705	.782	.894	.966	1.048		1.363	1.530				
								.468	.584	.695	.810	.889	.975	1.051		1.358	1.616				
								.480	.600	.687	.804	.877				1.353	1.612				
									.592	.692						1.362	1.626				
									.579							1.354					
																1.365					
																1.377					
																1.364					
Averages	.1366	.1467	.1564	.1724	.1960	.2160	.2379	.476	.581	.696	.799	.887	.971	1.060	1.217	1.348	1.601	1.846	2.026	2.198	2.362
Deviations, Percent rms.	2.3	3.2	2.0	1.6	1.1	1.0	1.0	3.6	3.3	1.9	1.3	1.7	0.9	1.0	1.0	2.5	2.1	1.7	0.7	0.8	0.8

TABLE 2. *Absolute calorimetric calibration of P2–4 at 20 °C and 760 mm of mercury in a 4.2 cm diam beam filtered by 4.5 g/cm² of aluminum*

Experiment A

k_{max}	*Joules* / mon. volt	*P2–4 volts* / mon. volt	F_A	Cal(P2–4)
Mev				*Joules/coulomb*
18.2	0.1472	3.442	0.998	4.19×10^{8}
19.8	.1579	3.693	.998	4.18
21.7	.1680	3.941	.998	4.17
25.9	.1848	4.361	.998	4.15
31.3	.2094	4.962	.999	4.13
36.7	.2305	5.495	.999	4.11
42.1	.2536	6.002	.999	4.14

Experiment B

20	0.512	12.20	1	4.12×10^{8}
25	.623	14.97	1	4.08
30	.744	17.74	1	4.11
35	.853	20.38	1	4.10
40	.946	22.88	1	4.05
45	1.034	25.25	1	4.02
50	1.128	27.70	1	3.99
60	1.293	32.18	1	3.94
70	1.431	36.31	1	3.86
90	1.696	43.80	1	3.80
110	1.956	50.00	1	3.84
130	2.151	55.39	1	3.81
150	2.336	59.90	1	3.82
170	2.513	63.73	1	3.87

Average

k_{max}	Cal(P2–4)	Percent error	
		sdm	Total
Mev	*Joules/coulomb*		
20	4.16×10^{8}	0.5	2.1
26	4.11	.6	2.4
31	4.12	.3	1.5
36	4.11	.2	1.2
41	4.09	.4	1.8
45	4.02	.3	1.5
50	3.99	.3	1.5
60	3.94	.3	1.5
70	3.86	.6	2.4
90	3.80	.6	2.4
110	3.84	.6	2.4
130	3.81	.2	1.2
150	3.82	.3	1.5
170	3.87	.3	1.5

photons and secondary electrons.[2] The determination of these corrections is described below, and the corrections are plotted in figure 6 as a function of bremsstrahlung peak photon energy. The corrected monitor calibrations are listed in table 2 for both experiments.

4.1. Calculated Corrections

The energy removed by the calorimeter entrance foils and by nuclear transformations was calculated as a function of photon energy and averaged over the bremsstrahlung spectra obtained from the tabulations of reference [8], corrected for filtration with the total attenuation coefficients of reference [9].

The probability of an interaction in the foils which removed a photon of energy k from the beam incident on the calorimeter cylinder was taken to be $\frac{1}{2}\alpha(k)t$, where t is the total foil thickness (0.1 g/cm² of aluminum), and $\alpha(k)$ is the total attenuation coefficient of aluminum [9]. The factor $\frac{1}{2}$ represents an estimate of the probability that the interaction products will not strike the cylinder. The foil correction is so small that large errors in this estimate are unimportant.

Only (γ,n) reactions were considered in calculating the nuclear correction since (γ,p) reactions are much less probable. The probability for a (γ,n) reaction was taken as the triple product of the atomic density of lead (2.91×10^{21} atoms/g), the reaction cross section (cm²) and the effective length of the cylinder (g/cm²). The cross section was taken from reference [10] below 18 Mev and from reference [11] at higher

[2] The amount of energy stored by the lead crystal when lead atoms are displaced to interstitial sites by X-rays and secondary electrons in the cylinder can be shown to be negligible: The cross section for atomic displacement in lead is of the order of 3×10^{-24} cm² for X-rays and 10^{-22} cm² for electrons, and each displaced atom will in turn displace no more than five additional atoms [7]. Each displacement results in the storage of less than 25 ev. In traveling one mean-free path, an X-ray of any energy loses no more than 0.002 percent of its energy to the crystal. The energy lost to the crystal by an electron, in traveling 1 cm, is less than 0.005 percent of the normal energy loss rate at all energies.

energies. The effective length of the cylinder is $(1-e^{-\beta L})/\beta$, where L is the true length and β is an attenuation coefficient describing the decrease of beam intensity with increasing depth in the cylinder. In the initial calculations, β was taken from tabulations of total attenuation coefficients [9], which underestimate the effective length because their use assumes that all interaction products are removed from the beam. In a second set of calculations, an average β was taken from the slope of experimental transition curves discussed in the following section (fig. 9). These β overestimate the effective length because they are close to the attenuation coefficient for minimum absorption, which occurs at about 4 Mev in lead. The average photon energy for (γ,n) reactions is larger than this and the average β should also be larger. However, at each energy, the fraction of energy lost to (γ,n) reactions predicted by these two sets of β's differed by less than ¼ percent and the average effective length was used in the final calculations.

The amount of energy removed from the incident beam by a (γ,n) reaction was taken to be the neutron binding energy in lead, 7.9 Mev [10], plus an average neutron kinetic energy of 2.6 Mev [12].

4.2. Measured Corrections

The leakage of photons and electrons from the surfaces of the calorimeter cylinder was investigated in two subsidiary experiments. The first was performed by replacing the calorimeter cylinder by a large lead medium and determining the relative amount of energy, $\epsilon(r,x)$, absorbed at different points, where r is radius, measured from the beam axis, and x is depth in the medium. The medium was composed of 24 cm diam lead disks mounted perpendicular to the beam axis, each 12 g/cm² thick. $\epsilon(r,x)$ was obtained from densitometer measurements of X-ray films which had been sandwiched between these disks and exposed to X-rays. The analysis assumed that density was proportional to absorbed energy, an assumption which was justified in the tests described at the end of this section. Figure 7 shows the densitometer traces obtained at 170 Mev in experiment B, normalized to the same energy incident on the medium.

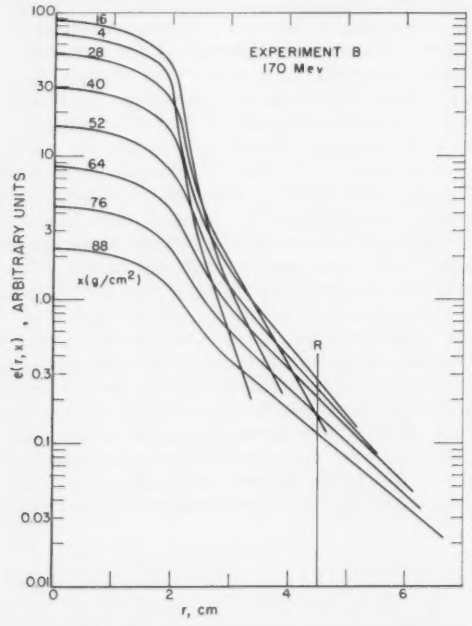

FIGURE 7. *Typical radial distributions of absorbed energy at several depths in a lead medium.*

R is the radius of the calorimeter cylinder.

The fraction of energy absorbed in the medium outside the cylinder volume is:

$$\text{leakage fraction}=\frac{\int_0^L I_1(x)dx+\int_L^\infty I_2(x)dx}{\int_0^\infty I_2(x)dx} \qquad (1)$$

where:

$$I_1(x)=\int_R^\infty \epsilon(r,x)rdr$$

$$I_2(x)=\int_0^\infty \epsilon(r,x)rdr$$

and R and L are the radius and length of the cylinder, respectively. The integrals $I_1(x)$ and $I_2(x)$ are plotted in figures 8 and 9 for the data obtained in experiment B. The curves of figure 9 are broad-beam transition curves, showing the relative amount of energy which would be absorbed at different depths in a lead medium bombarded by a uniform bremsstrahlung beam of infinite diameter.

The leakage fraction predicted by eq (1) is smaller than the fraction of energy leaking from the sides and back of the calorimeter cylinder in vacuo because of the enhanced backscatter of the lead medium at the cylinder boundaries. However, it was shown that the difference is negligible by exposing films at depth L with different thicknesses of backing. As the backing thickness was increased from zero, the absorbed energy rose to a saturation value at a thickness of only 1 mm.

The second subsidiary experiment was a determination of the fraction of energy backscattered from the calorimeter cylinder itself. This experiment was performed with a scintillation spectrometer, using a cylindrical sodium iodide crystal with an axial hole, mounted in front of the calorimeter cylinder as shown in figure 10. The crystal was viewed by four photomultipliers, which generated an electronic pulse each time a backscattered photon or secondary electron interacted with the crystal. A 256 channel pulse height analyzer was used to sort and display the pulses as a function of pulse height. Figure 11 shows the pulse height distributions obtained at 25, 50, 90, and 170 Mev, corrected for background. In these distributions, the large peaks at 511 kev were produced by photons resulting from positron annihilation in the cylinder,

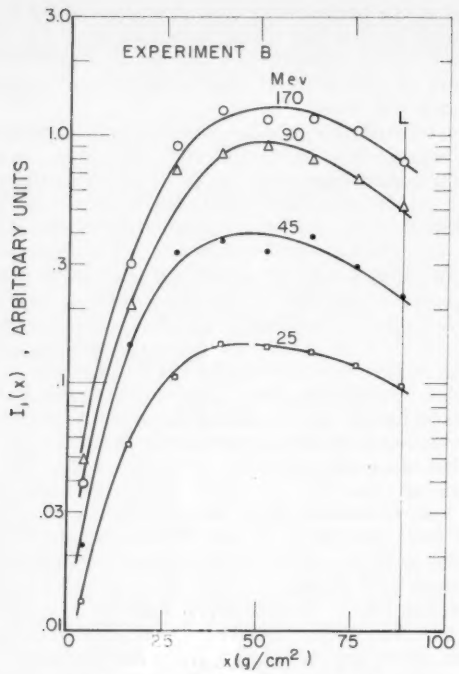

FIGURE 8. *Sidescattered energy.*

$I_1(x) = \int_R^\infty e(r,x)rdr$ from the film measurements of experiment B. L is the length of the calorimeter cylinder.

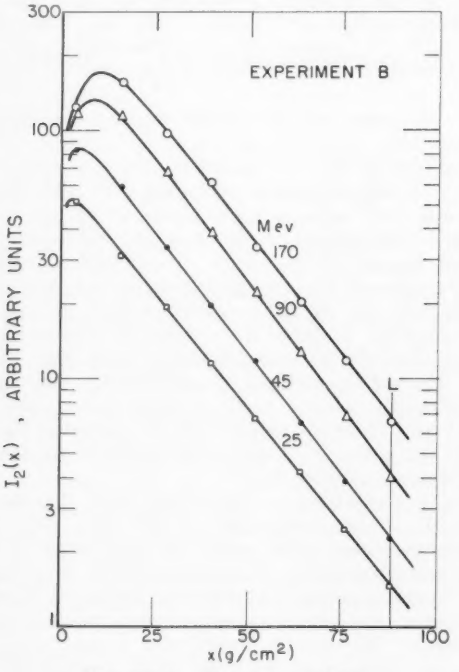

FIGURE 9. *Transition curves.*

$I_2(x) = \int_0^\infty e(r,x)rdr$ from the film measurements of experiment B. L is the length of the calorimeter cylinder.

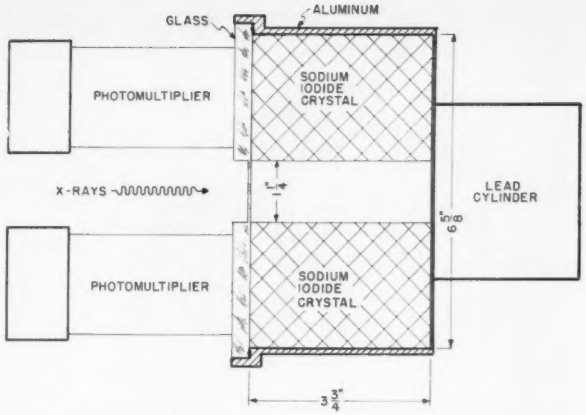

FIGURE 10.—*Arrangement of scantillation spectrometer to determine fraction of energy backscattered from calorimeter cylinder.*

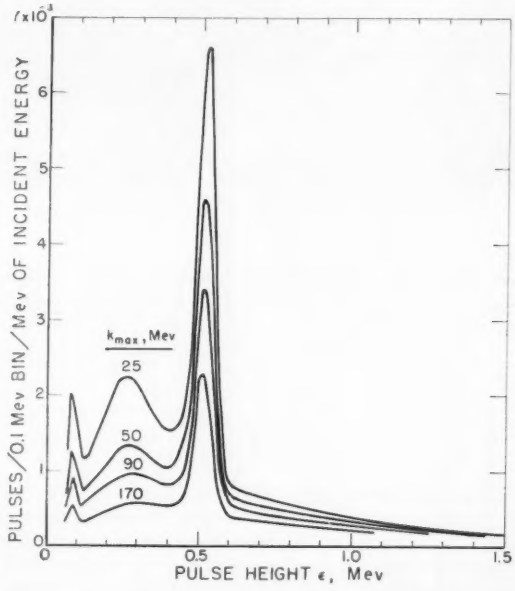

FIGURE 11. *Pulse height spectra produced by radiation backscattered from calorimeter cylinder.*

the broad peaks around 250 kev were produced by singly-scattered photons, and the peaks at 80 kev by lead K X-rays. The low level background, which decreases monotonically with increasing pulse height, ϵ, was presumably caused by electrons, multiply-scattered photons, and bremsstrahlung.

Each pulse height distribution, $P(\epsilon)$, was transformed into a particle spectrum, $N(k)$, by solving the integral equation:

$$P(\epsilon) = \int_0^{k_{max}} N(k)S(k)K(k,\epsilon)dk \qquad (2)$$

where $S(k)$ is the probability that a photon or electron of energy k will interact with the crystal, and

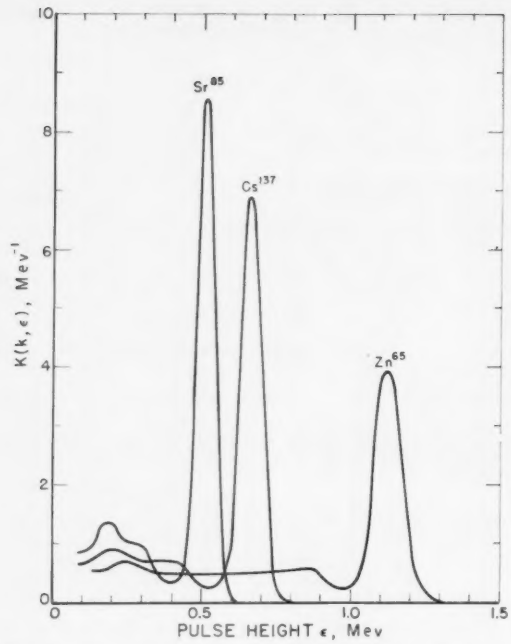

FIGURE 12. *Pulse height spectra produced in the backscatter crystal by monoenergetic photons from radioactive sources, normalized to unit enclosed area.*

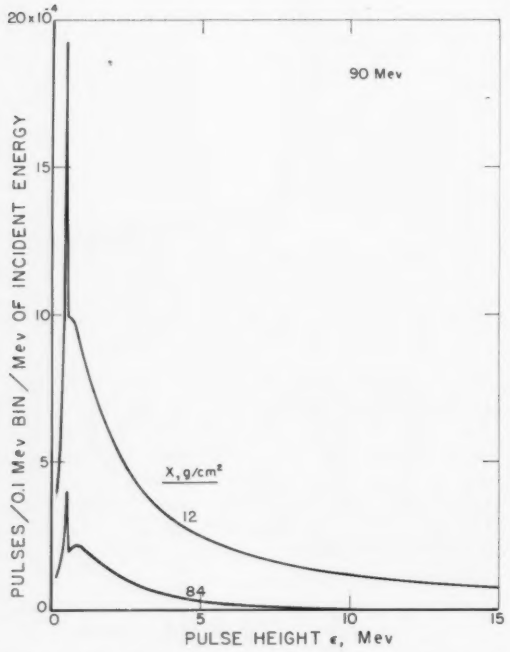

FIGURE 13. *Pulse height spectra produced by the 90 Mev bremsstrahlung transmitted by a lead medium of thickness X.*

$K(k, \epsilon)$ is the probability that it will generate a pulse of height ϵ after the initial interaction. For given k, $K(k, \epsilon)$ is the pulse height distribution produced by photons or electrons of that energy, normalized to unit enclosed area.

The scintillation spectrometer cannot distinguish between incident photons and electrons, yet the transformation from $P(\epsilon)$ to $N(k)$ depends upon the nature of the incident particles because both the sensitivity, $S(k)$, and the response function, $K(k, \epsilon)$, differ for photons and electrons. The transformation was first made by assuming that only photons were incident on the crystal and solving eq (2) by standard matrix methods [13]. $K(k, \epsilon)$ was measured for k=0.51, 0.66, and 1.12 Mev by placing Sr, Cs, and Zn radioactive sources on the front surface of the cylinder, producing the pulse height distributions shown in figure 12. Each of these distributions was approximated by a one parameter function, a delta function at $\epsilon = k$ and a flat tail for $\epsilon < k$. The one parameter, the relative area under the delta function, was measured from the distributions of figure 12 at low energies and was extrapolated to higher energies with the help of the theoretical predictions of Berger and Doggett [14]. This relative area, or "photofraction," varied from 0.96 at 0.3 Mev to 0.08 at 170 Mev. $S(k)$ was calculated from the crystal geometry, assuming isotropic backscattering, and using published total attenuation coefficients for sodium iodide [9]. It varied from 0.985 below 0.1 Mev to a minimum of 0.580 at 5 Mev. The fraction of energy backscattered was calculated from:

$$\text{fraction backscattered} = \int_0^{k_{max}} kN(k)dk. \quad (3)$$

The fraction backscattered was recalculated assuming that only electrons were incident on the crystal, using $K(k, \epsilon) = \delta(k - \epsilon)$ and $S(k) = 0.985$ for all k. These two determinations of the fraction backscattered were weighted and averaged, assuming that 13½ percent of the backscattered energy was carried by electrons. This estimate is one-half of the fraction of the energy emerging from the back of the cylinder which is carried by electrons, as revealed by the shape of the transition curves of figure 9 with the help of a simple theory of energy absorption [15]. This method of estimating the electron contribution is only approximate, but since it reduced the fraction calculated for photons by only about 0.2 percent at all energies, the uncertainties are relatively unimportant.

The scintillation spectrometer was also used to check the film measurements of the variation of absorbed energy with position in a lead medium. This was done with a 9 in. diam, 6¼ in. long sodium iodide crystal placed immediately behind the medium to look at the spectrum of transmitted X-rays and electrons. Figure 13 shows the pulse height distributions obtained with 90 Mev bremsstrahlung, using two different medium thicknesses. These distributions, plus one at 25 Mev, were analyzed to find the fraction of energy transmitted by the medium,

using the analytical technique outlined above. The results are listed in table 3 along with the predictions of the film measurements, which come from the formula:

$$\text{fraction of energy transmitted}=\frac{\int_X^\infty I_2(x)dx}{\int_0^\infty I_2(x)dx} \quad (4)$$

where X is the medium thickness. The good agreement between these two determinations of the transmitted energy was interpreted as a verification of the film analysis procedure.

TABLE 3. *Comparison of film and spectrometer determinations of energy transmitted by lead medium of thickness X*

k_{max}	X	Percent transmitted	
		Spectrometer	Film
Mev	*g/cm²*		
90	12	64.1	59.3
90	84	2.85	2.64
25	84	2.84	2.97

5. Ionization Chamber Calibrations

The monitor calibrations of table 2 have only a transitory value, and were transferred by direct comparison to the more permanent aluminum ionization chamber shown in figure 14. This large chamber is labeled P2–4 and has been described in detail elsewhere [16]. Its calibration in joules/coulomb was obtained from the formula:

$$\text{Cal (P2–4)}=\frac{(\text{Joules/monitor volt})\times F_A}{C\times(\text{P2–4 volts/monitor volt})} \quad (5)$$

where C is the capacitance of the capacitors charged by P2–4 (0.10197×10^{-6} $\pm0.05\%$ farads) and F_A is a small correction [16] used with the data of experiment A to change it to refer to the filtration of experiment B.[3]

The calibrations of P2–4 are listed in table 2,[4] along with F_A and the chamber comparison data.

The P2–4 calibrations from experiments A and B agree to within 2 percent except for the 42.1 Mev measurement, which is a trifle high. The data from the two experiments were combined, to yield better statistics, and the average calibrations are also listed in table 2. Data from the three lowest energies in experiment A were averaged with the 20 Mev data in experiment B, but otherwise the energies were paired, below 45 Mev. This averaging introduces some uncertainty in the energy assignments,

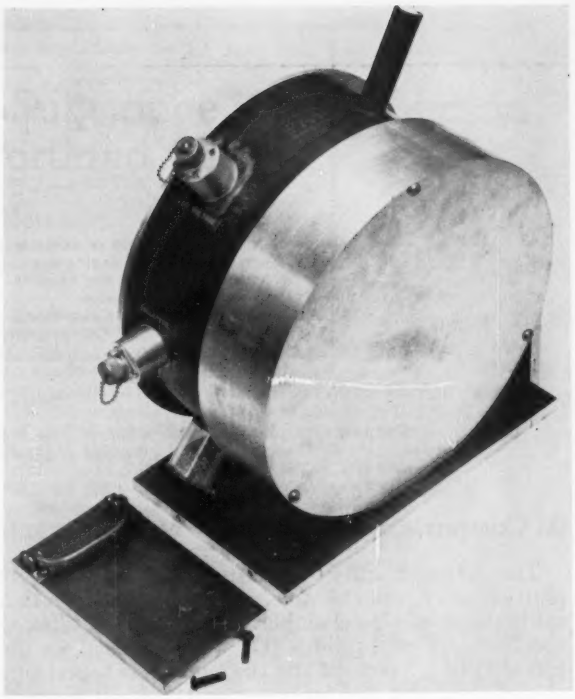

FIGURE 14.—*Aluminum ionization chamber P2–4.*

but this is inconsequential because the calibration varies slowly with k_{max} below 45 Mev. The numbers listed as sdm in table 2 are the statistical standard deviations of the mean of each average:

$$\text{sdm}=\sqrt{\frac{\sum_i \delta_i^2}{n(n-1)}} \quad (6)$$

where δ_i is a deviation from the mean and n is the number of cases. The net systematic error was taken to be the square root of the sum of the squares of the estimated maximum systematic errors listed in table 4. The statistical and systematic errors were combined with the arbitrary formula:

$$\text{Total error}=3\times\text{sdm}+\text{net systematic error}. \quad (7)$$

The statistical part of the total error of each point is consequently considerably more pessimistic than a probable error.

TABLE 4. *Estimated maximum systematic errors in P2–4 calibration*

	%
Electrical energy measurements	0.2
Monitor stability	.2
Foil correction	.1
Nuclear correction	.2
Leakage correction	.3
Backscatter correction	.3
Net systematic error	.6

[3] The filtration of experiment B is listed as entirely of aluminum, since the calibrations are insensitive to the difference between Pyrex and aluminum filters [16].

[4] The earlier versions of these calibrations which appeared in references [5] and [18] differ because they were printed before the backscatter correction had been determined.

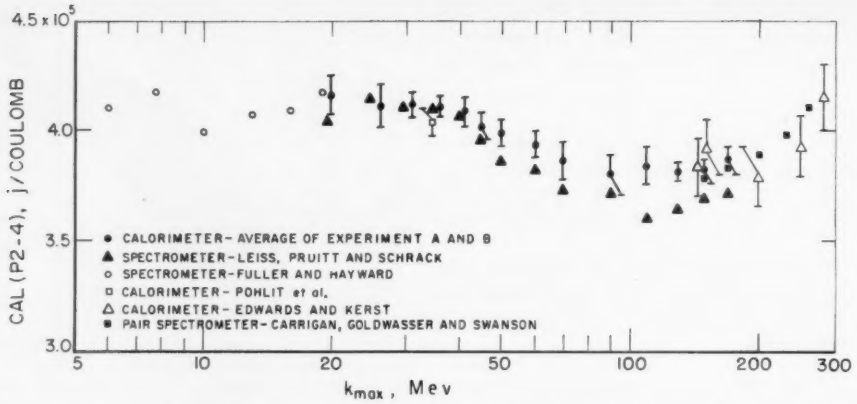

FIGURE 15. *Absolute calibrations of ionization chamber P2–4 in a 4.2 cm diam bremsstrahlung beam filtered by 4.5 g/cm² of aluminum, at 20° C and 760 mm of mercury.*

6. Comparison With Other Measurements

The average P2–4 calibrations of table 2 are plotted in figure 15 for comparison with other calibrations of this chamber. The first scintillation spectrometer calibrations [17] were assigned an uncertainty of ±3 percent and the more recent spectrometer calibrations [18] an uncertainty of ±2 percent. The 34.5 Mev calorimetric calibration was made with chamber P2–6 in Frankfurt and was transferred to P2–4 by direct comparison [5]. The calorimetric calibrations based on the work of P. D. Edwards and D. W. Kerst [3] were transferred to P2–4 from replicas of their copper ionization chamber at the NBS and the University of Illinois. The pair spectrometer measurements [19] are not absolute, and were normalized to a weighted average of the NBS calorimeter and spectrometer calibrations at 170 Mev. The NBS spectrometer calibrations and the Frankfurt calibration have been corrected for differences in beam diameter and filtration [16]. No such corrections have been applied to the other points, but they are probably quite small compared to the uncertainties in these points.

The P2–4 calibrations shown in figure 15 are all in good agreement except for the spectrometer measurements above 45 Mev, which differ from the calorimeter measurements by as much as 5 percent. The source of this discrepancy is thought to be a time dependent systematic error in the spectrometer measurements, which were made in two sets. The measurements above 45 Mev predated the lower energy measurements, except at 90 Mev, which contains data from both sets. This is the high energy spectrometer point in closest agreement with the calorimeter calibrations.

The authors express their thanks to all members of the NBS High Energy Radiation Section for their help with these experiments, and to J. McElhinney and B. Zendle for their invaluable pioneering work.

7. References

[1] NBS Handbook 55, appendix B (1954); H. W. Koch, J. E. Leiss, and J. S. Pruitt, Bull. APS II **1,** 199 (1956)A; R. R. Wilson, Nuclear Instr. **1,** 101 (1957).
[2] J. S. Laughlin and J. W. Beattie, Rev. Sci. Instr. **22,** 575 (1951); Laughlin, Beattie, Henderson, and Harvey, Am. J. Roentgenol. **70,** 294 (1953); Skarsgard, Bernier, Cormack, and Johns, Rad. Research **7,** 217 (1957); G. D. Adams, Radiology **69,** 867 (1957).
[3] P. D. Edwards and D. W. Kerst, Rev. Sci. Instr. **24,** 490 (1953).
[4] S. P. Kruglov, Zhur. Tekh. Fiz. **28,** 2310 (1958) (Soviet Phys.—Tech. Phys. **3,** 2120 (1958)); S. P. Kruglov and I. V. Lopatin, Zhur. Tekh. Fiz. **30,** 424 (1960).
[5] J. S. Pruitt and W. Pohlit, Z. Naturforsch. **15b,** 617 (1960).
[6] J. McElhinney, B. Zendle, and S. R. Domen, J. Research NBS **56,** 9 (1956).
[7] F. Seitz and J. S. Koehler, Proc. of Int. Conf. on Peaceful Uses of Atomic Energy, United Nations (1956), Vol. 7, p. 615.
[8] A. S. Penfold and J. E. Leiss, Analysis of photo cross sections, (Phys. Research Lab., Univ. of Illinois, Champaign, Ill., 1958).
[9] G. W. Grodstein, NBS Circular 583 (1957).
[10] R. Montalbetti, L. Katz, and J. Goldemberg, Phys. Rev. **91,** 659 (1953).
[11] L. W. Jones and K. M. Terwilliger, Phys. Rev. **91,** 699 (1953).
[12] M. E. Toms and W. E. Stephens, Phys. Rev. **108,** 77 (1957); W. R. Dixon, Can. J. Phys. **33,** 785 (1955).
[13] J. Kockum and N. Starfelt, Nuclear Instr. and Meth. **4,** 171 (1959).
[14] M. J. Berger and J. Doggett, J. Research NBS **56,** 355 (1956).
[15] F. Rasetti, Elements of nuclear physics, p. 96, eq. III, 34. (Prentice-Hall, New York, 1936).
[16] J. S. Pruitt and S. R. Domen, NBS Monograph 48 (1962).
[17] J. E. Leiss, J. S. Pruitt, and R. A. Schrack (unpublished data).
[18] E. G. Fuller and Evans Hayward, J. Research NBS **65A,** (Phys. and Chem.) No. 5, 401 (1961).
[19] R. Carrigan, E. Goldwasser, and W. Swanson (private communication).

(Paper 66A5–172)

JOURNAL OF RESEARCH of the National Bureau of Standards—A. Physics and Chemistry
Vol. 66A, No. 5, September–October 1962

Zinc Oxide as a Standard Substance in the Solution Calorimetry of Portland Cement

Edwin S. Newman

(May 10, 1962)

Zinc oxide is the standard substance specified for calibrating the heat-of-solution calorimeters used in determining the heat of hydration of portland cement in several American and foreign cement specifications. The heats of solution of zinc oxide samples from different sources and after different heat treatments have been determined in the standard mixture of nitric and hydrofluoric acids. It is concluded that the value given in the specifications is low, that heat treatment in the range 310 to 950 °C is not critical, that small variations in the ZnO/acid weight ratio are without significance, and that analytical-reagent zinc oxide from various sources may safely be used. The mean value obtained for the heats of solution of zinc oxide from twelve sources determined in triplicate in $1.00HNO_3$,$0.284HF$,$26.38H_2O$ at a ZnO/acid weight ratio of 7/425 at 25 °C was 257.82 cal/g with a standard error of 0.015 cal/g. The thermochemical calorie of 4.1840 joules is used. The temperature coefficient based on least-square fitting to 16 data points obtained in an earlier study was −0.087 cal/g-deg, with a computed standard error of 0.013 cal/g-deg. The corresponding values for heat of solution and temperature coefficient given in the specifications are 256.6 cal/g and −0.1 cal/g-deg, respectively.

1. Introduction

Several specifications [1, 2, 3] [1] require the use of zinc oxide as the standard substance for calibrating the heat-of-solution calorimeters by which the heat of hydration of portland cement is determined. For this purpose the heat of solution of ZnO has been determined [4, 5] in the mixture of nitric and hydrofluoric acids used in measuring the heats of solution of cements and cement pastes. Roth and Chall [6] and Peppler and Newman [7] have also determined the heat of solution of zinc oxide in hydrochloric acid.

The heat of solution of ZnO in the nitric-hydrofluoric acid mixture was given by Stenzel and Morris [4] as 256.1 cal/g without reference to the temperature of reaction, although it is believed that the final temperature of their calorimeter was 31.5 °C [8, p. 589]. They calibrated their calorimeter electrically but did not define their calorie. It is believed that the calorie of 4.1833 international joules was used. Elsewhere throughout this paper the defined thermochemical calorie of 4.1840 joules (4.1833 international joules) is used.

Shartsis and Newman [5] determined the isothermal heat of solution of ZnO over the temperature range 20 to 35 °C and reported a temperature coefficient of −0.1 cal/g-deg. Newman [9] made a few measurements at two ZnO/acid ratios and reported a relationship between heat of solution and sample weight. No other independent determinations of the heat of solution of zinc oxide in nitric-hydrofluoric acid have been found, other authors having accepted the specification value of 256.6 cal/g at 25 °C [1, 5].

Recently the American Society for Testing Materials has directed attention to the improvement of the simple vacuum-flask cement calorimeter by the use of an isothermal jacket and by other means. In the course of tests, new measurements of the heat of solution of ZnO were made by the author and are reported below. Since these values differed from the published measurements, the original data from this laboratory [5, 9] were re-examined, and those heats of solution were recalculated, using in so far as possible the current method of determining the corrected temperature rise of the calorimeter. In the current procedure, bridge-dial corrections are used, and the time-resistance (temperature) values used in computation are taken from large-scale smooth curves drawn through the observed values. The bridge corrections were not determined in the earlier work and were not available for the recalculation. The calibration experiments on which this earlier work was based were also recalculated, and the revised energy-equivalent values obtained were used in the computations.

Before an individual lot of ZnO is used in a series of calibration experiments, it is sintered by heating for one hour at 950 °C to reduce the surface [1, 2] and ground, tediously, by hand, to pass a No. 100 sieve. During this grinding, moisture which must be removed is gained from the atmosphere, and a second heating is required. Measurements were made of the heats of solution of samples of zinc oxide which had not been ground and reheated, but which had simply been heated for 2 hr to various temperatures and introduced into the calorimeter after cooling in a desiccator over magnesium perchlorate and weighing.

In this investigation of the heat of solution of zinc oxide in a nitric-hydrofluoric acid mixture of a single composition, the effects of a number of variables were considered. On single lots of zinc oxide, the effects of varying the temperature of heating, the time of heating at 950 °C, and the ZnO/acid

[1] Figures in brackets indicate the literature references at the end of this paper.

weight ratio, and of different batches of 2.00 *N* nitric acid were examined. The heats of solution of zinc oxide lots from widely separated sources were measured. As a check on the calorimeter assembly and operation, the heat of solution of KCl in water was determined for comparison with published values.

2. Materials, Apparatus, and Procedure

Three 50-liter batches of 2.00 N nitric acid were prepared at different times and stored in a 50-liter polyethylene bottle while being used. The acid was standardized volumetrically against NaOH solution and potassium acid phthalate (NBS Standard Sample No. 84b).

Twelve different lots of zinc oxide were used, seven from the United States, two each, by different manufacturers, from England and Germany, and one from Japan. One, from the United States, the only sample not of reagent grade, was the Rubber Reserve Standard for the compounding of rubber. Two others, NBS Standard Sample 370A and one intended for the NBS Standard Sample 370B but rejected on the basis of compounding tests, were also manufactured for the test compounding of rubber. Both were of analytical-reagent grade. All the others were reagent-grade chemicals in the country of their origin, and are there used to calibrate cement calorimeters.

The composition and properties of sample 370A were as follows, as given by the manufacturer at the time of its establishment as a standard material for the compounding of rubber:

	%	American Chemical Society specification limits for analytical reagent (1960)
Loss at 110°	0.12	
Total sulfur as SO_4	.007	0.010 maximum
Pb	.0011	.005
Cu	.0001	
Mn	.0001	.0005
As	.0001	.0002
Fe	.0009	.001
ZnO	99.9	

This material passed the American Chemical Society specification tests for material insoluble in sulfuric acid (<0.010%), alkalinity, chlorides (<0.001%), and nitrates (<0.003%). The specific surface of the original material as determined by nitrogen adsorption was 3.3 m^2/g. After sintering for 1 hr at 950 °C and grinding to pass a No. 100 sieve, the surface determined by nitrogen adsorption in this laboratory was 1.7 m^2/g.

About a third of the heat-of-solution measurements, namely those concerned with the effect of different heating temperatures and part of those made with differing sample weights, was made on one lot of zinc oxide. The remaining measurements were made, generally in sets of four replicate determinations, on the various lots of zinc oxide subjected to the standard treatment of heating and grinding A single lot which had been heated for 17 hr, instead of 1 hr, at 950 °C was also tested.

Analytical-reagent potassium chloride was recrystallized twice, dried at 200 °C, and passed through a No. 30 sieve. Its heat of solution in distilled water was determined at a nominal H_2O/KCl molar ratio of 1,500.

An improved platinum calorimeter reaction vessel, described elsewhere [10], was used in the isothermal jacket of the calorimeter described in earlier papers, [11, 12]. The calorimeter fluid was 14 ml of 48-percent HF solution and enough 2.00 *N* HNO_3 to make a total charge of 740.00 g. The calorimeter was operated in a 30-liter water bath at 25.4 °C (25.0 °C in the later work) controlled to ±0.002 °C during a determination. The water bath and the instruments were in a constant temperature room generally controlled at 25.5±0.5 °C. The temperature measurements were made using a platinum resistance thermometer in a platinum envelope. A G–1 Mueller bridge was used with a type HS galvanometer with an 8-m light beam. Measured resistances were recorded to 10 μohms, corresponding to a galvanometer scale deflection of 1 mm. At small rates of temperature change the sensitivity was doubled by reversing the bridge current. A current of 8 ma was used, corresponding to 4 ma in the resistance thermometer. The effect of this current on the thermometer resistance was quite apparent, and the measurements were generally made not less than 110 sec after the bridge current was turned on, in order to allow the thermometer resistance to attain its steady-state value. The scale zero was determined after each 2-min temperature reading, either by switching off or by reversing the bridge current.

The bridge was calibrated in place just before the heat-of-solution measurements were begun. The K–2 potentiometer, the standard cell, standard resistance, and volt box used in measuring the electrical-energy input were calibrated by the Electricity Division of the National Bureau of Standards. For the early calibrations (see table 1), the electrical heating of the calorimeter was timed automatically on a chronograph paced by the standard seconds signal of the NBS. When the chronograph was used, electrical heating times were about 9 min, and the total error in measuring the tape was probably no larger than ±0.03 sec. Most of the calibrations, however, were made by turning the current on and off by means of a relay activated by the seconds signal. Oscilloscopic measurements showed a net correction of −7 msec to the nominal time indicated by the individual seconds pulses which turned on and turned off the calorimeter heating current. The calorimeter was operated as nearly as possible between the same two temperatures in all experiments with a given weight of zinc oxide, and was generally calibrated between these temperatures also, usually beginning and ending within 0.02 deg C of the two selected temperatures. The final temperature was generally within a few hundredths of a degree C of the bath temperature.

TABLE 1. *Electrical calibrations*

(1 calorie=4.1840 joules)

Number	Calorimeter fluid	Average [a] calorimeter temperature (θ_{avg})	Heating rate	Temperature rise	Energy equivalent	
					Average value	Standard error
		Ohm	*cal/sec*	*° C*	*j/ohm*	*j/ohm*
1353–59 [b, c]	Acid O [b]	2.5767–2.5771	0.78	0.7	24088	5
1652–59 [c]	Acid A	2.4552–2.4688	3.8	3.3	27967.6	4.2
1719–23	Acid B	2.4160–2.4422	3.8	3.3	27974.5	4.6
1724–28	Acid B	2.3634–2.3690	3.8	4.4	27976.5	4.1
1730–36	Acid B	2.5334–2.5389	.95	1.0	28006.5	7.0
1773A to 1775F [d]	Acid C	1.9470–2.6920	.92	1.0	$27519.5+195.5\theta_{avg}$	
1779–82	Water	2.5314–2.5493	3.7	1.0	31994.4	4.5
1783–86	Water	2.5329–2.5345	.93	1.0	31992.9	6.6
1837–41 [e]	Water	2.5820–2.5880	.52	0.15	32081	39
1842–48	Water	2.5860–2.5889	.23	.15	32026	9

[a] Bridge dial readings, add 25.5 ohms. At 25 °C, $\theta_{avg}=2.61$ ohm, $dR/dT=0.1010$ ohm/deg.
[b] Data obtained with calorimeter containing 600.0 g of an earlier batch of acid. J. Research NBS **62** 207–211 (1959) RP2955.
[c] Timed by chronograph. All other calibrations timed by relay.
[d] 5 consecutive 1-deg rises per determination.
[e] Measurements by operator B. All others by operator A.

Three 50-liter batches of 2.00 *N* HNO_3 were used. With acid from the first (acid A) batch, the calorimeter was calibrated using the chronograph, with the second (acid B) and third (acid C), using the relay. For use with acid C, the calorimeter was calibrated three times over five consecutive 1-deg temperature rises from 20 to 25 °C, using the final rating period for one increment as the initial rating period for the next. The least-squares linear equation relating the observed energy equivalent to the average calorimeter temperature as indicated by the resistance thermometer was calculated from the 15 points obtained. Since all heat-of-solution determinations ended near the bath temperature, different average temperatures were obtained with different weight samples, and the equation was used to calculate the energy equivalent to be used. By this procedure otherwise necessary large differences in either electrical-heating rates or times were not involved in the comparison of heats of solution of different weight samples of zinc oxide.

The energy equivalent was determined with the calorimeter containing only the mixed acids. The sample when added was at a temperature near to the final calorimeter temperature, and the heat it carried into the calorimeter was accounted for by the heat capacity of the sample and the small temperature difference involved. This procedure is equivalent to the use of the heat capacity of the reactants in calculating the heat of reaction. The result, therefore, is the isothermal heat of reaction (solution) at the final temperature of the calorimeter.

The temperatures at the beginning, middle, and end of the two 20-min rating periods of each calorimetric determination were obtained from smooth deviation curves drawn through the recorded data plotted at a scale of 1.5mm=10 μohms. Experimental periods [13, p. 38] of 20 min were used for heat-of-solution experiments, and periods of 20 to 30 min were used for calibration experiments. The corrected temperature rise in ohms was calculated using the Second Geophysical Laboratory Method described by White [13, p. 42].

The temperature of the interior of the balance was taken as the temperature of the sample at the time of its introduction into the calorimeter through a funnel. Tests showed that a thermometer in the balance case and one immersed in the sample indicated essentially the same temperature. The specific heat of ZnO was taken as 0.12 cal/g-deg [14], and the correction for the sensible heat carried into the calorimeter with the sample averaged −0.051 cal/g. Extreme values of −0.127 and +0.046 cal/g were obtained with the exception of seven values ranging from −0.138 to −0.289 cal/g reached during two brief periods in July when the air conditioner was not operating properly.

Heats of solution recorded in this paper are corrected to 25.0 °C from the final calorimeter temperature, using −0.09 and −0.48 cal/g-deg for the temperature coefficients of the heats of solution of ZnO and KCl [18], respectively. The measurements of the effect of temperature of heating on the heat of solution of ZnO were made at the rate of two measurements per day in a series such that each treatment was measured once in the morning and once in the afternoon, but not twice on the same day. The series was then repeated. The various standard-treated samples were measured at the rate of four a day, programed so that none was measured twice on the same day or twice at the same (2-hr) period during the day.

3. Results and Discussions

3.1. New Data

a. Calibrations

The electrical calibrations made in this work are reported in table 1.[2] For these various calibrations,

[2] Standard deviation of the average, standard error, is given here and elsewhere in this paper, calculated by the formula

$$s=\sqrt{\frac{\Sigma x^2-(\Sigma x)^2/n}{n(n-1)}},$$

where x is the individual observation, and n is the number of observations. Where data in this paper is given in the form $a\pm b$, a represents the mean value and b, the standard error of a. Also for the comparison of two averages the t-test was used at the 5 percent level of significance [15].

the applied voltage was adjusted so that each rise was generally accomplished by heating times of 9 to 13 min. The heating rates for calibrations with acid varied by a factor of about four, as did the temperature intervals over which the calibrations were made. No effect of heating rate on the energy equivalent was evident which could be separated from effects of different acid batches or from the increase of energy equivalent with average temperature. A perceptible effect of heating rate would be expected if systematic error were present in the electrical heating. As a further check, the calorimeter, charged with 740.00 g of water, was calibrated over a 1-deg temperature interval ending near the bath temperature at two heating rates differing by a factor of about four, see table 1, Nos. 1779–1786. No significant effect was found at these rates. For

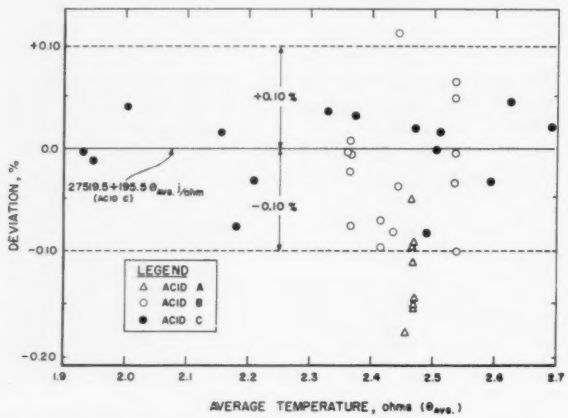

FIGURE 1. *Electrical calibration of calorimeter containing nitric-hydrofluoric acid.*

Results for three batches are shown.

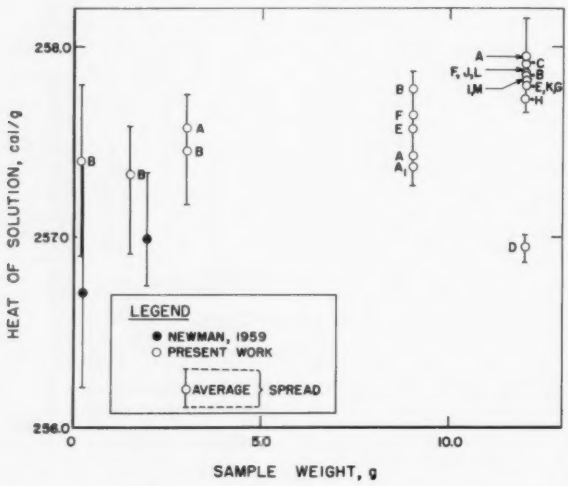

FIGURE 2. *Effect of ZnO/acid weight ratio on the heat of solution of zinc oxide in nitric-hydrofluoric acid.*

The zinc oxide was heated 1 hr at 950 °C, ground to pass a No. 100 sieve, and reheated for 5 min (1 cal=4.1840 j).

determining the heat of solution of KCl, the calorimeter was calibrated for a temperature rise of about 0.15 °C at heating rates of about one-half and one-quarter of the smaller of the two rates used for the 1-deg experiments. These data are also given in table 1, Nos. 1837–1848. The energy equivalents obtained by these two smaller rates differed by about 0.2 percent. Contributing to this difference is the fact that the 0.15-deg experiments at the faster rate were performed by a different operator. The energy equivalent obtained for a 0.15-deg rise at the slower rate was about 0.07 percent higher than the value obtained by the same operator for a 1-deg rise at 16 times the heating rate, when both energy equivalents were calculated at the same average temperature by means of the temperature coefficient shown in table 1 (No. 1773A–1775F). This 0.07 percent difference might be attributable to the 16-fold difference in heating rate.

Figure 1 shows the results of calibrations made with nitric-hydrofluoric acid solution in the calorimeter. A least-squares linear equation for the relationship between the energy equivalent found using acid C and the average calorimeter temperature in ohms was calculated from the data in table 1. This equation

$$E=27519.5+195.5\ \theta_{avg}$$

where E is j/ohm, and θ_{avg} is average dial reading in ohms, is plotted in figure 2 as a straight horizontal line. The individual determinations from which the line was calculated, and the rest of the values for acids A, B, and C given in table 1, are shown in figure 1, deviations from the line in percentage being plotted as ordinates against the average temperature in ohms as the abscissas. Acid A, for which the calorimeter was calibrated by chronograph, is seen to be generally about 0.1 percent low compared with the other two.[3]

b. Heats of Solution, Potassium Chloride in Water

The results of the measurements of the heat of solution of recrystallized potassium chloride in water are given in table 2. Results obtained for a different lot of reagent, not recrystallized, are also given. The average values for the recrystallized salt are larger than the tentative "best" value of $\Delta H^{\circ}_{\infty}=4115$ cal/mole recently reported [19].

c. Zinc Oxide in Nitric-Hydrofluoric Acid

The results of the measurements of the heats of solution of 9-g samples of zinc oxide A heated for 2 hr at 150, 310, 660, and 950° C are given in table 3. These samples do not show the reduction in heat of solution with increased temperature of heating found

[3] The reason for this difference is not known. An error of about 0.03 [16] in adjusting the normality of this batch of acid would account for the difference but seems excessive. Tests have shown no significant difference in timing between chronograph and relay.

TABLE 2. *Heat of solution of* KCl *in water*

(1 calorie=4.1840 joules)

Lot	A	B (Recrystallized)	B (Recrystallized)
Operator	B	B	A
Numbers	1803 to 06	1837 to 42	1843 to 46
Final temperature (θ_2) °C	24.80 to 24.82	24.84 to 25.00	24.88
Sample temperature (θ_r) [a] °C	25.35 to 25.90	24.90 to 27.00	25.30 to 25.50
n [b]	1017.6 to 1021.1	1491.4 to 1496.5	1492.6 to 1495.5
Correction for sample temperature [c] cal/g	−0.089 to −0.178	+0.008 to −0.348	−0.069 to −0.102
Correction to 25 °C [d] cal/g	+0.083 to +0.096	0 to +0.077	+0.056
Heat of solution at 25 °C cal/g	−56.495 to −56.669	−56.043 to −56.273	−56.127 to −56.241
cal/mole	−4212.1 to −4225.1	−4178.4 to −4195.5	−4184.7 to −4193.2
$\Delta H^{\circ}_{\infty}$ [e] cal/mole	4146±3 [f]	4122±5 [f]	4125±2 [f]

[a] Temperature in balance case.
[b] Moles H_2O/moles KCl=(740.00/18.016)/[(Sample weight)/74.557].
[c] −0.165 (θ_r−θ_2) NBS Circular 500.
[d] +0.48(25.00−θ_2) J. Coops, G. Somsen, and M. W. Tolk, Calorimetry Conference, Ottawa (1961).
[e] Corrections to heat of solution for n=1,000 and 1,500 are negligible. Corrections to ΔH for $n=\infty$ are −71 and −63 cal/mole for n=1,000 and 1,500 respectively, V. Barfield, Calorimetry Conference, Ottawa (1961).
[f] Standard error.

TABLE 3. *Heat of solution of zinc oxide "A" heated for 2 hr at various temperatures* [a]

(1 calorie=4.1840 joules)

Number	150 °C	310 °C	660 °C	950 °C
	cal/g	cal/g	cal/g	cal/g
1	256.95	257.40	257.61	257.35
2	256.82	257.55	257.20	257.33
3	256.80	256.90	257.06	257.03
4	256.88	257.29	257.32	257.27
5	[b] 256.97		[b] 257.28	
Average	256.88	257.28	257.29	257.25
S.D. Avg	0.034	0.139	0.090	0.073

[a] 9-g samples.
[b] Omitted from variance analysis.

TABLE 4. *Residual ignition loss* [a] *of zinc oxide "A" after heating for 2 hr at various temperatures*

Number	Unheated [b]	150 °C	310 °C	660 °C
	%	%	%	%
1	0.243	0.133	0.057	0.020
2	.245	.129	.056	.017
3	.241	.139	.056	.018
4	.246	.134	.058	.011
5		.139		.016
Average	0.244	0.135	0.057	0.016

[a] Calculated ignition loss if sample were heated at 950 °C.
[b] Observed loss at 950 °C.

TABLE 5. *Calculated heat of solution of zinc oxide "A" after heating for 2 hr at various temperatures* [a]

(1 calorie=4.1840 joules)

Number	150 °C	310 °C	660 °C	950 °C
	cal/g	cal/g	cal/g	cal/g
1	257.29	257.54	257.66	257.35
2	257.15	257.69	257.24	257.33
3	257.16	257.04	257.10	257.03
4	257.22	257.44	257.34	257.27
5	[b] 257.32		[b] 257.32	
Average	257.23	257.43	257.34	257.25
S.D. Avg	0.049	0.140	0.092	0.072

[a] Basis: weight ignited at 950 °C.
[b] Omitted from variance analysis.

by Roth and Chall [6] with hydrochloric acid. These investigators heated their samples for 4 hr. It may be that 2 hr, although twice the "standard" heating time, is not long enough to affect the heat of solution significantly. Note, however, the results in table 6 for lot H showing that 17 hr at 950 °C had no appreciable effect. The values in table 3 are calculated on the basis of the actual weight of the zinc oxide after the heat treatment. Table 4 gives the calculated residual loss on ignition of each sample, i.e., the percentage that would be lost if the sample were thereafter heated at 950 °C.

Table 5 gives the heats of solution from table 3, recalculated on the 950 °C ignited basis. These recalculated data show a slight decrease in heat of solution with increase of temperature of heating. The decrease, however, is not significant. On the basis of the data in tables 3 and 5, it is concluded that for calibration of the cement calorimeter the temperature of heating of the zinc oxide is not critical, providing it is 310 °C or more and not over 950 °C.

In performing an analysis of variance on data from table 3, it was found that temperature, test series, and their interaction are significant at the 5-percent probability level. However, if the 150 °C data are omitted, none of these factors or interaction are significant at the 5-percent probability level, and the 12 values yield an average of 257.28 cal/g with a standard error of 0.059 cal/g. Data from table 5 were similarly treated, and it was found that none of the main factors or interaction are significant at the 5-percent probability level. The 16 values yield an average of 257.30 cal/g with a standard error of 0.050 cal/g. Note that all measurements to determine the effect of temperature of heating for 2 hr were performed with 9-g samples of zinc oxide lot A in calorimeter acid batch A.

Table 6 gives a summary of all the measurements of the heats of solution of different lots of zinc oxide subjected to the standard treatment of heating 1 hr at 950 °C, grinding to pass a No. 100 sieve, and reheating for 5 min at 950 °C. The values in this table are significantly higher than those previously reported for zinc oxide [4,5,9], except those for lot D

TABLE 6. *Heat of solution of zinc oxide in nitric-hydrofluoric acid mixture* [a, b]

(1 calorie=4.1840 joules)

Lot	Source	Sample weight	Calorimeter acid	Heat of solution			Remarks
				N[c]	Mean	Standard error	
		g			*cal/g*	*cal/g*	
A	USA	12.18	B	4	257.95	0.075	
		9.00	A	5	257.37	.044	
		9.00	B	4	257.43	.065	
		3.00	B	4	257.57	.022	
B	USA	12.18	B	4	257.85	.033	NBS Standard Sample 370-A.
		9.00	B	4	257.78	.062	
		3.00	B	4	257.45	.128	
		1.50	C	3	257.33	.12	
		0.20	C	4	257.4	.2	
C	USA	12.18	C	5	257.92	.063	NBS Standard Sample 370-B reject.
D	USA	12.18	C	4	256.95	.030	Rubber Reserve Standard.
E	USA	12.18	C	3	257.81	.018	
		9.00	B	4	257.57	.059	
F	USA	12.18	C	4	257.87	.036	Same as E, 2d sample.
		9.00	C	4	257.64	.040	
G	USA	12.18	C	4	257.82	.031	
H	USA	12.18	C	4	257.73	.022	17 hr at 950 °C before grinding.
I	Great Britain	12.18	C	4	257.82	.056	
J	Great Britain	12.18	C	4	257.86	.086	
K	Germany	12.18	C	4	257.81	.054	
L	Germany	12.18	C	4	257.88	.026	
M	Japan	12.18	C	4	257.83	.028	
N	USA	[d] 1.92	O	3	256.98	.18	
		[d] 0.24	O	3	256.7	.4	

[a] Zinc oxide heated 1 hr at 950 °C, ground to pass No. 100 sieve, reheated 5 min, cooled in a desiccator.
[b] Acid mixture, 740.00 g ($1.36HNO_3$,$0.386HF$,$35.88H_2O$).
[c] Number of determinations.
[d] 1.56 and 0.20 g determined in calorimeter containing 600.0 g total acid. J. Research NBS 62, 207–211 (1959) RP2955.

which was not reagent grade. The data for the 12-g samples, the proper sample weight to give the correct ZnO/acid ratio in 740.00 g of acid, were subjected to analysis of variance. It was found that the first determination each day gave a significantly high mean value. The mean value of these 12 measurements was 257.92 cal/g with a standard error of 0.033 cal/g. Lot D was not included in the analysis. The analysis was repeated excluding the first determination each day, and there were found no significant differences among the 12 samples and no significant variation with time of day. The mean value for the 12 samples measured in triplicate was 257.82 cal/g at 25 °C with a standard error of 0.015 cal/g. The 0.10-cal/g higher average value found for the first sample each day may have been due to inadequate cooling in the desiccator, since this sample was usually cooled for about an hour instead of the two or more hours for subsequent samples. The change in weight during the additional 1-hr storage in the desiccator was about 0.01 percent, one quarter of the percentage change in the heat of solution. Parker and Nurse [17], desiccating with $CaCl_2$, found a somewhat larger change in weight.

Included in the data in table 6 are heats of solution obtained with different weights of sample. Figure 2 shows these data, including all determinations. The individual points in this figure are the mean values from table 6. The vertical lines show the total spread of all determinations at a given weight, 48 determinations in the case of the twelve 12-g samples plotted together. The progressively poorer precision as the sample size decreases is apparent in the figure if a comparison is made between the spread for the four determinations for zinc oxide D and the spread found for the three or four determinations each for the 1.5- and 0.2-g samples of lot B. Also plotted in figure 2 are the recalculated small-sample values given by Newman [9]. These overlap the values obtained for zinc oxide B in the present series. Because of the low precision for small samples, little confidence can be placed in the apparent increase in heat of solution with sample weight shown in this part of the figure. Except for zinc oxide lot B, however, there is a significant difference in the results for 9-g and 12-g samples. Zinc oxide lots E and F were heated and ground at different times from the same source. For the same weight of sample there is no difference between E and F either in the same or in different acids. The increases in heat of solution between 9-g and 12-g samples for E and F are significant, however, although not as large as found for lot A. The average difference in heat of solution between 9- and 12-g samples is about 0.28 cal/g^2, and an effect of this magnitude should be considered when examining differences in the heats of solution of zinc oxide samples in this weight range.

3.2. Recalculated Data

Stenzel and Morris [4, table IV] determined the heat of solution of three different lots of zinc oxide over a period of about 6 months. Using, presumably, their various appropriate (by date) values of the energy equivalent of their calorimeter, they obtained heats of solution of 256.68 ± 0.02, 256.62 ± 0.06, and 256.15 ± 0.10 cal/g, all originally assumed to be at 30 °C [4,5], but probably at a final calorimeter temperature of 31.5 °C [8, pp. 579, 580, 589]. The average of all nine determinations was 256.48 ± 0.09 cal/g. Stenzel and Morris reported, however, that if the average of their seven reported energy-equiva-

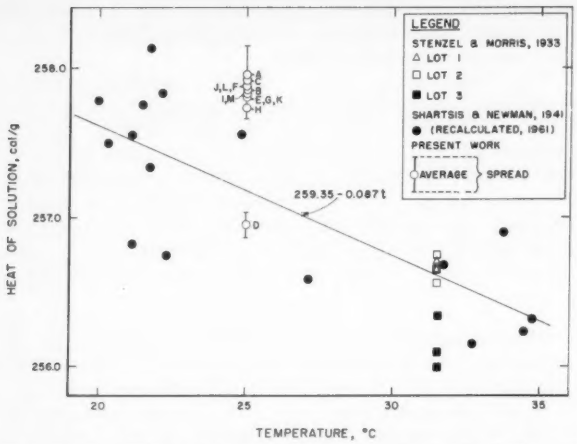

FIGURE 3. *Effect of temperature on the heat of solution of zinc oxide in nitric-hydrofluoric acid.*

Recalculated data. The zinc oxide was heated 1 hr at 950 °C, ground to pass a No. 100 sieve, and reheated for 5 min before introduction. A ratio of 12 g ZnO/740 g acid was used except for Stenzel and Morris data [Ind. Eng. Chem. Anal. Ed. **6**, 246-9 (1934)] for which the sample size is not known, and the temperature of reaction was assumed to be 31.5 °C. (1 cal=4.1840 j).

lent values was used to calculate all the heats of solution, the average heat of solution obtained was 256.1 cal/g, almost the lowest of their individual experimental values. This computation could not be repeated by the present author since it was not known which of the calibration values was used for each heat-of-solution determination, and the individual corrected temperature rises per gram of zinc oxide could not be determined. It seems likely, however, that the reported average heat of solution of the zinc oxide should have been higher. A statistical test [15] of the few data given indicates that the heat of solution of their third lot of zinc oxide was significantly lower than those of the other two. If this lot were eliminated, the individual average value for the other two would be 256.65 ± 0.03 cal/g.

Shartsis and Newman [5] calibrated their calorimeter for average temperatures ranging from 14 to 35 °C. A new least-squares linear equation relating energy equivalent and average temperature has been obtained from a recalculation of their calibration data. Values of the energy equivalent calculated from this equation were used in recalculating their heats of solution. Figure 3 shows their heat-of-solution data as recomputed in 1961, plotted as ordinates against the final calorimeter temperature as abscissas. The equation of the least-squares straight line through these data is $y=259.35-0.087\ t$, where y is cal/g and t is °C. The standard error of the slope is 0.013 cal/g-deg. The heat of solution of zinc oxide at 25 °C from this equation is 257.2 cal/g. The data as originally calculated gave a 25 °C value of 257.0 cal/g and a slope of 0.087 cal/g-deg. Considering the scatter [4] of their data, Shartsis and Newman did not wish to change the value 256.1 cal/g given by Stenzel and Morris, but it seems now that they may have been overcautious, particularly if the latter authors' values were at 31.5 °C as plotted in figure 3. The data shown in this figure indicate that the value 256.6 cal/g at 25 °C is probably low.

[4] The value 0.14 erroneously given as the standard deviation of the mean [5, p. 909] was actually s_y^2, the mean square of the deviations of the observed points about the line. The recalculated value is 0.16, giving 0.4 cal/g as a measure of the scatter of the observed points about the fitted line.

3.3. Comparison of Results

The mean value for the heat of solution of zinc oxide obtained in this work is about half a percent higher than the specification value. If there is a systematic calibration error in the present work it has not been apparent, although the heat of solution found for potassium chloride is a quarter of a percent greater than the tentative "best" value. This difference, however, is not statistically significant. The energy equivalent for the calorimeter containing acid A is 0.12 percent less than the values obtained for the other two batches, a difference the cause for which is not known. The heat of solution of the 9-g samples of zinc oxide A (table 6) in this acid was 257.37 ± 0.044 cal/g, in acid B it was 257.43 ± 0.065 cal/g. It is perhaps improper to compare the still earlier work with 9-g samples of zinc oxide A heated for 2 hr at 950 °C (table 3) with the results for standard-treated samples in table 6, but table 3 shows that differences in temperature of heating are not critical, while the results for lot H agreed with the others in table 6 although it was heated for 17 hr instead of 1 hr before grinding. Making the comparison, the samples of zinc oxide lot A heated 2 hr at 950 °C (table 3) had an average heat of solution in acid A of 257.25 ± 0.073 cal/g, while after the standard treatment its heat of solution in the same acid was 257.37 ± 0.044 cal/g (table 6). This difference also is not significant, although the effect of changing both the heat treatment and the acid is significant at the 5-percent probability level.

It seemed possible that there had been a real change in the purity or form of reagent zinc oxide with a corresponding change in its heat of solution since Stenzel and Morris determined it. Sample D of the present series, made by the American process directly from the ore, had a distinctly lower heat of solution than the others, exemplified by B and C made from the metal, but not as low as 256.6 cal/g. Sample D, however, was not of reagent grade and behaved differently on heating in that it did not shrink in the crucible, but remained a fine fluffy powder that could not be passed through a No. 100 sieve by shaking alone. Correspondence with a manufacturer has indicated that reagent zinc oxide made by the same process used today was well established on the market in 1933 and available to Stenzel and Morris. Thus it appears that there has probably been no substantial change in the purity or form of the reagent-grade zinc oxide used.

Stenzel and Morris do not give the final temperature of their calorimeter, but Biddle and Kelley [8], whose procedures the former authors were presumably following, operated their calorimeter ending at about 1.5 deg above the bath temperature. Stenzel and Morris also do not state the quantity of zinc oxide used in their calorimeter, but in accordance with the usual procedure, it would have been an amount causing about the same temperature rise as

a 6-g cement sample. On this basis, a sample of about 13-g of ZnO would have been used in 1222.5 g of acid, and a final temperature of about 31.5 °C would have been reached. If the average heat of solution for their lots of zinc oxide No. 1 and No. 2, 256.65 cal/g, is corrected to 25 °C using the temperature coefficient 0.09 cal/g-deg from figure 1, and the value thus obtained is corrected from the ZnO/acid weight ratio of 13/1222.5 to 7/425 by the average difference found from figure 3, a heat of solution of 257.6 cal/g is obtained. This value is in reasonable agreement with that found in the present work. The results obtained by Shartsis and Newman were less precise than those obtained either by Stenzel and Morris or in the present work, and the recalculated 25 °C value of 257.2 cal/g obtained from their work is essentially in agreement also.

4. Conclusions

Measurements have shown no significant difference between the heats of solution of heat-treated reagent zinc oxide from widely differing sources. As a consequence, heat-of-solution calorimeters calibrated with this substance in different laboratories, and even in different countries, should not be in disagreement because of differences in the calibrating standard. Accordingly, any differences found in portland-cement heat-of-hydration measurements between laboratories anywhere in the world are likely to be due to differences in sample-handling techniques between different laboratories or between different operators.

The heat of solution of 256.6 cal/g at 25 °C assigned to "standard" heat-treated zinc oxide by various cement specifications appears to be about half a percent low. Consequently, the heats of hydration measured with calorimeters calibrated with ZnO are also low by the same percentage. Since the coefficient of variation for heats of hydration is likely to be substantially larger than 2 percent, this half-percent difference is not serious. However, heats of solution determined in electrically calibrated and in zinc oxide calibrated calorimeters will disagree, and this disagreement may cause concern.

The heat of solution of zinc oxide in nitric-hydrofluoric acids appears to be affected only slightly by heating the ZnO at temperatures between 310 and 950 °C, slight decreases in the heat of solution (when calculated to the 950 °C ignited weight) being offset by slight decreases in the content of residual volatile material as the temperature of heating is increased. Consequently small changes in the temperature or time of heating of the zinc oxide will be without significant effect on the calculated heat capacity of cement calorimeters.

Small changes in the ZnO/acid weight ratio from the specification value of 7/425 are without significant effect from the standpoint of cement calorimetry, but changes as large as 25 percent from this ratio should be avoided.

The 1-hr heating of zinc oxide at 950 °C and its subsequent grinding and reheating can be eliminated from the specification. It would suffice to require only a 2-hr heating of the calorimeter sample with subsequent cooling in a desiccator for 2 hr over magnesium perchlorate and weighing before introduction into the calorimeter.

The heat of solution of standard-heat-treated analytical-reagent-grade zinc oxide at 25 °C in HNO_3, $0.28HF,26.4H_2O$ (8.0 ml 48%HF+2.00*N* HNO_3 to total 425.0 g) at a ZnO/acid weight ratio of 7/425 was measured as 257.82 cal/g, with a standard error of 0.015 cal/g. The temperature coefficient of this reaction is −0.087 cal/g-deg C, with a standard error of 0.013 cal/g-deg C. Independent measurement of these values by others would be desirable.

The assistance of John H. Gibb, guest worker, in preparing the recrystallized potassium chloride and participating in measurements of its heat of solution, is gratefully acknowledged. Thanks are also due to J. H. Welch of the Building Research Station, Garston, England, to F. Gille of the Forschungsinstitut der Zementindustrie, Dusseldorf, West Germany, and to Renichi Kondo of the Tokyo Institute of Technology, Tokyo, Japan, who graciously provided samples of reagent zinc oxide from their respective countries.

5. References

[1] Federal Test Method Standard No. 158a. Method 3101.1, General Services Administration, Washington, D.C. (1960).
[2] ASTM Standards. Designation C 186–55. Heat of hydration of portland cement, American Society for Testing Materials, Philadelphia 3, Pa. (1960).
[3] British Standard No. 1370–1958, British Standards Institution, London (1958).
[4] R. W. Stenzel and S. B. Morris. Ind. Eng. Chem., Anal. Ed., **6,** 246–49(1934).
[5] L. Shartsis and E. S. Newman, Proc. Am. Soc. Testing Materials **43,** 905–16(1943).
[6] W. A. Roth and P. Chall, Z. Elektrochem. **34,** 185–99 (1928).
[7] R. B. Peppler and E. S. Newman, J. Research NBS **26,** 121–23(1951) RP2183.
[8] S. B. Biddle, Jr., and J. W. Kelly, Proc. Am. Soc. Testing Materials **33,** 571–89(1933).
[9] E. S. Newman, J. Research NBS **62,** 207–11(1959) RP2955.
[10] H. A. Berman and E. S. Newman, J. Research NBS **65A** (Phys. and Chem.) No. 3, 197–207(1961).
[11] E. S. Newman and L. S. Wells, J. Research NBS **20,** 825–36(1938) RP1107.
[12] E. S. Newman, J. Research NBS **57,** 27–30(1956) RP2690.
[13] W. P. White, The Modern Calorimeter, Am. Chem. Soc. Monograph No. 49, The Chemical Catalog Co., New York (1928).
[14] F. D. Rossini, D. D. Wagman, W. H. Evans, S. Levine, and I. Jaffe, Selected values of chemical thermodynamic properties, NBS Circ. 500(1952).
[15] W. J. Youden, Statistical Methods for Chemists. p. 24 John Wiley & Sons, New York, (1951).
[16] International Critical Tables. **3,** 58; **5,** 122, National Research Council (McGraw-Hill Book Co., New York, 1933).
[17] T. W. Parker and R. W. Nurse, Cement and Lime Manufacture, **26,** No. 1,1–8 (1953).
[18] J. Coops, G. Somsen, and M. W. Tolk, The use of potassium chloride as a standard substance in solution calorimetry, Calorimetry Conference, Ottawa. (1961).
[19] Vivian Barfield, Preliminary Report, National Bureau of Standards, Calorimetry Conference, Ottawa. (1961).

(Paper 66A5–173)

JOURNAL OF RESEARCH of the National Bureau of Standards—A. Physics and Chemistry
Vol. 66A, No. 5, September–October 1962

Nuclear Optical Model Analysis of Neutron Elastic Scattering for Calcium*

Randall S. Caswell

(May 14, 1962)

A nuclear optical model calculation of neutron elastic scattering using five parameters has been made. Appropriate estimates of the effect of compound elastic scattering at low energies are included. Comparisons have been made with experimental data, and results for the parameters adopted are given for elastic scattering in the energy range from 0.734 to 18 Mev. Although reasonably good agreement between the calculation and experimental results have been obtained, there is a discrepancy between experiments below 2 Mev, and experimental data is needed between 6 and 14 Mev. Both angular distributions and Legendre expansion coefficients for the total elastic scattering are given.

1. Introduction

The nuclear optical model has been outstandingly successful in describing the elastic scattering of neutrons and other nuclear particles above the energy of perhaps 6 Mev, where compound elastic scattering processes are not important. Below these energies it is necessary to include some estimate of compound elastic scattering. At neutron energies below the first excited state of the target nucleus, inelastic scattering is not possible. In this energy range it is possible to describe the compound elastic scattering by use of the fluctuation cross section [Feshbach, 1960]. Above this energy the angular distribution of the compound elastic scattering may be obtained from the compound statistical model [Hauser and Feshbach, 1952].

Initially in the present work the experimental data was analyzed using the six-parameter nuclear optical model of Bjorklund and Fernbach [1958]. However, it was found that at least as good fits to the experimental data could be obtained with a five-parameter model, using derivative surface absorption instead of an adjustable parameter to determine the width of the imaginary (absorptive) well. This latter model, which contains a Saxon real potential, a Thomas spin-orbit potential, and a surface imaginary potential, was used in this calculation.

This calculation is the first of a series which will provide data in a form suitable for input to neutron penetration calculations with digital computers. The present calculations are for calcium, an important component of concrete which is widely used for neutron shielding. Comparisons with experimental elastic scattering angular distributions are included. Angular distributions and Legendre coefficients for the calculated angular distributions are both presented. The calculations have been programed in Fortran for the IBM 7090 computer at the National Bureau of Standards.

*This work was sponsored by Defense Atomic Support Agency.

2. Description of the Calculation

2.1. Solution of the Wave Equation

Although the exact phase shift analysis carried out here is standard in many respects, it seems desirable to record the specific method of calculation, including the Legendre polynomial analysis.

We start with the radial part of the non-relativistic Schrödinger wave equation:

$$\frac{d^2U_l(r)}{dr^2}+\frac{2m}{\hbar^2}\left[E-\frac{l(l+1)\hbar^2}{2mr^2}-(V(r)+iW(r))\right]\times U_l(r)=0. \quad (1)$$

The potential is described by $V(r)+iW(r)$ where $V(r)$ is the real part of the potential and $W(r)$ is the imaginary part. The wave function $U_l(r)$ will also have both real and imaginary parts:

$$U_l(r)=X_l(r)+iY_l(r). \quad (2)$$

Equation (1) becomes:

$$\frac{d^2(X_l+iY_l)}{dr^2}+\frac{2m}{\hbar^2}\left[E-\frac{l(l+1)\hbar^2}{2mr^2}-V-iW\right]\times(X_l+iY_l)=0. \quad (3)$$

Separating this equation into real and imaginary parts, we obtain two coupled real equations which may be solved on the computer.

$$\frac{d^2X_l}{dr^2}+\frac{2m}{\hbar^2}\left[E-\frac{l(l+1)\hbar^2}{2mr^2}-V\right]X_l+\frac{2m}{\hbar^2}WY_l=0 \quad (4)$$

$$\frac{d^2Y_l}{dr^2}+\frac{2m}{\hbar^2}\left[E-\frac{l(l+1)\hbar^2}{2mr^2}-V\right]Y_l-\frac{2m}{\hbar^2}WX_l=0. \quad (5)$$

These equations are integrated step-by-step outward in radius by the second order Runge-Kutta method [see, for example, Zurmühl, 1961]. The number of

integration steps is typically 100 to 500. If the wave functions become large, they are automatically renormalized to smaller values by the code. The running time for 15 l's and 200 steps is about 1 min per energy including all angular distributions. The mass appearing in these equations is the reduced mass of the neutron in the neutron-nucleus center-of-mass system. The energy, E, is that of the neutron in the center-of-mass system. When the complex potential $(V+iW)$ approaches a non-vanishing constant at the origin, then

$$U_l(r)\to C_l r^{l+1} \text{ as } r\to 0 \tag{6}$$

where C_l is a complex number independent of r [Amster, Leshan, and Walt, 1960]. In the presence of the spin-orbit term (see below) there is a $1/r$ behavior of the potential energy for small values of r; however, eq (6) still holds since this term is dominated by the $1/r^2$ dependence of the centrifugal potential [see Bohm, 1951]. Since the cross sections depend only on the logarithmic derivative of the wave function, the normalization is arbitrary and C_l can be taken to be any non-zero value. We have chosen $k(1+i)$ for C_l where k is a small number chosen to prevent underflow or overflow problems. Provision is made in the code to calculate for values of l up to $l=29$.

For the optical model parameters we have used a potential whose real and imaginary parts are:

$$V(r)=V_c\rho(r)-\alpha V_c\left(\frac{\hbar}{2Mc}\right)^2(\vec{l}\cdot\vec{\sigma})\frac{1}{r}\frac{d\rho}{dr}, \tag{7}$$

$$W(r)=W_s\left(4a\frac{d\rho}{dr}\right)=W_s\left(4\rho^2\exp\left[\frac{r-R_0}{a}\right]\right) \tag{8}$$

where

$$\rho(r)=\frac{1}{1+\exp\left[\dfrac{r-R_0}{a}\right]},$$

the usual "Saxon" potential; α is the strength of the spin-orbit interaction relative to the "Thomas" term for a nucleon; M is the neutron mass; V_c is the central real potential; W_s is the lowest value of the imaginary surface potential; $\dfrac{\hbar}{Mc}$ is the Compton wavelength for a nucleon; $\vec{l}$ is the orbital angular momentum of the neutron; $\vec{\sigma}$ is the Pauli spin operator of the incident neutron; R_0 is the nuclear radius; and a is the "diffuseness" parameter of the real potential. If the spin angular momentum of the incident neutron is parallel to the orbital angular momentum of the incident neutron, then $j=l+1/2$, and $\vec{\sigma}\cdot\vec{l}=l$. If the spin and orbital angular momentum are anti-parallel, then $j=l-1/2$ and $\vec{\sigma}\cdot\vec{l}=-(l+1)$. This leads to two real potentials, $V^+(r)$ and $V^-(r)$ corresponding to the parallel and anti-parallel $\vec{\sigma}\cdot\vec{l}$ interactions. The wave equation is solved for each of these. To obtain the desired cross sections, we need the phase shifts η_l^+ and η_l^- which measure the effect of the complex potential on the neutron partial waves. These phase shifts are obtained by a calculation which compares the value for logarithmic derivative f_l obtained by numerical integration in the presence of the nuclear potential with the corresponding quantity (Δ_l+iS_l) for the zero phase shift spherical Hankel function solutions obtained in the absence of the nuclear potential.

The required expression for η_l is given by Blatt and Weisskopf [1952]:

$$\eta_l=\frac{f_l-\Delta_l+iS_l}{f_l-\Delta_l-iS_l}\exp(2i\xi_l). \tag{9}$$

For neutrons

$$\exp(2i\xi_l)=\frac{G_l(R)-iF_l(R)}{G_l(R)+iF_l(R)}, \tag{10}$$

where $G_l(R)$ and $F_l(R)$ are solutions of eq (1) with $(V(r)+iW(r))=0$. In terms of spherical Bessel functions, $F_l(x)=xj_l(x)$ and $G_l(x)=xn_l(x)$ where $x=kR$.

2.2. Evaluation of the Cross Sections Directly From the Nuclear Optical Model

The total cross section predicted by the nuclear optical model is made up of a shape-elastic scattering cross section and a compound nucleus formation cross section [Feshbach, Porter, and Weisskopf, 1954]:

$$\sigma_t=\sigma_e+\sigma_c.$$

However, the compound nucleus may decay into the entrance channel producing "compound elastic" scattering or it may produce inelastic scattering or charged particle reactions:

$$\sigma_c=\sigma_{ce}+\sigma_r.$$

These equations may now be rearranged to separate the elastic scattering (σ_{se} and σ_{ce} are not distinguishable experimentally) from the reaction cross section:

$$\sigma_t=(\sigma_{se}+\sigma_{ce})+\sigma_r=\sigma_e+\sigma_r.$$

In the present calculation σ_{ce} is estimated by the "fluctuation" cross section, σ_{fl}, which is important below energies of about 6 Mev:

$$\sigma_t=\sigma_{se}+\sigma_{fl}+\sigma_r.$$

When inelastic scattering and reactions are zero or negligible, the entire cross section is elastic:

$$\sigma_t=\sigma_{se}+\sigma_{fl}.$$

In this case the fluctuation cross section may be obtained very simply from the phase shifts of the optical model alone (see Feshbach [1960] for a discussion of the fluctuation cross section).

We now proceed to evaluate the various cross sections from the calculated phase shifts (η_l's). For both incident particles and the nucleus without spin, the expressions for the incident plane wave, the total wave (which shows the effect of the potential of the nucleus on the incident wave), and the scattered wave are:

$$e^{ikz}=\sum_{l=0}^{\infty} i^l \frac{2l+1}{2}[h_l^*(kr)+h_l(kr)]P_l(\cos\theta), \quad (11)$$

$$\psi_{\text{tot}}(r)=\sum_{l=0}^{\infty} i^l \frac{2l+1}{2}[h_l^*(kr)+\eta_l h_l(kr)]P_l(\cos\theta), \quad (12)$$

and

$$\psi_{\text{scatt}}(r)=\psi_{\text{tot}}(r)-e^{ikz}$$
$$=\sum_{l=0}^{\infty} i^l \frac{2l+1}{2}(\eta_l-1)h_l(kr)P_l(\cos\theta). \quad (13)$$

The incident neutrons which have spin 1/2 may be represented by a plane wave:

$$\psi_{\text{inc}}=e^{ikz}\chi_{\text{inc}} \quad (14)$$

where χ_{inc} describes the spin wave function of the neutron. $\chi_{\text{inc}}=\binom{1}{0}$ is spin "up." $\chi_{\text{inc}}=\binom{0}{1}$ corresponds to spin "down." In the presence of the nuclear potential the asymptotic form of the wave function of the neutron is:

$$\psi \xrightarrow[r\to\infty]{} \psi_{\text{inc}}+\frac{1}{r}e^{ikr}F(\theta)\chi_{\text{inc}} \quad (15)$$

where $F(\theta)$ is the scattering matrix.

$$F(\theta)=A(\theta)+B(\theta)\vec{\sigma}\cdot\vec{n} \quad (16)$$

where $\vec{n}$ is a unit vector perpendicular to the plane of scattering. According to the Basel convention [Huber and Meyer, 1961], the positive direction of polarization, given by the unit vector $\vec{n}$, is:

$$\vec{n}=\frac{\vec{k}_i\times\vec{k}_f}{|\vec{k}_i\times\vec{k}_f|} \quad (17)$$

where $\vec{k}_i$ and $\vec{k}_f$ are the wave vectors of the incident and scattered neutrons.

In the equations above, $h_l^*=j_l-in_l$ and represents an incoming spherical wave and $h_l=j_l+in_l$ and represents an outgoing spherical wave. To extend this treatment to the case of neutrons with spin incident on spin-zero nuclei [Lepore, 1950], we introduce the operators π_l^+ and π_l^- which select the states for which $j=l+\frac{1}{2}$ and $j=l-\frac{1}{2}$, respectively. These operators are

$$\pi_l^+=\frac{l+1+\vec{\sigma}\cdot\vec{l}}{2l+1} \text{ and } \pi_l^-=\frac{l-\vec{\sigma}\cdot\vec{l}}{2l+1}. \quad (17a)$$

If $j=l+\frac{1}{2}$, $\pi^+=1$, $\pi^-=0$. If $j=l-\frac{1}{2}$, $\pi^+=0$, $\pi^-=1$. Applying our operators to the total wave function, eq (16) we have

$$\psi_{\text{tot}}=\sum_{l=0}^{\infty}\frac{2l+1}{2}i^l[\pi^++\pi^-][h_l^*(kr)+\eta_l h_l(kr)]$$
$$\times P_l(\cos\theta)\chi_{\text{inc}}. \quad (17b)$$

Let η_l^+ and η_l^- be phase shifts corresponding to the parallel and anti-parallel spin-orbit orientations for the neutron. At large radii we use the asymptotic form of the Hankel functions,

$$\psi_{\text{tot}}=\sum_{l=0}\frac{(2l+1)i^l}{2ikr}\left\{\pi_l^+\left(\eta_l^+e^{i\left[kr-(l+1)\frac{\pi}{2}\right]}\right.\right.$$
$$\left.+e^{-i\left[kr-(l+1)\frac{\pi}{2}\right]}\right)+\pi_l^-\left(\eta_l^-e^{i\left[kr-(l+1)\frac{\pi}{2}\right]}\right.$$
$$\left.\left.+e^{-i\left[kr-(l+1)\frac{\pi}{2}\right]}\right)\right\}\times P_l(\cos\theta)\chi_{\text{inc}}. \quad (17c)$$

If we now subtract the incident wave from the total wave to obtain the scattered wave, we find

$$\psi_{\text{scatt}}=\sum_{l=0}^{\infty}\frac{e^{ikr}}{2ikr}\Big[(l+1)(\eta_l^+-1)+l(\eta_l^--1)$$
$$+(\eta_l^+-\eta_l^-)\vec{\sigma}\cdot\vec{l}\Big]P_l(\cos\theta)\chi_{\text{inc}}, \quad (18)$$

where we have used the expressions (17a) for the operators and the condition that when $\eta_l^+=\eta_l^-=1$, ψ_{scatt} must equal zero. The right-left asymmetry in the scattering of a polarized beam is introduced through the $(\vec{\sigma}\cdot\vec{l})$ operator:

$$(\vec{\sigma}\cdot\vec{l})P_l(\cos\theta)=\vec{\sigma}\cdot\left[\vec{n}\left(-i\frac{\partial}{\partial\theta}\right)P_l(\cos\theta)\right]. \quad (19)$$

However, $\frac{\partial}{\partial\theta}=-\sin\theta\frac{\partial}{\partial(\cos\theta)}$. Finally,

$$(\vec{\sigma}\cdot\vec{l})P_l(\cos\theta)=(\vec{\sigma}\cdot\vec{n})\left[i\sin\theta\frac{\partial}{\partial(\cos\theta)}P_l(\cos\theta)\right], \quad (20)$$

$$(\vec{\sigma}\cdot\vec{l})P_l(\cos\theta)=(\vec{\sigma}\cdot\vec{n})iP_l^1(\cos\theta). \quad (21)$$

where $P_l^1(\cos\theta)=\sin\theta\frac{\partial}{\partial(\cos\theta)}P_l(\cos\theta)$. Note: a $(-1)^m$ term is sometimes included in the definition of the associated Legendre function $P_l^m(\cos\theta)$, in which case our function has the opposite sign, and a minus sign appears on the right side of eq (21). $A(\theta)$ and $B(\theta)$ appearing in the scattering matrix, eq (16) are:

$$A(\theta)=\frac{1}{2ik}\sum_{l=0}^{\infty}[(l+1)(\eta_l^+-1)+l(\eta_l^--1)]P_l(\cos\theta) \quad (22)$$

$$B(\theta)=\frac{1}{2k}\sum_{l=1}^{\infty}[\eta_l^+-\eta_l^-]P_l^1(\cos\theta). \quad (23)$$

The differential scattering cross section is

$$\frac{d\sigma}{d\Omega}=\frac{1}{2}\,trF^+F=|A|^2+|B|^2. \quad (24)$$

The polarization is given by

$$P=\frac{2\ \mathrm{Re}\ (A^*B)}{|A|^2+|B|^2}. \quad (25)$$

For a completely polarized incident beam with spin "up," $P=(L-R)/(L+R)$, where L and R are the measured left and right detector counting rates.

The total, compound nucleus formation, and shape elastic cross sections (integrated over angle) are:

$$\sigma_t=\frac{\pi}{k^2}\sum_{l=0}^{\infty}[(l+1)2\ \mathrm{Re}\ (1-\eta_l^+)+l\,2\ \mathrm{Re}\ (1-\eta_l^-)] \quad (26)$$

$$\sigma_c=\frac{\pi}{k^2}\sum_{l=0}^{\infty}[(l+1)(1-|\eta_l^+|^2)+l(1-|\eta_l^-|^2)] \quad (27)$$

$$\sigma_{se}=\frac{\pi}{k^2}\sum_{l=0}^{\infty}[(l+1)|1-\eta_l^+|^2+l|1-\eta_l^-|^2]. \quad (28)$$

For use in inelastic scattering calculations and in our estimate of compound elastic scattering, the "transmission coefficients" are also calculated:

$$T_l^+=(1-|\eta_l^+|^2)\ \text{and}\ T_l^-=(1-|\eta_l^-|^2). \quad (29)$$

2.3. Compound Elastic Scattering

Whereas shape elastic scattering is given directly by the nuclear optical model, our estimate of compound elastic scattering is treated in four different ways depending upon the incident neutron energy. Below 3.35 Mev, it may be obtained from the optical model phase shifts, with a small correction for the observed (n, p) cross section. In the energy range from 3.35 to 5.0 Mev, a Hauser-Feshbach [1952] hand calculation using discrete energy levels of the target nucleus (see fig. 1) was made. From 5.0 to 5.7 Mev a Hauser-Feshbach calculation using a statistical-model residual nucleus was made. In this case the compound elastic scattering is isotropic because of the randomness of the spins and parities of the levels assumed in the statistical model. The angular isotropy has been proved by Wolfenstein [1951] and by Hauser and Feshbach. Above 6 Mev compound elastic scattering is neglected.

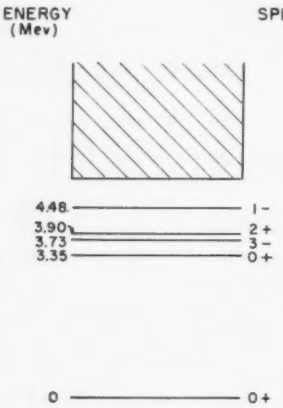

FIGURE 1. *Low-lying energy levels of* Ca^{40}.

Spins and parities in parentheses are taken from Troubetzkoy, Kalos, Lustig, Ray, and Trupin [1961]. Levels taken as a continuum above 5 Mev.

The fluctuation cross section, in the absence of inelastic scattering and reactions, may be obtained from the phase shifts of the optical model [Feshbach, 1960]:

$$|A|^2_{jl}=\frac{1}{4k^2}\sum_{l=0}^{\infty}\{(l+1)^2(1-|\eta_l^+|^2)^2+l^2(1-|\eta_l^-|)^2\}\times[P_l(\cos\theta)]^2$$

$$|B|^2_{jl}=\frac{1}{4k^2}\sum_{l=1}^{\infty}\{(1-|\eta_l^+|^2)+(1-|\eta_l^-|^2)\}[P_l^1(\cos\theta)]^2. \quad (30)$$

At energies below the energy of the first excited state in the target nucleus (3.35 Mev for Ca^{40}), we have used eq (30) to calculate the compound elastic scattering. Note that this leads not to isotropic scattering but to an angular distribution which goes predominantly as $[P_l(\cos\theta)]^2$ for neutrons of angular momentum l.

The cross section for inelastic scattering of a neutron of incident angular momentum l, final angular momentum l', from a nucleus of initial angular momentum i and final angular momentum i' is given by Hauser and Feshbach as

$$\sigma(l,i|l',i')=\frac{1}{2(2i+1)}\sum_{\alpha,\beta}\sigma(l,j_\alpha|l',j'_\beta|\theta) \quad (31)$$

where

$$\sigma(l,j|l',j'|\theta)=\frac{\pi}{k^2}(2l+1)T_l(E)\sum_J \frac{A_J(l,j|l',j'|\theta)}{1+\sum_{p,q,r}{}' T_p(E'_q)/T'_l(E')}, \quad (32)$$

and is the cross section for production of neutrons of energy E' of angular momentum l', channel spin j', moving in a direction θ. The r index refers to possible channel spins, p to possible final neutron angular momenta, E'_q to final neutron energies. J is the total angular momentum of the compound nucleus state. The prime on the summation indicates that we omit the term referring to the final neutron E', l', j' we are considering. As we shall see the denominator of eq (32) is essentially the branching ratio of the specific neutron transition under consideration versus all other possibilities. If we immediately specialize to the case of compound elastic scattering, $(E=E', l=l', j=j')$, consider spin zero nuclei only $(j=j'=\frac{1}{2}, i=0,$ and $J=l\pm\frac{1}{2})$, and T_l's as defined in eq (29), the angular distribution for the lth partial wave of compound elastically scattered

neutrons becomes:

$$\left(\frac{d\sigma}{d\Omega}\right)_{l_{CE}}=\frac{\pi}{2k^2}\left\{\frac{(l+1)T_l^+(E)}{1+\sum_{p,q,r}' T_P^+(E_q')/T_l^+(E)}\right.$$

$$A_{l+\frac{1}{2}}\left(l,\frac{1}{2}\middle|l,\frac{1}{2}\middle|\theta\right)+\frac{lT_l^-(E)}{1+\sum_{p,q,r}' T_P^+(E_q')/T_l^-(E)}$$

$$\left.A_{l-\frac{1}{2}}\left(l,\frac{1}{2}\middle|l,\frac{1}{2}\middle|\theta\right)\right\}. \quad (33)$$

The A-functions that occur in eq (33) are easily expressed in terms of Z-coefficients used by Blatt and Biedenharn [1952] and tabulated by Biedenharn [1953]:

$$A_J(l,j|l,j|\theta)=\frac{1}{4\pi(2l+1)}\sum_L[Z(lJlJ;jL)]^2P_L(\cos\theta). \quad (34)$$

The question of phases does not enter since the Z-coefficient appears only when squared. Note that these results appear naturally in a Legendre series expansion which may be easily combined with the Legendre coefficient expansion as determined by the computer for the shape elastic scattering. Equations (33) and (34) are used to calculate the region of discrete states of the target nucleus (3.35 to 5 Mev). A correction to the branching ratio appearing in eq (33) is applied to allow for experimentally observed reaction cross sections. From 5 to 5.7 Mev, the residual nucleus is considered as statistical, and the compound elastic scattering is isotropic.

2.4. Legendre Coefficient Analysis of the Elastic Scattering

The elastic scattering angular distribution is represented in the following way:

$$\frac{d\sigma}{d\Omega}(E,\theta)=\frac{\sigma_{\text{total elastic}}}{4\pi}\sum_l(2l+1)S_l(E)P_l(\cos\theta) \quad (35)$$

where $S_0(E)=1$.

The differential cross section as obtained from eq (24) appears as a sum of the products of two series:

$$\frac{d\sigma}{d\Omega}=\sum_l A_lP_l(\cos\theta)\sum_m A_mP_m(\cos\theta)$$

$$+\sum_l B_lP_l^1(\cos\theta)\sum_m B_mP_m^1(\cos\theta). \quad (36)$$

The first term in eq (36) may be represented by a single series of Legendre coefficients

$$\frac{d\sigma}{d\Omega}=\sum_k a_kP_k(\cos\theta), \quad (37)$$

where a_k is given by

$$a_k=\sum_{l=0}\sum_{m=0}A_lB_m\frac{C_{\frac{1}{2}(l-m+k)}C_{\frac{1}{2}(l+m-k)}C_{\frac{1}{2}(m-l+k)}}{C_{\frac{1}{2}(l+m+k)}}$$

$$\times\frac{2k+1}{l+m+k+1}, \quad (38)$$

where $C_j=\dfrac{1.3.5\ldots.(2j-1)}{j!}$; l,m are positive integers; $(l+m+k)$ is even; and $|l-m|\leq k\leq l+m$, that is, the three vectors satisfy the "triangle condition" [Whittaker and Watson, 1958].

The product of the two series in $P_l^1(\cos\theta)$ can be reduced to product of two series in $P_l(\cos\theta)$ which can then be solved by eq (38). First we express the $P_l^1(\cos\theta)$'s in terms of polynomial expansions in $P_l(\cos\theta)$ [see Morse and Feshbach, 1953]:

$$P_l^1(\cos\theta)=\frac{l(l+1)}{(2l+1)\sin\theta}[P_{l-1}(\cos\theta)-P_{l+1}(\cos\theta)] \quad (39)$$

$$P_m^1(\cos\theta)=\sin\theta[(2m-1)P_{m-1}(\cos\theta)$$

$$+(2m-5)P_{m-3}(\cos\theta)$$

$$+(2m-9)P_{m-5}(\cos\theta)+\ldots] \quad (40)$$

Any product term $P_l^1(\cos\theta)P_m^1(\cos\theta)$ resulting from the series product in eqs (36) may be expressed in terms of a product of expressions from eqs (39) and (40). Note that in the product $\sin\theta$ cancels out, leaving only terms in Legendre polynomials. Relations (38 to 40) were programed for the computer so that a Legendre coefficient analysis of the form of eq (35) could be directly obtained from the calculated phase shifts.

The calculation could equally well be done through use of vector-coupling coefficients [Edmonds, 1957]. It is expected that the problem for the computer would be about the same either way. The C_j coefficients used here are closely related to the Clebsch-Gordan coefficient $(ab00|abc0)$ as given in eq (5) of Blatt, Biedenharn, and Rose [1952].

3. Choice of Optical Model Parameters and Comparison With Experiment

Calcium is composed of 96.97 percent Ca^{40} with 2.06 percent of Ca^{44}, and smaller amounts of Ca^{42}, Ca^{43}, Ca^{45}, and Ca^{46}. In this calculation it is considered as pure Ca^{40} except that a slightly larger value of R_0 is used to approximate the effect of the other isotopes.

In the initial attempts to fit calcium neutron cross section data, the model of Bjorklund and Fernbach [1958] was used. The real potential is as described by eq (7), and the imaginary potential is a Gaussian absorption located at the surface:

$$W=W_s\exp\left[-\left(\frac{r-R_0}{b}\right)\right]^2. \quad (41)$$

This model, which has been quite successful in fitting neutron elastic scattering data at 4.1, 7, and 14 Mev, involves six parameters: R_0, V_c, α, a, W_s, and b. In attempting to fit this data, R_0 was held constant at 1.25 $A^{1/3}$ fermis, b at 0.980 fermis, α at 35. The average atomic weight was used for A. The other three parameters were varied. A problem of the optical model is the large number of arbitrary parameters. In an attempt to reduce the number of parameters, the width of the surface absorption, b, was eliminated as an independent parameter and derivative surface absorption used instead as given in eq (8). Somewhat surprisingly the agreement with the experimental data was considerably improved at 14.6 Mev, and was equally good at the energies of 2 Mev and below where data existed which could be directly compared with optical model predictions using the fluctuation cross section. The improved agreement at 14.6 Mev may be stated in another way; namely, the value of b (0.980 fermis) is too small at this energy, and a thicker shell of surface absorption of neutrons should be used. This is given automatically by the use of a derivative surface absorption.

Using the derivative surface absorption model, R_0 was held constant at $1.25A^{1/3}$ fermis, the value indicated by the work of Bjorklund and Fernbach, and also by the optical model analyses of proton polarization reported by Gursky and Stewart [1961]. Actually the parameters V_c and R_0 act very much like a single parameter $V_cR_0^n$ where n is equal to 2 at low energies and increases slightly with energy. Our choice is to hold R_0 fixed and vary V_c. The strength of the spin-orbit coupling, α, was also held at the value of 35 used by Bjorklund and Fernbach because it was felt that changes or improvements in this value should come from the analysis of polarization data to which α is more sensitive, rather than angular distribution data which is considered here. Three parameters were allowed to vary, V_c, W_s, and a. Although a could have been held fixed, independent of energy, at a value of about 0.580 fermis to obtain fairly good fits to the experimental data everywhere, it was found that better fits were obtained if a was taken as 0.600 fermis at 14.6 Mev and at 0.550 fermis below 2 Mev. Smooth curves drawn through the data were used to obtain parameters for the optical model calculations, even though local variations sometimes gave better fits (see fig. 2). This apparent jumping around of the experimental data is due at the low energies to the presence of resonances in the cross section, which the optical model averages over.

It should also be mentioned that a calculation which predicts the energy variation of the parameters of the optical model by use of a nonlocal potential has been made by Perey and Buck [1961]. The predictions of Perey and Buck have not been used here since it seemed unlikely that they would improve the cross section data.

Experimental data used for the parameter determination at 14.6 Mev were taken from Cross and Jarvis [1960]; below 2 Mev, the data of Seagrave, Cranberg, and Simmons [1958] and Lane, Langsdorf, Monahan, and Elwyn [1960] as collected by Howerton [1961] were used. Comparison of the calculation to experimental data is shown in figures 3 through 12. Comparison is also made to data at

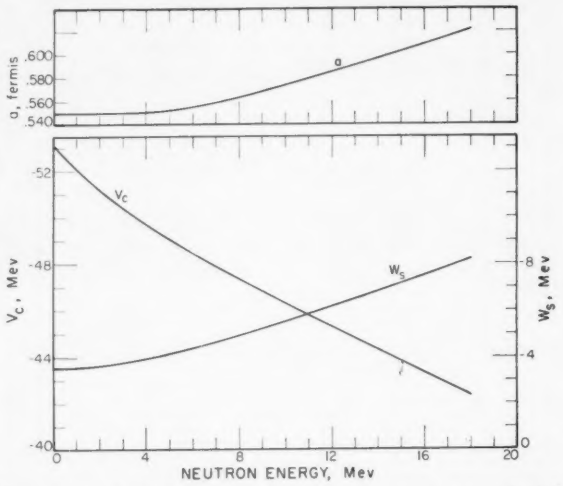

FIGURE 2. *Optical model parameters versus energy as adopted for the calculation.*

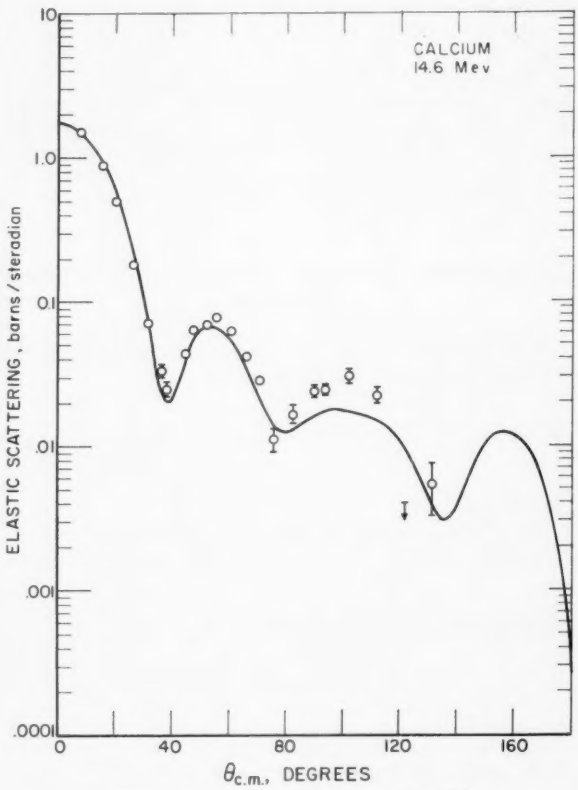

FIGURE 3. *Elastic scattering at 14.6 Mev.*

Experimental data are those of Cross and Jarvis [1960]. The curves in this and succeeding figures are from this calculation using the optical model parameters of figure 2.

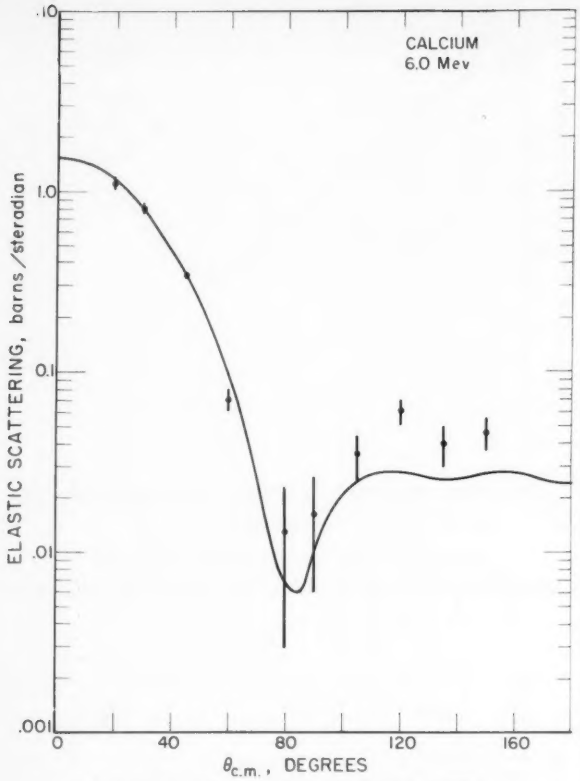

FIGURE 4. *Elastic scattering at 6.0 Mev.*
Experimental data are from Seagrave, Cranberg, and Simmons [1958].

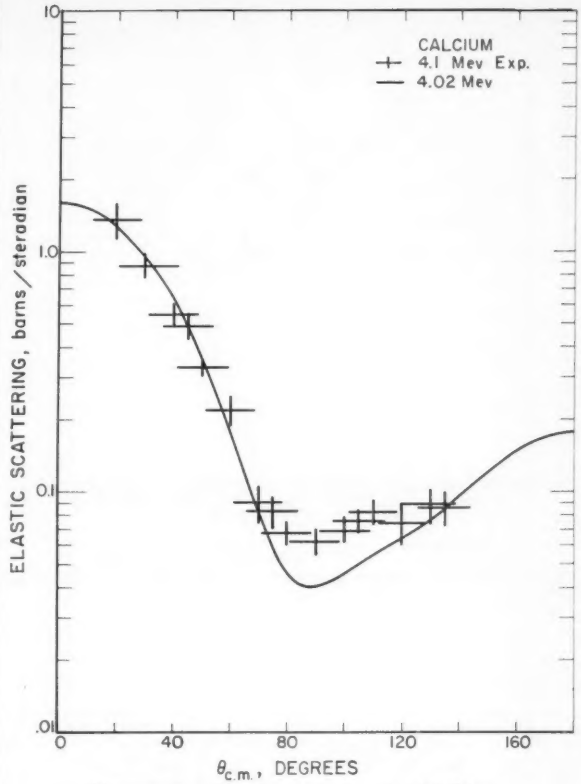

FIGURE 5. *Elastic scattering at 4.02 Mev.*
The calculation is compared to the 4.1 Mev experimental data of Vincent, Morgan, and Prud'homme [1960].

4.1 Mev of Vincent, Morgan, and Prud'homme [1960] and to an angular distribution of Seagrave, Cranberg, and Simmons [1958] at 6.0 Mev. Neither of these distributions was used to obtain the optical model fit because the Hauser-Feshbach hand calculation involved made parameter fitting quite difficult (it later turned out that at 6.0 Mev the compound elastic scattering could be neglected). Nevertheless the agreement between calculation and experiment is about the same here as at the other energies. We may therefore be reasonably confident that the calculation predicts the cross sections quite well where they have not been measured.

It would not be possible for these calculations to agree with both the Seagrave et al. and the Lane et al. experimental measurements, since these disagree with each other. In general the angular distributions of Lane et al. are more isotropic, while the distributions of Seagrave et al. have a larger cross section in the forward direction. Somewhat more weight was given to the Seagrave et al. experiment, since the geometry appears to be somewhat cleaner and less subject to multiple scattering effects which would tend to make the distributions too isotropic.

This optical model underestimates the magnitude of the non-elastic (or compound nucleus formation) cross section at 14.5 Mev. The calculation gives

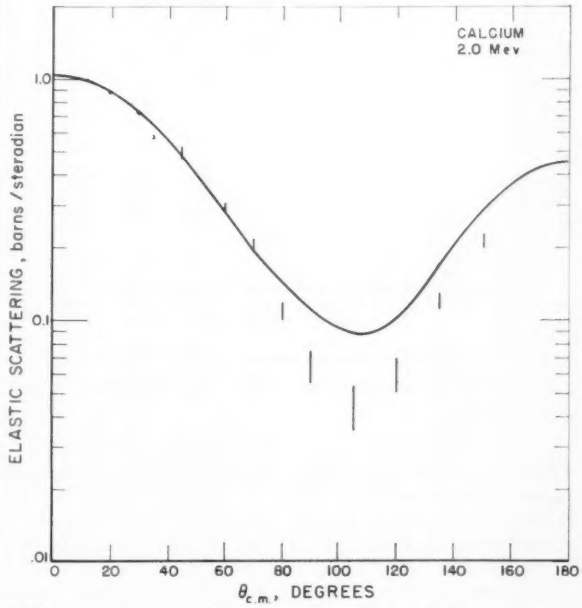

FIGURE 6. *Elastic scattering at 2.0 Mev.*
Experimental data are from Seagrave, Cranberg, and Simmons (1958).

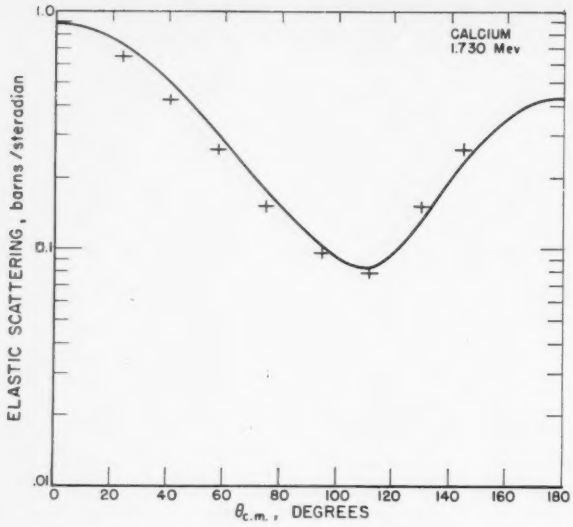

FIGURE 7. *Elastic scattering at 1.730 Mev.*
Experimental data are from Lane, Lane, Langsdorf, Monahan, and Elwyn 1960].

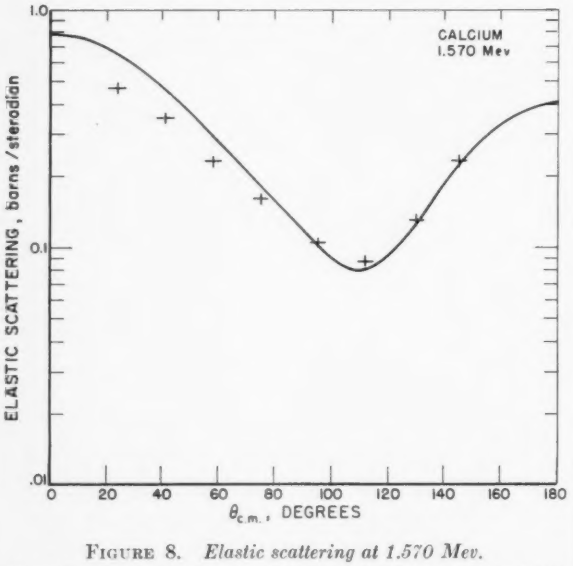

FIGURE 8. *Elastic scattering at 1.570 Mev.*
Experimental data are from Lane, Langsdorf, Monahan, and Elwyn [1960].

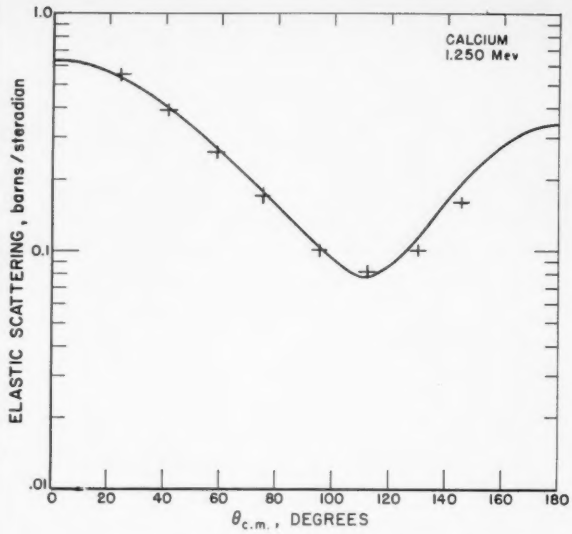

FIGURE 9. *Elastic scattering at 1.250 Mev.*
Experimental data are from Lane, Langsdorf, Monahan, and Elwyn [1960].

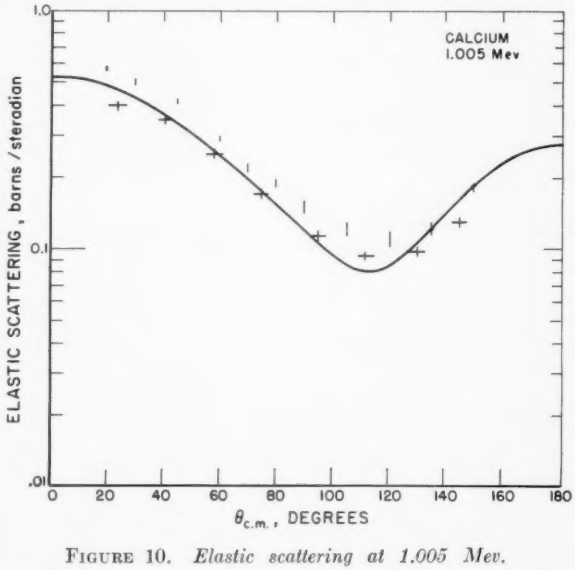

FIGURE 10. *Elastic scattering at 1.005 Mev.*
Experimental data are from Lane, Langsdorf, Monahan, and Elwyn [1960] at 1.01 ± 0.03 Mev (crosses) and from Seagrave, Cranberg, and Simmons [1958] at 1.0 Mev (vertical lines).

1.227 barns at 14.6 Mev, whereas the experimental measurement at 14.5 Mev of Flerov and Talyzin [1956] gives 1.36 ±0.02 barns. This leads to a corresponding error in the total cross section, but does not affect the elastic cross section values. The total elastic cross section at 14.6 Mev is 0.803 barns, in agreement with the experimental value of 0.82 ±0.07 barns of Cross and Jarvis.

4. Results of the Calculation

The calculated angular distributions for total elastic scattering are given in table 1 and the Legendre coefficient expansions are given in table 2.

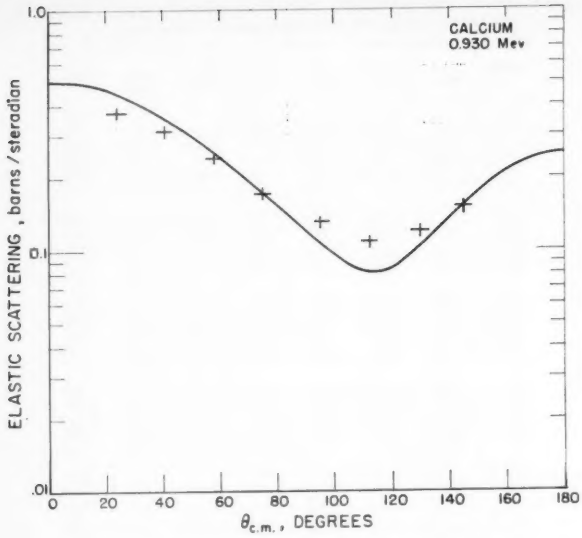

FIGURE 11. *Elastic scattering at 0.930 Mev.*
Experimental data are from Lane, Langsdorf, Monahan, and Elwyn [1960].

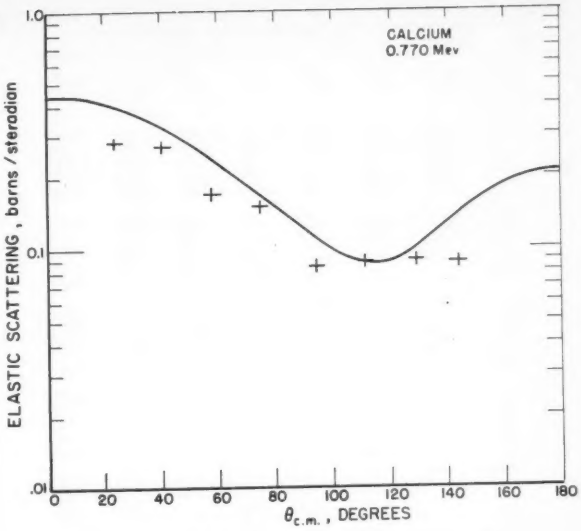

FIGURE 12. *Elastic scattering at 0.770 Mev.*
Experimental data are from Lane, Langsdorf, Monahan, and Elwyn [1960].

TABLE 1. *Angular distributions of neutron elastic scattering for calcium (barns/steradian)*

Angle	18.000 Mev	17.100 Mev	16.300 Mev	15.500 Mev	14.750 Mev	14.000 Mev	13.300 Mev
deg							
0.	2.2740	2.1727	1.9827	1.8448	1.7511	1.6825	1.5868
5.0	2.1104	2.0223	1.8512	1.7277	1.6449	1.5857	1.5013
10.0	1.6774	1.6223	1.4995	1.4131	1.3584	1.3234	1.2685
15.0	1.1189	1.1011	1.0364	0.9947	0.9740	0.9678	0.9495
20.0	0.5980	0.6068	0.5893	.5842	.5908	.6074	.6203
25.0	.2290	.2467	.2544	.2684	.2884	.3147	.3451
30.0	.0439	.0558	.0677	.0837	.1029	.1262	.1585
35.0	.0031	.0037	.0084	.0161	.0261	.0384	.0614
40.0	.0349	.0270	.0232	.0212	.0208	.0212	.0310
45.0	.0755	.0657	.0582	.0507	.0437	.0366	.0354
50.0	.0914	.0847	.0787	.0712	.0632	.0545	.0479
55.0	.0792	.0772	.0753	.0712	.0660	.0600	.0533
60.0	.0527	.0540	.0556	.0553	.0541	.0523	.0484
65.0	.0281	.0302	.0330	.0350	.0366	.0377	.0371
70.0	.0142	.0152	.0175	.0197	.0220	.0237	.0251
75.0	.0112	.0106	.0117	.0129	.0142	.0147	.0162
80.0	.0141	.0127	.0129	.0128	.0127	.0113	.0118
85.0	.0174	.0161	.0161	.0154	.0143	.0117	.0111
90.0	.0178	.0173	.0179	.0174	.0164	.0139	.0130
95.0	.0152	.0156	.0170	.0175	.0175	.0162	.0162
100.0	.0110	.0121	.0143	.0160	.0174	.0179	.0194
105.0	.0072	.0086	.0113	.0139	.0166	.0184	.0217
110.0	.0049	.0061	.0088	.0119	.0152	.0175	.0219
115.0	.0040	.0048	.0072	.0099	.0130	.0150	.0196
120.0	.0039	.0042	.0059	.0079	.0100	.0113	.0150
125.0	.0038	.0038	.0047	.0057	.0067	.0071	.0093
130.0	.0033	.0032	.0036	.0038	.0041	.0039	.0047
135.0	.0028	.0028	.0031	.0031	.0030	.0027	.0028
140.0	.0026	.0029	.0035	.0039	.0041	.0039	.0043
145.0	.0029	.0035	.0048	.0059	.0069	.0071	.0085
150.0	.0035	.0044	.0064	.0083	.0101	.0105	.0131
155.0	.0043	.0052	.0076	.0099	.0121	.0126	.0161
160.0	.0048	.0053	.0075	.0097	.0117	.0122	.0157
165.0	.0049	.0048	.0063	.0077	.0090	.0093	.0120
170.0	.0045	.0039	.0043	.0047	.0051	.0051	.0067
175.0	.0040	.0030	.0026	.0021	.0017	.0015	.0020
180.0	.0038	.0026	.0019	.0010	.0004	.0000	.0001

TABLE 1. *Angular distributions of neutron elastic scattering for calcium (barns/steradian)*—Continued

Angle	12.700 Mev	12.100 Mev	11.500 Mev	10.900 Mev	10.400 Mev	9.890 Mev	9.410 Mev
deg							
0.	1.5352	1.4533	1.4105	1.3773	1.3298	1.3199	1.3476
5.0	1.4571	1.3852	1.3492	1.3219	1.2816	1.2756	1.3061
10.0	1.2434	1.1979	1.1794	1.1679	1.1470	1.1511	1.1891
15.0	0.9480	0.9357	0.9393	0.9476	0.9521	0.9692	1.0165
20.0	.6382	.6555	.6781	.7039	.7321	.7609	0.8159
25.0	.3726	.4078	.4410	.4768	.5212	.5571	.6152
30.0	.1848	.2238	.2577	.2945	.3445	.3815	.4370
35.0	.0792	.1109	.1378	.1684	.2143	.2470	.2946
40.0	.0382	.0573	.0739	.0947	.1302	.1553	.1916
45.0	.0345	.0416	.0489	.0599	.0832	.0997	.1240
50.0	.0434	.0428	.0439	.0480	.0604	.0695	.0830
55.0	.0491	.0459	.0446	.0448	.0497	.0535	.0588
60.0	.0466	.0441	.0428	.0417	.0426	.0431	.0433
65.0	.0373	.0368	.0362	.0352	.0345	.0334	.0312
70.0	.0259	.0268	.0264	.0256	.0247	.0232	.0205
75.0	.0163	.0171	.0164	.0155	.0148	.0134	.0113
80.0	.0105	.0105	.0091	.0079	.0073	.0063	.0051
85.0	.0089	.0079	.0061	.0046	.0042	.0035	.0032
90.0	.0108	.0096	.0078	.0063	.0062	.0057	.0059
95.0	.0148	.0144	.0131	.0119	.0123	.0117	.0121
100.0	.0193	.0205	.0198	.0189	.0202	.0193	.0196
105.0	.0226	.0255	.0254	.0247	.0269	.0257	.0257
110.0	.0233	.0274	.0276	.0271	.0298	.0285	.0284
115.0	.0209	.0252	.0255	.0252	.0281	.0270	.0269
120.0	.0158	.0194	.0197	.0197	.0223	.0218	.0221
125.0	.0097	.0121	.0124	.0127	.0149	.0151	.0158
130.0	.0047	.0059	.0063	.0069	.0086	.0095	.0106
135.0	.0027	.0032	.0035	.0042	.0057	.0067	.0081
140.0	.0042	.0048	.0049	.0053	.0068	.0076	.0090
145.0	.0083	.0096	.0094	.0093	.0109	.0111	.0122
150.0	.0130	.0152	.0146	.0139	.0158	.0152	.0159
155.0	.0159	.0188	.0179	.0168	.0190	.0178	.0182
160.0	.0156	.0186	.0178	.0168	.0188	.0176	.0179
165.0	.0121	.0146	.0143	.0137	.0154	.0145	.0149
170.0	.0070	.0086	.0089	.0090	.0103	.0100	.0106
175.0	.0025	.0034	.0042	.0048	.0058	.0061	.0069
180.0	.0007	.0013	.0023	.0032	.0040	.0046	.0055

TABLE 1. *Angular distributions of neutron elastic scattering for calcium (barns/steradian)*—Continued

Angle	8.950 Mev.	8.510 Mev.	8.100 Mev.	7.700 Mev.	7.330 Mev.	6.970 Mev.	6.663 Mev.
deg							
0.	1.3531	1.3565	1.3728	1.4119	1.4324	1.4620	1.4826
5.0	1.3142	1.3211	1.3389	1.3795	1.4010	1.4320	1.4533
10.0	1.2039	1.2203	1.2422	1.2867	1.3108	1.3456	1.3687
15.0	1.0400	1.0692	1.0962	1.1457	1.1732	1.2131	1.2385
20.0	0.8472	0.8887	0.9205	0.9741	1.0046	1.0491	1.0766
25.0	.6513	.7014	.7358	.7911	0.8231	0.8704	0.8990
30.0	.4736	.5265	.5608	.6141	.6457	.6930	.7211
35.0	.3276	.3775	.4087	.4565	.4853	.5294	.5554
40.0	.2182	.2603	.2861	.3257	.3500	.3882	.4106
45.0	.1429	.1746	.1939	.2237	.2426	.2731	.2910
50.0	.0946	.1156	.1284	.1485	.1617	.1839	.1972
55.9	.0645	.0763	.0835	.0952	.1034	.1180	.1270
60.0	.0450	.0500	.0531	.0585	.0628	.0713	.0768
65.0	.0308	.0316	.0323	.0338	.0356	.0397	.0427
70.0	.0193	.0183	.0179	.0175	.0180	.0196	.0211
75.0	.0102	.0090	.0085	.0078	.0078	.0084	.0091
80.0	.0045	.0039	.0036	.0034	.0035	.0039	.0043
85.0	.0030	.0032	.0032	.0037	.0038	.0046	.0048
90.0	.0058	.0065	.0065	.0075	.0076	.0087	.0087
95.0	.0118	.0125	.0123	.0135	.0132	.0145	.0142
100.0	.0188	.0193	.0186	.0196	.0190	.0203	.0197
105.0	.0245	.0247	.0236	.0243	.0235	.0247	.0239
110.0	.0270	.0271	.0259	.0264	.0255	.0267	.0261
115.0	.0258	.0260	.0251	.0257	.0251	.0264	.0262
120.0	.0215	.0223	.0220	.0228	.0229	.0245	.0248
125.0	.0161	.0174	.0179	.0191	.0199	.0219	.0229
130.0	.0116	.0132	.0144	.0161	.0174	.0198	.0213
135.0	.0094	.0112	.0126	.0146	.0162	.0189	.0207
140.0	.0100	.0116	.0129	.0150	.0165	.0193	.0212
145.0	.0127	.0137	.0146	.0165	.0177	.0204	.0222
150.0	.0157	.0162	.0164	.0181	.0189	.0216	.0231
155.0	.0174	.0175	.0173	.0187	.0192	.0218	.0232
160.0	.0168	.0169	.0165	.0178	.0182	.0208	.0223
165.0	.0141	.0143	.0140	.0155	.0160	.0188	.0204
170.0	.0103	.0108	.0109	.0125	.0133	.0163	.0183
175.0	.0071	.0079	.0083	.0101	.0111	.0143	.0165
180.0	.0058	.0067	.0073	.0091	.0103	.0135	.0159

Angle	6.300 Mev.	6.000 Mev.	5.700 Mev.	5.430 Mev.	5.160 Mev.	4.910 Mev.	4.670 Mev.
deg							
0.	1.5013	1.5253	1.5377	1.5673	1.5719	1.6092	1.6033
5.0	1.4726	1.4980	1.5109	1.5411	1.5464	1.5837	1.5786
10.0	1.3897	1.4188	1.4335	1.4651	1.4723	1.5096	1.5064
15.0	1.2617	1.2958	1.3128	1.3464	1.3563	1.3935	1.3932
20.0	1.1018	1.1409	1.1604	1.1956	1.2087	1.2453	1.2483
25.0	0.9254	0.9681	0.9894	1.0255	1.0414	1.0770	1.0832
30.0	.7473	.7910	.8134	0.8489	0.8669	0.9006	0.9097
35.0	.5799	.6219	.6439	.6774	.6966	.7276	.7387
40.0	.4321	.4697	.4902	.5202	.5395	.5671	.5792
45.0	.3086	.3398	.3580	.3835	.4019	.4254	.4377
50.0	.2105	.2345	.2497	.2704	.2872	.3065	.3181
55.0	.1363	.1531	.1654	.1813	.1961	.2113	.2218
60.0	.0828	.0935	.1031	.1149	.1276	.1392	.1481
65.0	.0463	.0524	.0597	.0683	.0791	.0877	.0951
70.0	.0231	.0262	.0318	.0383	.0474	.0538	.0598
75.0	.0102	.0117	.0160	.0213	.0290	.0340	.0386
80.0	.0049	.0058	.0093	.0139	.0206	.0247	.0282
85.0	.0050	.0060	.0089	.0132	.0191	.0227	.0252
90.0	.0086	.0098	.0122	.0166	.0218	.0250	.0268
95.0	.0138	.0152	.0173	.0217	.0265	.0295	.0306
100.0	.0190	.0207	.0225	.0271	.0317	.0344	.0352
105.0	.0231	.0249	.0268	.0315	.0361	.0388	.0395
110.0	.0255	.0274	.0295	.0344	.0393	.0422	.0430
115.0	.0260	.0282	.0307	.0359	.0412	.0447	.0459
120.0	.0252	.0277	.0309	.0364	.0423	.0468	.0486
125.0	.0239	.0267	.0305	.0363	.0429	.0489	.0515
130.0	.0229	.0259	.0302	.0363	.0435	.0515	.0551
135.0	.0227	.0256	.0304	.0368	.0446	.0551	.0597
140.0	.0233	.0261	.0311	.0378	.0460	.0595	.0653
145.0	.0242	.0270	.0322	.0390	.0477	.0649	.0719
150.0	.0251	.0278	.0332	.0403	.0494	.0707	.0791
155.0	.0252	.0280	.0337	.0411	.0508	.0767	.0864
160.0	.0244	.0276	.0336	.0414	.0516	.0824	.0934
165.0	.0229	.0265	.0329	.0411	.0519	.0872	.0994
170.0	.0210	.0252	.0319	.0406	.0518	.0910	.1042
175.0	.0196	.0241	.0311	.0401	.0517	.0933	.1072
180.0	.0190	.0237	.0308	.0399	.0516	.0941	.1082

TABLE 1. *Angular distributions of neutron elastic scattering for calcium (barns/steradian)*—Continued

Angle	4.440 Mev	4.230 Mev	4.020 Mev	3.820 Mev	3.640 Mev	3.460 Mev	3.290 Mev
deg							
0.	1.7219	1.6126	1.5996	1.6072	1.3986	1.5570	1.5703
5.0	1.6938	1.5889	1.5765	1.5836	1.3787	1.5360	1.5497
10.0	1.6118	1.5197	1.5093	1.5150	1.3208	1.4746	1.4896
15.0	1.4832	1.4109	1.4034	1.4077	1.2298	1.3776	1.3944
20.0	1.3190	1.2710	1.2672	1.2712	1.1132	1.2522	1.2711
25.0	1.1321	1.1107	1.1109	1.1161	0.9799	1.1074	1.1283
30.0	0.9366	0.9408	0.9449	0.9528	.8394	0.9525	0.9751
35.0	.7455	.7719	.7794	.7907	.7006	.7966	.8206
40.0	.5696	.6126	.6229	.6370	.5708	.6475	.6726
45.0	.4170	.4698	.4818	.4971	.4559	.5115	.5375
50.0	.2923	.3475	.3602	.3749	.3592	.3927	.4195
55.0	.1972	.2477	.2604	.2727	.2824	.2936	.3208
60.0	.1304	.1703	.1823	.1915	.2250	.2148	.2421
65.0	.0884	.1138	.1247	.1312	.1854	.1552	.1822
70.0	.0665	.0754	.0850	.0900	.1607	.1129	.1390
75.0	.0589	.0519	.0600	.0651	.1475	.0850	.1098
80.0	.0600	.0396	.0464	.0524	.1421	.0685	.0917
85.0	.0648	.0352	.0408	.0479	.1409	.0602	.0817
90.0	.0691	.0358	.0404	.0476	.1410	.0574	.0774
95.0	.0702	.0390	.0428	.0491	.1401	.0579	.0768
100.0	.0668	.0432	.0464	.0511	.1366	.0601	.0783
105.0	.0590	.0475	.0504	.0534	.1301	.0634	.0813
110.0	.0481	.0514	.0545	.0567	.1204	.0675	.0855
115.0	.0363	.0552	.0587	.0616	.1083	.0725	.0912
120.0	.0261	.0591	.0636	.0684	.0948	.0791	.0990
125.0	.0201	.0637	.0694	.0769	.0808	.0877	.1096
130.0	.0201	.0693	.0765	.0865	.0677	.0987	.1239
135.0	.0277	.0762	.0852	.0968	.0562	.1126	.1423
140.0	.0430	.0846	.0956	.1078	.0474	.1293	.1647
145.0	.0654	.0942	.1075	.1198	.0417	.1485	.1907
150.0	.0933	.1047	.1206	.1335	.0392	.1696	.2191
155.0	.1243	.1156	.1341	.1491	.0397	.1915	.2484
160.0	.1555	.1261	.1473	.1662	.0425	.2128	.2765
165.0	.1839	.1354	.1592	.1834	.0464	.2319	.3013
170.0	.2066	.1428	.1686	.1982	.0505	.2471	.3207
175.8	.2212	.1475	.1747	.2085	.0534	.2568	.3331
180.0	.2262	.1491	.1768	.2121	.0545	.2602	.3374

Angle	2.970 Mev	2.690 Mev	2.440 Mev	2.210 Mev	2.000 Mev	1.810 Mev	1.630 Mev
deg							
0.	1.4990	1.3767	1.2546	1.1456	1.0433	0.9309	0.8244
5.0	1.4793	1.3603	1.2405	1.1334	1.0327	.9221	.8173
10.0	1.4218	1.3123	1.1991	1.0975	1.0017	.8963	.7963
15.0	1.3311	1.2361	1.1332	1.0403	0.9522	.8552	.7628
20.0	1.2143	1.1369	1.0473	0.9656	.8873	.8013	.7187
25.0	1.0797	1.0211	0.9466	.8779	.8111	.7378	.6663
30.0	0.9364	0.8957	.8374	.7822	.7278	.6881	.6083
35.0	.7927	.7679	.7253	.6838	.6417	.5958	.5476
40.0	.6558	.6440	.6160	.5873	.5569	.5241	.4867
45.0	.5311	.5290	.5138	.4964	.4767	.4554	.4280
50.0	.4219	.4269	.4220	.4142	.4036	.3919	.3731
55.0	.3298	.3396	.3426	.3425	.3391	.3349	.3232
60.0	.2550	.2682	.2764	.2818	.2839	.2851	.2789
65.0	.1962	.2119	.2230	.2321	.2380	.2424	.2403
70.0	.1520	.1694	.1814	.1924	.2005	.2065	.2071
75.0	.1201	.1387	.1500	.1614	.1704	.1767	.1787
80.0	.0988	.1175	.1268	.1376	.1465	.1520	.1544
85.0	.0858	.1036	.1102	.1196	.1276	.1315	.1337
90.0	.0795	.0949	.0986	.1061	.1127	.1148	.1163
95.0	.0782	.0900	.0908	.0962	.1013	.1015	.1019
100.0	.0803	.0879	.0862	.0896	.0933	.0916	.0909
105.0	.0848	.0882	.0846	.0864	.0889	.0856	.0837
110.0	.0908	.0910	.0863	.0870	.0885	.0841	.0811
115.0	.0981	.0968	.0917	.0920	.0930	.0878	.0839
120.0	.1068	.1063	.1016	.1021	.1032	.0974	.0926
125.0	.1176	.1202	.1168	.1181	.1196	.1133	.1078
130.0	.1316	.1391	.1375	.1403	.1426	.1358	.1296
135.0	.1498	.1632	.1640	.1686	.1720	.1645	.1575
140.0	.1727	.1922	.1957	.2025	.2071	.1986	.1905
145.0	.2006	.2252	.2315	.2407	.2466	.2367	.2274
150.0	.2326	.2607	.2698	.2814	.2885	.2770	.2661
155.0	.2671	.2967	.3084	.3223	.3305	.3172	.3044
160.0	.3015	.3309	.3448	.3608	.3699	.3550	.3400
165.0	.3329	.3608	.3765	.3943	.4041	.3877	.3706
170.0	.3580	.3841	.4011	.4202	.4304	.4130	.3941
175.0	.3743	.3988	.4167	.4366	.4471	.4290	.4089
180.0	.3800	.4039	.4220	.4422	.4529	.4345	.4139

TABLE 1. *Angular distribution of neutron elastic scattering for calcium (barns/steradian)*—Continued

Angle	1.480 Mev	1.340 Mev	1.210 Mev	1.096 Mev	0.991 Mev	0.853 Mev	0.734 Mev
deg							
0.	0.4400	0.6742	0.3484	0.3193	0.2848	0.4682	0.4299
5.0	.4365	.6691	.3459	.3172	.2831	.4656	.4277
10.0	.4263	.6541	.3388	.3111	.2780	.4577	.4211
15.0	.4097	.6301	.3273	.3013	.2697	.4450	.4104
20.0	.3879	.5982	.3121	.2883	.2586	.4280	.3960
25.0	.3619	.5602	.2938	.2726	.2453	.4074	.3786
30.0	.3330	.5178	.2733	.2550	.2302	.3842	.3588
35.0	.3025	.4730	.2515	.2360	.2140	.3590	.3372
40.0	.2717	.4275	.2292	.2165	.1972	.3328	.3146
45.0	.2416	.3829	.2071	.1969	.1802	.3063	.2915
50.0	.2131	.3404	.1857	.1778	.1636	.2801	.2685
55.0	.1868	.3007	.1655	.1596	.1477	.2548	.2460
60.0	.1630	.2646	.1467	.1424	.1325	.2306	.2244
65.0	.1418	.2319	.1295	.1264	.1184	.2078	.2038
70.0	.1230	.2028	.1139	.1117	.1053	.1865	.1844
75.0	.1066	.1769	.0998	.0983	.0932	.1669	.1664
80.0	.0922	.1540	.0871	.0861	.0822	.1489	.1498
85.0	.0797	.1338	.0758	.0752	.0723	.1326	.1348
90.0	.0689	.1163	.0659	.0656	.0636	.1182	.1215
95.0	.0600	.1016	.0576	.0575	.0562	.1060	.1100

TABLE 1.—*Angular distribution of neutron elastic scattering for calcium (barns/steradian)*—Continued

Angle	1.480 Mev	1.340 Mev	1.210 Mev	1.096 Mev	0.991 Mev	0.853 Mev	0.734 Mev
deg							
100.0	.0530	.0902	.0511	.0511	.0503	.0861	.1007
105.0	.0484	.0824	.0465	.0465	.0461	.0889	.0937
110.0	.0464	.0790	.0443	.0441	.0437	.0847	.0894
115.0	.0476	.0805	.0447	.0441	.0435	.0839	.0878
120.0	.0521	.0875	.0480	.0467	.0456	.0866	.0893
125.0	.0603	.1003	.0542	.0519	.0499	.0930	.0937
130.0	.0720	.1188	.0634	.0598	.0565	.1028	.1010
135.0	.0872	.1426	.0752	.0699	.0652	.1157	.1108
140.0	.1051	.1709	.0893	.0820	.0755	.1312	.1227
145.0	.1250	.2023	.1049	.0955	.0869	.1484	.1360
150.0	.1459	.2352	.1212	.1095	.0989	.1665	.1501
155.0	.1666	.2677	.1373	.1234	.1108	.1844	.1640
160.0	.1858	.2978	.1523	.1363	.1218	.2010	.1768
165.0	.2022	.3236	.1651	.1473	.1312	.2152	.1879
170.0	.2148	.3435	.1749	.1557	.1384	.2261	.1963
175.0	.2228	.3560	.1810	.1610	.1429	.2329	.2016
180.0	.2255	.3602	.1831	.1628	.1445	.2352	.2034

TABLE 2. *Legendre coefficients for calcium elastic scattering*

Energy—Mev	18.000	17.100	16.300	15.500	14.750	14.000	13.300
Total elastic—barns	0.836	0.826	0.806	0.797	0.800	0.804	0.827
$S_l(E)$, l= 0	1.00000	1.00000	1.00000	1.00000	1.00000	1.00000	1.00000
1	0.80315	0.79852	0.77512	0.75673	0.74259	0.74200	0.72305
2	.63456	.63283	.61087	.59713	.58931	.59324	.58335
3	.52042	.52075	.50234	.49179	.48678	.49052	.48014
4	.44965	.44827	.43098	.41843	.40920	.40525	.38564
5	.38692	.38273	.36377	.34726	.33268	.32239	.29412
6	.33349	.32659	.30864	.29195	.27627	.26353	.23572
7	.27457	.26459	.24661	.22811	.20948	.19201	.16411
8	.19745	.18289	.16280	.14236	.12222	.10318	.07932
9	.11379	.10103	.08647	.07360	.06212	.05073	.04016
10	.04970	.04153	.03233	.02535	.02005	.01572	.01149
11	.01833	.01441	.01021	.00735	.00540	.00401	.00267
12	.00600	.00448	.00294	.00197	.00136	.00096	.00059
13	.00176	.00125	.00076	.00048	.00031	.00021	.00012
14	.00048	.00033	.00019	.00011	.00007	.00004	.00002
15	.00012	.00008	.00004	.00002	.00001	.00001	

Energy—Mev	12.700	12.100	11.500	10.900	10.400	9.890	9.410
Total elastic—barns	0.841	0.882	0.912	0.951	1.030	1.082	1.177
$S_l(E)$, l= 0	1.00000	1.00000	1.00000	1.00000	1.00000	1.00000	1.00000
1	0.72659	0.71210	0.72014	0.72907	0.72052	0.72939	0.73597
2	.58770	.57698	.58101	.58442	.57153	.57326	.57503
3	.47996	.46317	.45735	.44935	.42450	.41510	.40540
4	.37632	.34809	.33140	.31266	.27692	.25958	.24144
5	.27959	.24550	.22536	.20430	.16755	.15023	.13010
6	.22017	.18950	.16944	.14854	.11804	.10130	.08231
7	.14672	.11953	.10163	.08462	.06413	.05288	.04149
8	.06418	.04400	.03236	.02305	.01255	.00863	.00521
9	.03164	.02328	.01665	.01139	.00748	.00496	.00330
10	.00883	.00607	.00426	.00285	.00179	.00117	.00076
11	.00197	.00123	.00084	.00054	.00031	.00020	.00012
12	.00042	.00024	.00016	.00010	.00005	.00003	.00002
13	.00008	.00004	.00003	.00002			
14	.00002						

Energy—Mev	8.950	8.510	8.100	7.700	7.330	6.970	6.663
Total elastic—barns	1.238	1.341	1.407	1.523	1.591	1.709	1.777
$S_l(E)$, l= 0	1.00000	1.00000	1.00000	1.00000	1.00000	1.00000	1.00000
1	0.74212	0.74199	0.74508	0.74309	0.74353	0.73635	0.73453
2	.57477	.56609	.56447	.55856	.55588	.54614	.54279
3	.39604	.37741	.36886	.35637	.34828	.33352	.32556
4	.22696	.20325	.19213	.17775	.16886	.15474	.14743
5	.11689	.09579	.08670	.07400	.06757	.05690	.05233
6	.06991	.05333	.04520	.03526	.02998	.02295	.01961
7	.03407	.02518	.02073	.01597	.01319	.01015	.00839
8	.00360	.00168	.00119	.00055	.00043	.00013	.00013
9	.00215	.00126	.00081	.00050	.00033	.00019	.00012
10	.00049	.00027	.00017	.00011	.00007	.00004	.00002
11	.00008	.00004	.00003	.00002	.00001		
12	.00001						

Energy—Mev	6.300	6.000	5.700	5.430	5.160	4.910	4.670
Total elastic—barns	1.844	1.965	2.057	2.196	2.313	2.472	2.538
$S_l(E)$, l= 0	1.00000	1.00000	1.00000	1.00000	1.00000	1.00000	1.00000
1	0.73165	0.72296	0.70672	0.68561	0.65982	0.62793	0.61459
2	.53906	.52817	.51546	.49904	.48011	.47289	.46532
3	.31721	.30341	.28995	.27561	.25893	.24041	.22903
4	.14042	.12812	.11992	.11103	.10245	.09839	.09343
5	.04818	.03950	.03571	.03080	.02742	.02337	.02113
6	.01680	.01218	.01029	.00798	.00669	.00581	.00506
7	.00692	.00491	.00397	.00300	.00240	.00181	.00147
8	.00014	.00003	.00004	.00002	.00003	.00022	.00023
9	.00008	.00004	.00003	.00002	.00001		
10	.00002	.00001					

TABLE 2. *Legendre coefficients for calcium elastic scattering*—Continued

Energy Mev	4.440	4.230	4.020	3.820	3.640	3.460	3.290
Total elastic barns	2.669	2.761	2.858	2.965	3.043	3.149	3.481
$S_l(E), l=0$	1.00000	1.00000	1.00000	1.00000	1.00000	1.00000	1.00000
1	0.59352	0.57163	0.54777	0.52606	0.50422	0.47943	0.42278
2	.45321	.44185	.43012	.42050	.26083	.39623	.36924
3	.21764	.20350	.18836	.17691	.16300	.14962	.12522
4	.14034	.08320	.07840	.07496	.07244	.06756	.06291
5	.01825	.01618	.01416	.01204	.01051	.00885	.00701
6	.00408	.00359	.00330	.00279	.00291	.00241	.00238
7	.00109	.00087	.00069	.00050	.00040	.00030	.00022
8	.00024	.00026	.00037	.00247	.00037	.00031	

Energy Mev	2.970	2.690	2.440	2.210	2.000	1.810	1.630
Total elastic barns	3.502	3.551	3.476	3.432	3.371	3.228	3.065
$S_l(E), l=0$	1.00000	1.00000	1.00000	1.00000	1.00000	1.00000	1.00000
1	0.39586	0.36179	0.34086	0.31364	0.28852	0.27864	0.26563
2	.35560	.33340	.31893	.30155	.28452	.26741	.25148
3	.10885	.08494	.06471	.04677	.03169	.01740	.00559
4	.05815	.05179	.04688	.04314	.03973	.03473	.03123
5	.00512	.00366	.00261	.00177	.00119	.00078	.00049
6	.00537	.00135	.00109	.00084	.00065	.00051	
7	.00012	.00007	.00005				

Energy Mev	1.480	1.340	1.210	1.096	0.991	0.853	0.734
Total elastic barns	1.727	2.779	1.500	1.426	1.322	2.303	2.224
$S_l(E), l=0$	1.00000	1.00000	1.00000	1.00000	1.00000	1.00000	1.00000
1	0.26421	0.25235	0.25450	0.25701	0.25074	0.23850	0.23522
2	.23576	.22312	.20742	.19271	.17951	.15989	.13935
3	−.00221	−.00704	−.01040	−.01179	−.01216	−.01140	−.00941
4	.02695	.02480	.02103	.01784	.01589	.01330	.01028
5	.00031	.00020	.00012	.00008			

5. Conclusions

Reasonably satisfactory average cross section predictions for calcium at neutron energies below 18 Mev can be made with the nuclear optical model using compound elastic scattering cross sections as calculated from the optical model in the absence of inelastic scattering, and using a Hauser-Feshbach calculation if inelastic scattering is present. In order to achieve the goal of calculation of any neutron cross section as required, Hauser-Feshbach and direct interaction inelastic scattering codes for inelastic scattering, and nuclear reaction codes will be required, for which the present type of calculation provides input data.

More experimental data in the region from 6 to 14 Mev is needed. Also the difference between the Seagrave et al. and the Lane et al. data at low energies needs to be resolved.

6. References

Amster, H. J., Leshan, E. J., and Walt, M., Computer techniques, Ch. IV. I., Fast Neutron Physics, Pt I, J. B. Marion and J. L. Fowler, Ed. (1960).

Biedenharn, L. C., U. S. Atomic Energy Commission Report ORNL–1501 (1953).

Biedenharn, L. C., Blatt, J. M., and Rose, M. E., Rev. Mod. Phys. **24,** 249 (1952).

Bjorklund, F., and Fernbach, S., Phys. Rev. **109,** 1295 (1958).

Blatt, J. M., and Biedenharn, L. C., Rev. Mod. Phys. **24,** 258 (1952).

Blatt, J. M., and Weisskopf, V. F., Theoretical Nuclear Physics, p. 333, Wiley (New York) (1952).

Bohm, D., Quantum Theory, p. 344, Prentice-Hall (1951).

Cross, W. G., and Jarvis, R. G., Nuclear Physics **15,** 155 (1960).

Edmonds, A. R., Angular Momentum in Quantum Mechanics, Princeton Univ. Press, Princeton, N. J., p. 63 (1957).

Feshbach, H., The complex potential model, Ch. VI. of Nuclear Spectroscopy, Part B, Fay Ajzenberg-Selove, Ed., Academic Press (New York) (1960).

Feshbach, H., Porter, C. E., and Weisskopf, V. F., Phys. Rev. **96,** 448 (1954).

Flerov, N. N., and Talyzin, V. M., Atomnaya Energiya **1,** 155 (1956).

Gursky, M. L., and Stewart, Leona, Bull. Am. Phys. Soc. II, **6,** 367 (1961).

Hauser, W., and Feshbach, H., Phys. Rev. **87,** 366 (1952).

Howerton, R. J., U. S. A.E.C. Report (UCRL-5573) (1961).

Huber, P., and Meyer, K. P., Proc. Intern. Symposium on Polarization Phenomena of Nucleons, p. 436, Berkhaüser Verlag (Basel and Stuttgart) (1961).

Lane, R. O., Langsdorf, A. S. Jr., Monahan, J. B., and Elwyn, A. J., private communication (1960). (See Howerton, 1961.)

Lepore, J., Phys. Rev. **79,** 137 (1950).

Morse, P. M., and Feshbach, H., Methods of Theoretical Physics, Mc-Graw Hill, New York, vol. 2, p. 1325 (1953).

Perey, F. G. J., and Buck, B., Neutron Physics Division Progress Report, ORNL–3193 (1961).

Seagrave, J. D., Cranberg, L., and Simmons, J. E., Private communication (1958). (See Howerton, 1961.)

Troubetzkoy, E. S., Kalos, M. H., Lustig, H., Ray, J. H., and Trupin, B. H., NDA Report 2133–4 (NDL–TR–5), Nuclear Development Corporation of America, White Plains, N.Y. (1961).

Vincent, L. D., Morgan, I. L., Prud 'homme, J. T., WADD–TR–60–217 (1960).

Whittaker, E. T., and Watson, G. N., Modern Analysis, p. 331, Cambridge (1958).

Wolfenstein, L., Phys. Rev. **82,** 690 (1951).

Zurmühl, R., Praktische Mathematik für Ingenieure und Physiker, p. 412, Springer-Verlag, (Berlin, Gottingen, Heidelberg) (1961).

(Paper 66A5–174)

JOURNAL OF RESEARCH of the National Bureau of Standards—A. Physics and Chemistry
Vol. 66A, No. 5, September–October 1962

Pyrolysis of Some Polyvinyl Polymers at Temperatures Up to 1,200 °C

Sidney Straus and Samuel L. Madorsky

(May 10, 1962)

A study was made of the thermal behavior in a vacuum of polystyrene, polytetrafluoroethylene, poly(α-methylstyrene), polypropylene, polyisobutylene, and poly(methyl methacrylate), when pyrolized at 500, 800, and 1,200 °C. The volatile products of degradation were collected and fractionated, and the fractions analyzed by mass-spectrometric and microcryoscopic methods. Generally, the results from 500 °C pyrolysis resemble those obtained previously from the same polymer at lower temperatures. The results at 800° and 1,200° indicate a much greater fragmentation of the pyrolysis products than at lower temperatures. Thus, for example, at 1,200° polystyrene yields less monomer but considerable greater amounts of C_2H_2, C_2H_4, C_3H_4, and C_6H_6 than at lower temperatures. Similarly, poly(α-methylstyrene) yields 100 percent monomer below 500 °C, but at 800 and 1,200 °C the yields are 88 percent and 34 percent, respectively. Also at the higher temperatures, pronounced amounts of H_2, CH_4, C_2H_2, C_2H_4, C_3H_4, C_3H_6, C_4H_4, C_6H_6, C_4H_8, and C_5H_8 are formed.

1. Introduction

While the literature contains a great deal of information on the behavior of polymers at temperatures up to about 500 °C, little is known about their behavior above this temperature. Natural crepe rubber was pyrolyzed up to 700 °C [1],[1] smoked crepe up to 650 °C [2], and polyisoprene up to 900 °C [3]. In all these experiments it was found that a higher temperature of pyrolysis produces a greater yield of isoprene in the degradation products [3, 4].

In the past few years a number of applications have been made of organic polymers as protective coatings for bodies subjected to very high temperatures. They have been used, for example, as the covering of the nose cones of missiles and satellites which develop considerable amounts of heat through friction with air at high velocities, and as the lining for the inner surface of nozzles that come in contact with the hot exhaust gases in jet propulsion. These applications have stimulated research on the thermal stability of polymers at high temperatures. In these investigations the heating of the materials has often been accomplished by means of an electric arc or by a stream of hot gas. However, in most of these experiments the polymeric materials were not in the pure state but contained extraneous materials such as carbon, glass, asbestos, etc. The products of degradation, therefore, consisted of a complex mixture of molecular fragments coming not only from the polymer but from the extraneous material as well. The gases from the arc or from the hot gas stream were an additional source of contamination of the products. This made it very difficult either to anlyze the products of degradation or to interpret the chemical reactions involved.

Studies were recently made by the present authors on the pyrolysis of polymers in a vacuum and, in some cases, in a helium atmosphere in the temperature range of 500 to 1,200 °C. The polymers thus investigated were: polystyrene up to 850 °C, and polyacrylonitrile, poly(vinylidene fluoride), and polytrivinylbenzene up to 800 °C [5]; polymethylene, poly(vinylidene fluoride), and polytrivinylbenzene up to 1,200 °C [6]; and silicone, phenolic, epoxy, and ester resins up to 1,200 °C [7]. The present investigation extends the program to cover a few simple vinyl polymers at temperatures ranging from 400 to 1,200 °C. These polymers include polystyrene, polytetrafluoroethylene, poly(α-methylstyrene), polypropylene, polyisobutylene, and poly (methyl methacrylate).

2. Materials Used

The materials used had the following characteristics:

(a) *Polystyrene.* Thermally prepared. Molecular weight 230,000, as determined by the osmotic pressure method.

(b) *Polytetrafluoroethylene.* Teflon tape 0.07 mm thick. Molecular weight not known, but estimated to be very high.

(c) *Poly(α-methylstyrene).* Flaky material obtained from the Dow Chemical Company. Prepared by low-temperature polymerization. Molecular weight 350,000, as determined by light scattering.

(d) *Polypropylene.* Fine white powder obtained from B. F. Goodrich Company. Prepared by the Ziegler method. Molecular weight between 50,000 and 100,000.

(e) *Polyisobutylene.* Pure grade white gum. Currently used as a National Bureau of Standards standard material for viscosity measurements. Molecular weight 1,560,000, as determined by the light-scattering method.

(f) *Poly(methyl methacrylate).* Prepared from the monomer at room temperature without the use of catalysts. Molecular weight 5,100,000, as determined by light scattering.

[1] Figures in brackets indicate the literature references at the end of this paper.

3. Apparatus and Experimental Procedure

The apparatus used in the pyrolysis studies was the same as that used in the pyrolysis of polytrivinylbenzene and other polymers [6, 7], except that the fused quartz tube holding the sample tube was replaced with a platinum tube. Samples weighing 15 to 30 mg were heated in a vacuum by quickly moving a preheated furnace into position surrounding the sample for pyrolysis. For temperatures of 500 °C or lower a 5-min period was used to heat up the sample from room temperature to the temperature of pyrolysis, followed by a 30-min period at the pyrolysis temperature. Fluctuation of the final temperature was ±2 °C. For higher temperatures a 2-min preheating period was followed by a 5-min heating period at the required temperature, and fluctuation of the operating temperature was ±5 °C. The residues were weighed, and the volatile products were collected and fractionated. The following volatilized fractions were obtained: (a) A waxlike fraction, designated as V_{pyr}, volatile at the temperature of pyrolysis, but not at room temperature, and consisting of large molecular fragments deposited in the apparatus just beyond the hot zone; (b) a light fraction, V_{25}, volatile at room temperature, collected in a liquid-nitrogen-cooled trap; and (c) a gaseous fraction, V_{-190}, not condensable at the temperature of liquid nitrogen. In some cases a fraction, V_{-80}, volatile at the temperature of dry ice, was also collected. Analyses of fractions V_{25}, V_{-80}, and V_{-190} were made by means of a mass spectrometer.

4. Experimental Detail

4.1. Polystyrene

It was shown in an earlier study [5] on pyrolysis of polystyrene at 362 and 850 °C in a vacuum, and in helium at atmospheric pressure, that a higher temperature, a higher pressure, or both, cause a greater fragmentation of the volatile products. This study has now been extended to temperatures up to 1,200 °C. The volatile products were collected and fractionated in the usual manner, and the more volatile fractions were analyzed in the mass spectrometer.

Distribution of fractions from pyrolysis in a vacuum at 400, 500, 800, and 1,200 °C is shown in table 1, and from pyrolysis at similar temperatures in helium, in table 2. Results of analysis of the volatile products from pyrolysis in a vacuum are shown in table 3 and those from pyrolysis in helium are shown in table 4. As seen from tables 3 and 4, the yield of monomer C_8H_8 from vacuum pyrolysis decreases with increase of temperature, while in pyrolysis in helium the decrease is so drastic that at 1,200 °C only 0.6 percent of monomer is produced.

There is some discrepancy between the results shown in tables 1, 2, 3, and 4 of this paper and those obtained previously at 362 and 850 °C [5, 8]. However, this may be due to the fact that in this work the time of collecting fraction V_{25} by means of liquid nitrogen was 3 hr instead of the 1 hr in the previous work. The longer period of collection of V_{25} was used in all the experiments described in this paper.

TABLE 1. *Pyrolysis of polystyrene in a vacuum*

Experiment	Weight of sample	Temperature	Volatilization	Fractions based on total volatilized		
				V_{pyr}	V_{25}	V_{-190}
	mg	°C	%	%	%	%
1	14.85	400	98.8	46.9	53.1	
2	14.25	400	99.0	43.3	56.7	
3	20.4	500	100.0	36.5	63.5	
4	19.9	500	100.0	38.6	61.4	
5	17.9	800	99.7	28.2	71.8	
6	16.7	800	100.0	22.8	77.2	
7	19.5	1200	98.0	34.4	65.0	0.6
8	13.4	1200	98.1	33.6	66.0	.4

TABLE 2. *Pyrolysis of polystyrene in helium*

Experiment	Weight of sample	Temperature	Volatilization	Products based on total volatilized	
				V_{pyr}[a]	V_{25}
	mg	°C	%	%	%
9	19.6	500	100.0	35.2	64.8
10	15.7	500	100.0	28.4	71.6
11	18.7	800	98.5	40.0	60.0
12	16.6	800	99.1	39.8	60.2
13	16.1	1200	95.3	74.6	25.4

[a] Fraction V_{-190} could not be separated from the helium. In vacuum pyrolysis V_{-190} appeared in small amounts only at 1,200 °C (table 1). Here fraction V_{-190} is included in V_{pyr}.

TABLE 3. *Analysis of volatile products from pyrolysis of polystyrene in a vacuum*

Component[a]	At 400 °C		At 500 °C		At 800 °C		At 1,200 °C	
	No. 1	No. 2	No. 3	No. 4	No. 5	No. 6	No. 7	No. 8
	%	%	%	%	%	%	%	%
H_2							0.1	0.1
C_2H_6							.1	
C_2H_2							5.6	4.2
C_2H_4						1.6	3.6	5.0
C_3H_4						0.4	1.5	3.0
C_4H_6	2.0	2.3	1.5	0.5	0.8	1.6	6.2	7.1
C_7H_8	4.0	3.6	1.1	3.4	1.8	3.9	0.6	1.5
C_8H_8	46.5	50.0	56.4	51.4	47.4	47.5	41.6	41.1
C_8H_{10}	0.2	0.3						
C_9H_{10}	.4	.5	4.5	6.1	21.8	22.2	6.3	4.4
V_{pyr}	46.9	43.3	36.5	38.6	28.2	22.8	34.4	33.6
Total	100.0	100.0	100.0	100.0	100.0	100.0	100.0	100.0

[a] Components are in weight percent of total volatiles.

TABLE 4. *Analysis of volatile products from pyrolysis of polystyrene in helium*

Component[a]	At 500 °C		At 800 °C		At 1,200 °C
	No. 9	No. 10	No. 11	No. 12	No. 13
	%	%	%	%	%
C_2H_2	0.1				0.6
C_2H_4			8.5	5.8	2.6
C_2H_6				0.4	0.2
C_3H_4			0.2		
C_4H_{10}		3.5			
C_5H_{10}					
C_6H_6	.7	1.4	16.2	15.5	12.5
C_7H_8	5.5	12.5	7.7	7.2	1.3
C_7H_{11}	0.9		0.6		
C_8H_8	52.7	49.1	8.8	12.5	0.6
C_8H_{10}				0.8	
C_8H_{11}	0.4				
C_9 and up	4.5	5.1	18.0	18.0	7.6
V_{pyr}	35.2	28.4	40.0	39.8	74.6
Total	100.0	100.0	100.0	100.0	100.0

[a] Components are in weight percent of total volatiles.

4.2. Polytetrafluoroethylene

It was shown in our previous work [9] that polytetrafluoroethylene (Teflon), when pyrolyzed in a vacuum at temperatures up to 538 °C, yields about 95 percent monomer. In the present work the effect of higher temperatures of pyrolysis on the nature and relative amounts of the volatiles is revealed. Distribution of fractions and analysis of volatile products are shown in tables 5 and 6. The HF in the products at 1,200 °C was calculated from the mass spectrometer analysis of SiF_4, which forms in the reaction of HF with glass in the presence of even a trace of H_2O. In contrast with low-temperature pyrolysis, the products from pyrolysis at higher temperatures contain, in addition to monomer, considerable amounts of larger fragments collected as fraction V_{pyr}.

TABLE 5. *Pyrolysis of polytetrafluoroethylene in a vacuum*

Experiment	Weight of sample	Temperature	Volatilization	Fractions based on total volatilized [a]	
				V_{pyr}	V_{25}
	mg	*°C*	*%*	*%*	*%*
1	24.7	500	17.2	0	100
2	20.2	500	16.1	0	100
3	14.1	800	99.7	0	100
4	8.6	800	100	1.8	98.2
5	10.9	1200	100	11.8	88.2
6	10.7	1200	100	15.9	84.1

[a] Fraction V_{-190} appeared in trace amounts.

TABLE 6. *Analysis of volatile products from pyrolysis of polytetrafluoroethylene in a vacuum*

Component [a]	At 500 °C		At 800 °C		At 1,200 °C	
	No. 1	No. 2	No. 3	No. 4	No. 5	No. 6
	%	*%*	*%*	*%*	*%*	*%*
HF	0	0	0	0	0.2	0.5
CF_4	1.5	1.2	1.6	1.8	1.7	2.6
C_2F_4	94.8	95.1	92.5	89.9	81.0	75.2
C_3F_6	3.7	3.7	5.9	6.5	5.3	5.8
V_{pyr}	0	0	0	1.8	11.8	15.9
Total	100.0	100.0	100.0	100.0	100.0	100.0

[a] Components are in weight percent of total volatiles.

4.3. Poly(α-methylstyrene)

When heated in a vacuum at temperatures below 400 °C, poly(α-methylstyrene) decomposes almost completely into monomer [10]. The effect of a higher temperature on the distribution of fractions in the pyrolysis of this polymer is shown in table 7. Considerable amounts of fractions V_{pyr} and V_{-190} are produced at the expense of fraction V_{25}. This effect is even more clearly indicated in table 8, where analysis of the volatile fractions from pyrolysis of the polymer is shown.

4.4. Polypropylene and Polyisobutylene

Pyrolysis of these two polymers in a vacuum has been studied previously at temperatures up to about 400 °C. For polypropylene the yield of monomer-size molecules, fraction V_{25}, is about 14 percent [11] and for polyisobutylene about 32 percent [4]. At higher temperatures fractions V_{25} are produced in larger amounts, as shown in tables 9 and 10.

TABLE 7. *Pyrolysis of poly(α-methylstyrene) in a vacuum*

Experiment	Weight of sample	Temperature	Amount of volatilization	Fractions based on total volatilized		
				V_{pyr}	V_{25}	V_{-190}
	mg	*°C*	*%*	*%*	*%*	*%*
1	10.2	500	99.0	0	100	0
2	11.3	500	99.4	0	100	0
3	8.0	800	100.0	11.2	88.7	0.1
4	10.1	800	100.0	5.4	94.3	.3
5	7.9	1200	98.7	34.3	54.2	11.5
6	8.2	1200	99.4	32.6	61.1	6.3

TABLE 8. *Analysis of volatile products from pyrolysis of poly (α-methylstyrene) in a vacuum*

Component [a]	At 500 °C		At 800 °C		At 1,200 °C	
	No. 1	No. 2	No. 3	No. 4	No. 5	No. 6
	%	*%*	*%*	*%*	*%*	*%*
H_2			0.1	0.1	1.7	1.3
CH_4			.3	.3	5.6	3.1
C_2H_2					0.8	0.7
C_2H_4			.5	.1	3.8	3.2
C_3H_4			.8	.3	1.0	1.8
C_3H_6			.8	.2	0.7	0.4
C_4H_6					.5	1.9
C_6H_6			2.0	1.1	9.3	13.3
C_7H_8			0.4	0.3	6.1	3.6
C_8H_8					2.6	4.2
C_9H_{10}	100.0	100.0	83.9	92.2	33.6	33.9
V_{pyr}	0	0	11.2	5.4	34.3	32.6
Total	100.0	100.0	100.0	100.0	100.0	100.0

[a] Components are in weight percent of total volatiles.

TABLE 9. *Pyrolysis of polypropylene in a vacuum*

Experiment	Weight of sample	Temperature	Volatilization	Fractions based on total volatilized		
				V_{pyr}	V_{25} [a]	V_{-190}
	mg	*°C*	*%*	*%*	*%*	*%*
1	10.0	400	76.5	76.7	23.3	Trace
2	10.5	400	82.4	79.2	20.8	Trace
3	11.0	500	99.6	82.4	17.6	Trace
4	9.6	800	100.0	29.6	70.3	0.1
5	9.4	1200	98.9	22.4	75.8	1.8
6	40.8	1200	98.9	31.7	53.7	14.6

[a] Includes V_{-85} fraction.

TABLE 10. *Pyrolysis of polyisobutylene in a vacuum*

Experiment	Weight of sample	Temperature	Volatilization	Fractions based on total volatilized		
				V_{pyr}	V_{25} [a]	V_{-190}
	mg	*°C*	*%*	*%*	*%*	*%*
1	15.9	400	99.3	53.3	46.7	0
2	14.1	400	98.6	57.5	42.5	0
3	17.0	500	99.4	51.1	47.8	1.1
4	15.8	500	99.4	52.1	46.9	1.0
5	13.8	800	99.6	3.6	94.8	1.6
6	12.9	800	99.2	3.1	94.5	2.4
7	14.1	1200	98.6	14.7	66.8	18.5
8	14.0	1200	97.5	7.6	73.3	19.1

[a] Includes V_{-80} fraction.

Analyses of the volatile fraction from pyrolysis of these two polymers are shown in tables 11 and 12. As compared with pyrolysis at temperatures below 500 °C, [4, 8, 11] the yields of monomers, C_3H_6 and C_4H_8, are much higher at the higher temperatures. However, in the case of polyisobutylene at 1,200 °C the yield of C_4H_8 is very low and the yields of fragments of lower molecular weight, particularly of H_2, CH_4, and C_2H_4, are very high.

TABLE 11. *Analysis of volatile products from pyrolysis of polypropylene in a vacuum*

Component [a]	At 400 °C		At 500 °C	At 800 °C	At 1,200 °C	
	No. 1	No. 2	No. 3	No. 4	No. 5	No. 6
	%	%	%	%	%	%
H_2				0.1	0.1	0.4
CH_4	0.1	0.1		.4	2.6	9.6
C_2H_2	.1	.1		.3	6.3	4.3
C_2H_4	.4	.3	0.4	6.0	13.1	19.0
C_2H_6	.3	.3	.3	0.7	1.0	0.9
C_3H_4	.6	.4	.3	3.4	8.5	6.5
C_3H_6	.6	.6	.4	17.9	18.4	12.6
C_3H_8	.5	.5	.6	2.3	1.9	0.6
C_4H_4				0.7	2.3	2.4
C_4H_6				3.0	5.1	4.1
C_4H_8	2.5	1.7	.6	12.4	8.1	2.9
C_4H_{10}	1.8	1.3	.7	1.3	0.5	
C_5H_6				0.5	.8	1.0
C_5H_8	0.8	0.6	.6	3.0	2.1	0.8
C_5H_{10}	3.3	3.8	2.0	10.2	4.1	.3
C_5H_{12}	3.1	2.2	3.0	1.9		
C_6H_6					1.6	2.9
C_6H_{10}	0.7	0.5	0.7	1.7	0.7	
C_6H_{12}	4.0	3.7	3.0	4.6	.4	
C_6H_{14}	0.2	1.4	1.9			
C_8H_{16}	2.2	1.8	1.0			
C_8H_{18}	2.1	1.5	1.4			
$C_{10}H_{20}$			0.7			
V_{pyr}	76.7	79.2	82.4	29.6	22.4	31.7
Total	100.0	100.0	100.0	100.0	100.0	100.0

[a] Components are in weight percent of total volatiles.

TABLE 12. *Analysis of volatile products from pyrolysis of polyisobutylene in a vacuum*

Component [a]	At 400 °C		At 500 °C		At 800 °C		At 1,200 °C	
	No. 1	No. 2	No. 3	No. 4	No. 5	No. 6	No. 7	No. 8
	%	%	%	%	%	%	%	%
H_2							2.7	1.6
CH_4					1.2		17.6	10.1
C_2H_2					0.8	1.1	6.8	7.3
C_2H_4			0.9	0.6	2.7	5.0	9.6	13.6
C_2H_6							1.6	1.2
C_3H_4	0.5		1.1	1.6	3.0	5.4	14.9	16.5
C_3H_6							0.9	1.0
C_3H_8			0.7	1.3			4.8	4.4
C_4H_4					2.1	1.3	4.5	4.2
C_4H_6						0.7	4.5	5.9
C_4H_8	35.6	31.5	38.0	34.9	72.7	65.3	10.6	15.3
C_4H_{10}	0.7	0.7						
C_5H_6						0.5	1.0	1.9
C_5H_8			0.7				0.7	2.4
C_5H_{10}					5.7	1.7		1.1
C_6 and up	9.9	10.3	7.4	9.5	8.2	15.9	5.1	5.9
V_{pyr}	53.3	57.5	51.2	52.1	3.6	3.1	14.7	7.6
Total	100.0	100.0	100.0	100.0	100.0	100.0	100.0	100.0

[a] Components are in weight percent of total volatiles.

4.5. Poly(methyl methacrylate)

Poly(methyl methacrylate) decomposes primarily into monomer on heating in a vacuum at temperatures up to about 350 °C [10]. However, when the temperature is raised to 1,200 °C considerable amounts of other fragments, both larger and smaller than the monomer, appear among the volatiles. Table 13 shows the distribution of volatile fractions for 500, 800, and 1,200° C pyrolysis. The appearance of preponderant amounts of V_{-190} at 1,200 °C is particularly notable and is mainly due to the formation of CO, CO_2, H_2, CH_4, C_2H_2, and C_2H_4, as indicated in table 14. It was found that fractions V_{25} and V_{-190} from pyrolysis at 800 and 1,200 °C, if allowed to stand for more than a day, tended to repolymerize and thus give misleading results. All the analyses of these two fractions were therefore made on the same day that they were produced and collected.

TABLE 13. *Pyrolysis of poly(methyl methacrylate) in a vacuum*

Experiment	Weight of sample	Temperature	Volatilization	Fractions based on total volatilized		
				V_{pyr}	V_{25}	V_{-190}
	mg	°C	%	%	%	%
1	10.3	500	100	3.6	96.4	0
2	9.9	500	100	2.3	97.7	0
3	8.5	800	100	11.2	88.7	0.1
4	11.3	800	100	8.8	91.1	.1
5	9.8	1200	100	5.0	29.4	65.6
6	9.8	1200	100	8.2	26.2	65.6

TABLE 14. *Analysis of volatile products from pyrolysis of poly(methyl methacrylate) in a vacuum*

Component [a]	At 500 °C		At 800 °C		At 1,200 °C	
	No.	No. 2	No. 3	No. 4	No. 5	No. 6
	%	%	%	%	%	%
H_2					0.9	1.1
CH_4					5.9	6.3
C_2H_2					2.6	3.5
C_2H_4			0.7	0.7	5.3	4.7
C_2H_6					1.4	1.1
C_3H_4	0.7	1.0	.3	1.4	6.7	6.6
C_3H_4O			.3	0.8		
C_3H_6			.1	.7	8.2	5.6
C_3H_6O			.3			
C_4H_4			.4		1.2	0.5
C_4H_6			.3		1.4	3.0
C_4H_8			2.0	1.0	1.3	2.0
$C_5H_8O_2$	93.0	95.4	80.5	83.1	16.5	9.3
C_5H_8			0.3			
C_5H_{10}			1.0	1.0	0.7	2.0
C_5H_{12}			0.7			
C_6H_6	0.1		.2		1.8	1.9
CO	2.3	0.8	.6	1.8	31.3	31.4
CO_2	0.3	.5	1.1	0.7	9.8	12.8
V_{pyr}	3.6	2.3	11.2	8.8	5.0	8.2
Total	100.0	100.0	100.0	100.0	100.0	100.0

[a] Components are in weight percent of total volatiles.

5. Discussion

As indicated in this paper, the method of heating a polymer sample consisted in moving quickly a furnace preheated to the required temperature into position to surround the sample. It is safe to assume that in the earlier work below 500 °C and also in most cases in the present work at 500 °C most of the pyrolysis took place at or near the specified temperature since the reactions proceed at a moderate rate. However, at the temperatures of 800 and 1,200 °C, where the rates of degradation are extremely high, it is quite certain that most of the volatilizable part of a given sample would degrade

and evaporate while its temperature was rising from room temperature to 800 or 1,200 °C. An idea of the speeds of reactions at these temperatures can be gained from the fact that below 500 °C the rates were found generally to double for every rise of 10°. The only limitation on this rate is the limited rate of heat transfer to the sample to furnish the heat required in the endothermic reactions. Under these circumstances the data obtained at the higher temperatures indicate only a general trend in the results of pyrolysis as a function of temperature, on the assumption that a higher initial temperature results in a higher pyrolysis temperature.

Fraction V_{pyr} from pyrolysis of the various polymers discussed in this paper consisted of molecular fragments too large to be analyzed by the mass spectrometer at our disposal, and the amounts collected were too small to be analyzed even by microchemical methods. Instead, the fractions were checked for their average molecular weight by a microcryoscopic method. The results are shown in table 15. Results for polymethylene are shown for comparison. Here again, as in the case of the lower molecular weight fractions, the higher the temperature of pyrolysis the greater is the fragmentation of the products, except in the case of polystyrene. It can be safely assumed that the V_{pyr} fragments consist of parts of the main chain, partially degraded.

TABLE 15. *Average molecular weight of fraction* V_{pyr} *from pyrolysis of polymers at various temperatures*

Polymer	Temperature of pyrolysis		
	500 °C	800 °C	1,200 °C
Polystyrene	264	372	476
Poly(α-methylstyrene)			309
Polypropylene	854		526
Polyisobutylene	543		358
Poly(methyl methacrylate)			245
Polymethylene, in vacuum	690	562	473
Polymethylene, in helium	324	277	250

Another point to be considered in connection with this work is the mechanism of degradation. The results of measurements of relative amounts of the gaseous fractions and their chemical composition reflect two principal mechanisms: (a) a primary thermal degradation, and (b) a subsequent degradation involving thermal and catalytic cracking reactions in the hot chamber, similar to those that take place in petroleum cracking.

Results of pyrolysis at 500 °C do not differ essentially from those obtained previously at lower temperatures. However, results of pyrolysis at 800 and 1,200 °C show a conspicuous departure from those obtained below about 500 °C. This departure consists mainly in an increased fragmentation of the degradation products and in the appearance of V_{pyr} fraction in some cases where such a fraction is absent at lower temperatures. Pyrolysis in a neutral atmosphere such as helium also results in greater fragmentation of the volatile products due to their slower escape from the hot zone. Thus, in the case of polystyrene, monomer is the main constituent in the V_{25} fraction when pyrolysis in a vacuum takes place at temperatures up to 500 °C. At 800 and 1,200 °C the yield of monomer is diminished, and C_2H_2, C_2H_4, and C_6H_6 appear in increasing amounts. Similarly, pyrolysis at 800 and 1,200 °C in helium at atmospheric pressure yields small amounts of monomer, only 0.8 wt-% at 1,200 °C, and appreciable amounts of C_2H_2 and C_6H_6. Formation of C_6H_6 can be assumed to take place as follows:

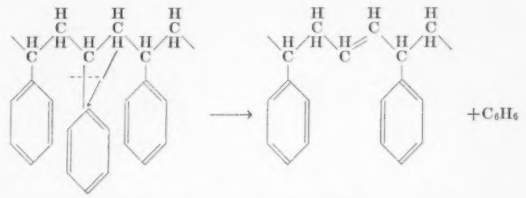

or a phenyl group may split off as a free radical causing a scission in the backbone of the chain

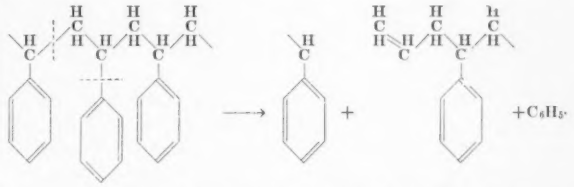

The free radicals could then absorb H from the surrounding medium causing further scissions. Compounds C_2H_2 and C_2H_4 could form through scissions in the backbone of the polymer chain, or they could form from the monomer. In either case, these reactions result in a decrease of the yield of monomers.

With polytetrafluoroethylene, the main product of pyrolysis at the lower temperatures is C_2F_4, with small amounts of C_3F_6 and CF_4. At the higher temperatures C_2F_4 is still the dominant product, but in addition there also appears small amounts of HF. There is no fraction V_{pyr} formed at temperatures up to 500 °C and only a small amount at 800, but at 1,200 °C the yield of this fraction is considerable. It was postulated in our earlier work [9] that this polymer breaks up at free radical ends of chains by an unzipping process to yield mostly monomers. The overall reaction is of first order [9, 12, 13]. This can be explained on the ground that the unzipping process is preceded by a process of scission of C—C chain bonds into free radicals. This reaction is slower and random and is therefore rate determining and of first order. The absence of any V_{pyr} at low temperatures is probably due to the fact that at these temperatures unzipping, once started, proceeds until the whole chain is consumed, so that large fragments (V_{pyr}) do not appear among the volatile products. At the higher temperatures some of the shorter free radical chains evaporate before they have a chance to decompose into monomer, thus yielding volatile fractions of V_{pyr} size.

With poly(α-methylstyrene) the distinction between low and high temperature pyrolysis is clear-cut. At lower temperatures the product consists

of 100 percent monomer. At 800 and 1,200 °C various smaller fragments, from H_2, CH_2, C_2H_2, and other small hydrocarbons up to C_7H_8 make their appearance. In addition to these there are among the degradation products at the higher temperature a considerable amount of V_{pyr} size fragments, whereas at the lower temperature the yield of V_{pyr} is zero. The mechanism of degradation of this polymer is similar to that of polytetrafluoroethylene, and the reaction is of first order [14]. The appearance of larger molecules found in fraction V_{pyr} could be caused by the vaporization at higher temperatures of some of these molecules before they have time to break up into the monomer by the unzipping process. The formation of small molecules found in fraction V_{-190} is most likely caused by cracking of the larger molecules in the hot zone of the apparatus.

In the pyrolysis of polypropylene, the monomer, C_3H_6, appears in small amounts below about 500 °C. At 800 and 1,200 °C its yield is considerable. The reverse is true of V_{pyr}, due to the cracking of the V_{pyr} fragments into smaller molecules in the hot zone. There is some H_2 and larger amounts of CH_4, C_2H_2, C_2H_4, C_2H_6, C_3H_4, C_4H_8, and C_5H_{10} at the higher temperatures than at the lower. In this respect the mechanism of degradation of polypropylene is similar to that of polymethylene [6].

Pyrolysis of polyisobutylene generally follows the same pattern as that of polypropylene, except for the fact that at 800 °C the yield of monomer is higher than at 500 or at 1,200 °C. On comparing the yield of V_{pyr} for the three temperatures, it appears that there is an inverse relationship between these products so that one may assume that at 500 and 800 °C the increase of monomer yield is at the expense of V_{pyr}.

Degradation of poly(methylmethacrylate), like that of polytetrafluoroethylene and poly(α-methylstyrene), yields at the higher temperatures less amounts of monomer than at the lower temperatures. Judging from table 14, the monomer decomposes at the higher temperatures, particularly at 1,200 °C, to yield considerable amounts of CO, CO_2, CH_4, C_2H_2, C_2H_4 and similar compounds.

6. References

[1] T. Midgley and A. L. Henne, J. Am. Chem. Soc. **51,** 1215 (1929).
[2] H. L. Bassett and H. G. Williams, J. Chem. Soc. p. 2324 (1932).
[3] B. B. S. T. Boonstra and G. J. VanAmerongen, Ind. Eng. Chem. **41,** 161 (1949).
[4] S. L. Madorsky, S. Straus, D. Thompson, and L. Williamson, J. Research NBS **42,** 499 (1949).
[5] S. L. Madorsky and S. Straus, J. Research NBS **63A,** 261 (1959).
[6] S. L. Madorsky and S. Straus, Soc. Chem. Ind. (London) Monograph No. 13, p. 60 (1961).
[7] S. L. Madorsky and S. Straus, Modern Plastics **38,** 134 (1961).
[8] S. L. Madorsky, J. Soc. Plastic Engineers **17,** 665 (1961).
[9] S. L. Madorsky, V. E. Hart, S. Straus, and V. A. Sedlak, J. Research NBS **51,** 327 (1953).
[10] S. Straus and S. L. Madorsky, J. Research NBS **50,** 165 (1953).
[11] S. L. Madorsky and S. Straus, J. Research NBS **53,** 361 (1954).
[12] S. L. Madorsky and S. Straus, J. Research NBS **64A,** (Phys. and Chem.), No. 6, 513–514 (Nov.–Dec. 1960).
[13] Henry L. Friedman, Paper presented at the 136th Meeting of the American Chemical Society, Atlantic City, New Jersey, September 1959.
[14] S. L. Madorsky, J. Polymer Sci. **11,** 491 (1953).

(Paper 66A5–175)

JOURNAL OF RESEARCH of the National Bureau of Standards—A. Physics and Chemistry
Vol. 66A, No. 5, September–October 1962

Lattice Frequencies and Rotational Barriers for Inorganic Carbonates and Nitrates From Low Temperature Infrared Spectroscopy

R. A. Schroeder,[1] C. E. Weir, and E. R. Lippincott [2]

(May 29, 1962)

Infrared absorption spectra of inorganic nitrates and carbonates have been obtained on single crystals at room temperature, under liquid nitrogen refrigeration and under liquid helium refrigeration. Diffuse absorption observed in the room temperature spectra between about 1400 cm^{-1} and 700 cm^{-1} is resolved under liquid helium refrigeration into a large number of bands not attributable to fundamentals or combinations of fundamental frequencies of the anions. Almost all of these bands are readily interpreted as summation bands of fundamental frequencies with successive levels of a librating oscillator. The libration is considered to represent a planar torsional oscillation of the anion about the trigonal axis. The librational frequency depends in part on the crystal structure and on the ions. In a given material the librational frequency as determined from successive bands is reasonably constant. In the substances studied the librational frequency varied from about 15 cm^{-1} to 30 cm^{-1}.

Band limits observed in the spectra are interpreted as representing rotational energy barriers. These barrier heights are approximately 200 cm^{-1} with some dependence on the crystal structure and the ions involved. Barrier heights calculated from a cosine potential function agree reasonably well with the observed barriers for the cubic and calcite structures. Similar calculations have not been made for other structures studied because of doubtful assignments or unknown structural details. In particular, spectra of the aragonite structures are remarkable in detail and complexity, and have not been analyzed. However, the details of these and all other spectra studied appear to involve similar phenomena.

1. Introduction

Free rotation of atomic groups in the solid phase was suggested initially by Pauling in 1930 [59] [3]. A number of reports appeared subsequently presenting evidence for free rotation in solids [5,25,32, 39,40,41,65]. In general, the experimental evidence presented consisted chiefly of plausible interpretations of X-ray structure determinations of various solid phases in the ammonium salts and in metal nitrates and carbonates. It was argued that essentially free rotation of the nonspherical ion would be necessary to produce a NaCl-type structure which was required by the X-ray data from these salts. In other structures containing nitrate and carbonate ions free rotation of the ion about the trigonal axis was proposed to satisfy the X-ray data. It has been argued more recently that a disoriented arrangement of the nonspherical ions would also satisfy the diffraction data without the necessity for free rotation [45].

Completely unambiguous evidence of rotation in solids has been sought actively. The question has been pursued with an increasing number of experimental techniques being brought to bear such as X-ray studies [6, 22, 45, 68], specific heat measurements [48], infrared spectroscopy [34, 35, 74, 75], Raman spectroscopy [9, 10, 11, 12, 25, 36, 42, 43, 44, 55, 62, 63, 64], nuclear magnetic resonance [3, 4, 16, 28], and neutron diffraction [18, 31, 49, 50, 53]. In each of these fields the literature is extensive and the references cited are not exhaustive but are confined to the inorganic materials of interest here. Almost without exception, all studies agree that free rotation does not take place at ordinary temperatures. However, they conclude that hindered rotation, i.e., a torsional oscillation or libration does take place with potential barriers sufficiently low that disordering may occur near room temperature. The only exceptions appear to be in NH_4I where there is evidence [61, 72] from heat capacity and infrared data that the NH_4^+ rotates about an N–H–I axis above 75 °K, and in a recent report [18] of free rotation in KCN based on neutron diffraction studies. The present ideas suggest librating ions are able to surmount the barriers at a rate sufficiently great to satisfy the X-ray structure requirements. In effect the findings substantiate the suggestions advanced by Frenkel in 1943 [23] who opposed Pauling's rotation hypothesis and proposed instead torsional oscillation with a finite disordering rate.

Harmonic librations are lattice modes and might be detected by Raman or infrared spectroscopic studies. The frequencies expected for these modes cannot be predicted without knowledge of the potential energy function describing the potential barrier. Although

[1] Present address, University of Southwestern Louisiana, Lafayette, La.
[2] Consultant to the Mineral Products Division, National Bureau of Standards. Present address, Dept. of Chemistry, University of Maryland, College Park, Md.
[3] Figures in brackets indicate the literature references at the end of this paper.

the rotational frequencies of the free ion can be calculated readily it is only possible to predict that the frequency of the restricted harmonic librator must be greater than that for the free rotator. Low frequency shifts have been found in the Raman spectra of inorganic solids for which there is independent evidence of anion or cation libration [for example, preceding references on Raman spectra]. Certain Raman lines have been attributed to frequencies arising from harmonic libration modes; however, there is no assurance that these represent the fundamentals rather than overtones or combinations. There is also no conclusive evidence for harmonic libration in the infrared spectra of solids, although Hexter [34, 35] has proposed that certain complex high frequency overtone and combination bands in the 3000 cm^{-1} to 5000 cm^{-1} region of carbonates and nitrates arise from libration combinations. Early reststrahlen studies [51] have shown the existence of low frequency infrared bands whose exact origin is unknown. These bands have been widely attributed to lattice vibrations of an unspecified nature.

This paper will present evidence for libration in the infrared spectra of anhydrous metal nitrates and carbonates. These substances have been the subject of infrared studies since the early work of Schaefer, Bormuth, and Matossi [66] and the spectra are believed to be well understood insofar as the assignments of the six fundamental vibrations of the free nitrate and carbonate ions [30, 33, 38] are concerned. However, the strong overtone and combination bands and their complexity have been the source of recent studies [29, 34, 35]. The very intense and obviously complex band containing the antisymmetric stretching band has also been of concern [52]. Newman and Halford [57, 58] observed in the infrared spectra of crystalline $Pb(NO_3)_2$ and $TlNO_3$ bands that were not attributable to fundamentals of the anions. They were assigned to sum and difference bands of the symmetric stretching vibration and a low lying (30 cm^{-1}) lattice mode. Recently Gross and Shultin [26] studied $Ba(NO_3)_2$ and $Pb(NO_3)_2$ with similar results and succeeded in resolving several combination bands. Both of these studies used low temperatures (liquid nitrogen temperature) to improve the resolution. A careful examination of the pioneering spectra given by Schaefer, Bormuth, and Matossi [66] on the crystalline carbonates shows clear evidence of weak bands in the frequency range containing the fundamentals. In this early work some attempt was made to explain these bands as sum and differences between fundamentals or between fundamentals and lattice frequencies reported from reststrahlen experiments, but with only partial success.

Recent studies in this laboratory of the effect of high pressure on the infrared spectra of crystalline nitrates and carbonates showed the sum and difference modes previously reported in the heavy metal nitrates and produced evidence for additional bands of this type at elevated pressures. These observations motivated a serious study of the combination bands at 1 atm in an attempt to understand the behavior at elevated pressures.

It is obvious that extensive combinations involving sum and difference bands between a lattice fundamental of the order of 30 cm^{-1} and the internal fundamentals of the anion found between 700 cm^{-1} and 1500 cm^{-1} will produce such a complex overlapping band structure as to make analysis extremely difficult. If the spectrum were simplified by removing the difference bands through cooling as suggested by Hornig [38] the fact that 30 cm^{-1} levels are involved would require very low temperatures. Simple calculations showed that at the temperature of liquid nitrogen, large numbers of ions would be in upper states when the levels are spaced 30 cm^{-1} apart. At the temperature of liquid helium, however, almost all of the ions would be in the ground state. This report presents data on the room temperature and on the low temperature—liquid nitrogen and liquid helium temperature—infrared spectra of "thick" (about 0.010 in.) crystals of metal nitrates and carbonates. The spectra are interpreted in terms of librations of the anions.

2. Experimental Method

2.1. Apparatus

Most infrared spectra were recorded on a commercial double-beam spectrometer using NaCl prisms. To permit the use of small thick crystals the spectrometer was equipped with a microfocusing unit employing reflecting optics. This unit was modified for use with the spectrometer and further to permit introduction of the tip of a Dewar into the focal region. The modified unit produced a focal spot 0.060 to 0.080 in. in diameter within a working space 1⅛ in. wide. Approximately 45 to 50 percent of the normal energy was available with the microfocus unit. Only a single unit was available, and this increased the path length of the specimen beam by about 18 in. over the path length of the reference beam. Therefore, complete compensation for water vapor and carbon dioxide was not achieved. Weak bands for these materials appeared in all spectra near 1700 cm^{-1}, 2350 cm^{-1}, and 3500 cm^{-1}. These regions were not of particular interest in the data but caution was exercised in interpreting weak bands near these frequencies.

The overtone and combination region at frequencies above 1700 cm^{-1} was studied on a double beam spectrometer using a grating to provide greater resolution in the higher frequency region. This unit was equipped with a reflecting microfocus unit in both beams to provide for better compensation. Weak bands, particularly in the 3500 cm^{-1} region, indicated incomplete compensation.

The low temperature equipment was constructed to utilize an available commercial Dewar. This was a triple-wall stainless steel unit open at the bottom to permit access to the tip of the innermost liquid container. The central wall comprised a radiation shield that extended well below the liquid reservoir. A specimen holder was fabricated from a ½ in. diam bar of copper. The bar was approxi-

mately 2 in. long, threaded at the top end to screw tightly into the tip of the liquid reservoir and machined down at the bottom end to give a flat plate ½ in. square times ⅛ in. thick. The length of 2 in. was necessary to permit specimens mounted in the flat bottom plate to be positioned in the focal spot of the rather large ellipsodial focusing mirror. The specimens were mounted over holes 0.060 in. in diameter drilled in the flat plate. Five holes were drilled in two rows, the top row containing three holes, the bottom row two. Holes were located ⅛ in. apart and holes in the two rows were staggered so that a single hole could be brought into the focal spot with no stray radiation through the adjacent holes. Each hole was counterbored from each side of of the plate to a diameter of ⅛ in. and of such depth that a flat web of copper approximately 1/32 in. thick remained in the center of the plate. Counterboring permitted entry of the highly convergent cone of radiation and afforded a relatively shallow well in which the crystals were mounted. The Dewar was closed with a brass housing which enclosed the copper bar and was equipped with two NaCl windows located opposite the flat plate on the bottom of the copper bar. Vacuum closure between the housing and the outer wall of the Dewar was accomplished satisfactorily with a rubber O-ring seal. The restricted working space between the ellipsoidal mirrors required miniaturization and although considerable clearance between brass housing and copper bar was provided, it did not prove feasible to extend the radiation shield around the copper bar inside the housing. Attempts to insert such a shield invariably resulted in a thermal short circuit produced by nonuniform contraction of the inner container or the radiation shield assembly on cooling. Some radiation protection was provided by wrapping the copper bar with bright aluminum foil. The Dewar was evacuated through a cutoff valve by means of an oil diffusion pump backed up by a mechanical pump. The complete Dewar assembly was rigidly mounted in a rack equipped with guides and adjusting screws to permit controlled motion in three perpendicular directions. This mount was essential to afford rapid, controlled centering of the small holes in the equally small focal spot.

Five crystals, each covering a single hole, were studied in a single experiment. The small crystals required (⅛ in. in diameter) were generally available from reagent bottles or crystal fragments. Crystals were selected for clarity and shape, one reasonably flat surface being required. They were then filed down to fit snugly against the 1/32 in. web at the bottom of the ⅛ in. wells, and were cemented into place against the web and the walls of the well with a low temperature resin. All crystals were mounted on the same side of the web and in use this side was turned away from the incident radiation. This arrangement minimized heating of the crystals by unused radiation and eliminated problems arising from absorption by the adhesive. Crystals were checked for thickness while in place by their spectra; if too thick, they were thinned in the center by using water or dilute acid. In these studies estimated crystal thicknesses ranged from about 0.001 to 0.080 in.

In a given experiment spectra were recorded at room temperature and, following exhaustive evacuation of the Dewar, were recorded at liquid nitrogen temperature. If the runs at liquid nitrogen temperature proved successful, liquid helium was introduced into the Dewar immediately after removing the liquid nitrogen and the final spectra were then recorded. In an ordinary experiment with approximately 1 liter of liquid helium in the Dewar, the rate of boil-off of the helium was sufficiently low to provide cooling for at least 4 hr with the energy input supplied by the spectrometer and the normal environment. This period was more than sufficient to obtain the spectra of the five specimens. Following an experiment the crystals were found to be still firmly cemented in place and, although generally fractured by thermal contraction or the stresses produced by the adhesive, appeared to be in good thermal contact with the copper. Each cooling cycle appeared to produce further fracturing which tended to increase scattering losses and reduce transmission. Thus it was found to be desirable, wherever possible, to obtain all spectra on a single cooling cycle.

In these experiments it was not considered feasible to attempt to measure the temperature of the small crystal specimens. The temperature of the flat copper strip was measured in a typical experiment and with liquid nitrogen in the Dewar a value of 86 °K was obtained while with liquid helium the temperature was found to be 27 °K. These temperatures represented the temperature of the copper bar at a point as far from the coolant as possible, measured with a gold-cobalt alloy-copper thermocouple [54]. The actual temperature of a crystal might have been higher because of the energy flux from the focal spot, with the temperature being determined by the absorption, the specific heat, the thermal conductivity of crystal and cement, and the thermal barriers between crystal and cement and copper, or lower because of the thermal energy introduced by the thermocouple leads. On the other hand the thermal path was very short and the crystal was nearly surrounded by the cold copper strip. In several spectra of interest the difference band between the symmetric stretching mode and a level of the order of 30 cm^{-1} was identified. This band in effect represented a thermometer built into the spectrum and observations showed that the difference band, although somewhat reduced in intensity, was still very prominent at the temperature of liquid nitrogen. With liquid helium in the Dewar, however, the difference band was effectively missing. This result may be taken as evidence that the temperature of the crystal was sufficiently low to remove all difference modes involving energies of 30 cm^{-1} or more. The removal of difference bands was the primary objective of cooling and the result showed that, irrespective of the absolute temperature of the crystal, the resulting spectra could be interpreted in terms of the fundamentals

and their summation bands only. In tabulating the spectra the temperatures will be described as liquid nitrogen temperature and liquid helium temperature with the clear understanding that the temperatures of the crystals may differ appreciably from the boiling temperatures of these liquids.

2.2. Materials Studied

The following nitrates were studied: $NaNO_3$, KNO_3, $RbNO_3$, $CsNO_3$, $TlNO_3$, $AgNO_3$, $Sr(NO_3)_2$, $Ba(NO_3)_2$, and $Pb(NO_3)_2$. Of these all except $RbNO_3$, $CsNO_3$, and $TlNO_3$ were reagent grade chemicals of high purity. These three materials were recrystallized from aqueous solution at 55 °C to effect further purification and to prepare suitable crystals. This technique was used by Newman and Halford [58] to prepare large $TlNO_3$ crystals. Suitable crystals for the other materials were obtained from the substances as received.

The following carbonates were studied: $MgCO_3$, $CaCO_3$, $SrCO_3$, $BaCO_3$, $PbCO_3$, $FeCO_3$, and $MnCO_3$. These were all natural minerals obtained in large crystals. The materials and their sources are as follows:

$MgCO_3$—magnesite—origin uncertain (large clear crystals)
$CaCO_3$—calcite—Brazil (large clear crystals)
$SrCO_3$ — strontianite — Argyll, Scotland (large translucent crystals)
$BaCO_3$ — witherite — Lancashire, England (large translucent crystals)
$PbCO_3$—cerrusite—Southwest Africa (large clear crystals)
$FeCO_3$—siderite—Roxbury, Conn. (opaque masses, obviously impure)
$MnCO_3$—rhodochrosite—Kusatuni Kaga, Japan (opaque—large crystals)
$CaCO_3$—aragonite—Cianciano, Sicily (large translucent crystal).

Spectrochemical analyses were performed on all carbonates except the $CaCO_3$ (aragonite). Aside from trace impurities the following metallic impurities were found in quantities up to a maximum of 1 percent. $MgCO_3$-Fe; $CaCO_3$ (calcite)—none; $SrCO_3$-Ca; $BaCO_3$-Sr; $PbCO_3$—none; $MnCO_3$-Ca,Fe, Mg; $FeCO_3$-Mg,Mn,Si. The impurities except in the cases of $MnCO_3$ and $FeCO_3$ appear to be of negligible importance. Inspection of the infrared spectra indicates no evidence for the strongest fundamentals of the major contaminant.

The materials studied fall into the following five classes at room temperature.

(1) calcite type—space group D^6_{3d}-$NaNO_3$, $MgCO_3$, $CaCO_3$ (calcite), $MnCO_3$, and $FeCO_3$ [71];
(2) aragonite type—space group V^{16}_h-KNO_3, $CaCO_3$ (aragonite), $SrCO_3$, $BaCO_3$, and $PbCO_3$ [7, 8, 17, 71, 79];
(3) hexagonal—space group C^2_{3v}-$CsNO_3$, $RbNO_3$ [19, 20, 21, 60, 76];
(4) orthorhombic — space group uncertain — $TlNO_3$, $AgNO_3$ [37, 71];
(5) cubic—space group T^6_h-$Sr(NO_3)_2$, $Ba(NO_3)_2$, $Pb(NO_3)_2$ [71].

Specific heat data are available for most of these substances between room temperature and lower temperatures which range from 55 to 13 °K with no reports of any structural changes. $CaCO_3$ (calcite), $CaCO_3$ (aragonite), $SrCO_3$, and $BaCO_3$ were studied by Anderson down to 55 °K [1]. Anderson also has reported data down to 55 °K for $MgCO_3$, $PbCO_3$, $MnCO_3$, and $FeCO_3$ [2]. The data on $CaCO_3$ (aragonite) have been extended down to 23 °K by Gunther [27] with no observed transitions. Latimer and Ahlberg have studied $Ba(NO_3)_2$ [46] and $TlNO_3$ [47] down to about 16 °K while Nernst and Schwers [56] have reported data on $CaCO_3$ (calcite) to a temperature of 22 °K. Shomate and Kelley [67] investigated $Ba(NO_3)_2$ to 53 °K and similar data were given to 13 °K for $AgNO_3$ by Smith, Brown, and Pitzer [69]. Finally, data down to 15 °K were obtained by Southard and Nelson for KNO_3 and $NaNO_3$ [70]. In no case were any irregularities in the specific heat curves observed, therefore, no transitions are known to occur between room temperature and the temperatures given. These temperatures may be above the lowest temperature to which the materials were subjected in these studies; however, the specific heat data assure that no transitions occur in the major portion of the temperature range. Low temperature data do not appear to be available for $Sr(NO_3)_2$, $Pb(NO_3)_2$, $RbNO_3$, and $CsNO_3$. By analogy with $Ba(NO_3)_2$ it would be expected that $Sr(NO_3)_2$ would exhibit a regular low temperature behavior. It would appear much less certain that $Pb(NO_3)_2$ would behave similarly. The $RbNO_3$ and $CsNO_3$ represent different systems and to resolve the question low temperature X-ray diffraction patterns were obtained on $RbNO_3$ and $CsNO_3$ to 77 °K. The results showed that no structural changes occurred between room temperature and 77 °K. Behavior at temperatures below 77 °K was not studied.

2.3. Polarization and Orientation Effects

The infrared beam underwent at least three reflections in the process of being focused on the crystal studied. Therefore, some uncertainty existed concerning the polarization of the incident beam. To provide a partial answer to the experimental effects to be expected, two specimens from a single crystal of calcite were studied, one cut parallel and the other cut perpendicular to the optic axis. The absorption spectra of these crystals are shown in figure 1. The spectra are displaced vertically to eliminate overlapping. It will be noted that the spectra are similar. Although some major differences in relative intensity are observed in the two spectra, both crystals show essentially the same absorption bands. It is concluded, therefore, that the degree of polarization of the beam is so small that essentially the same absorption spectrum will be shown by randomly oriented, anisotropic crystals.

3. Results and Discussion

3.1. Method of Presentation

There are a large number of spectra to be presented and discussed and the following pro-

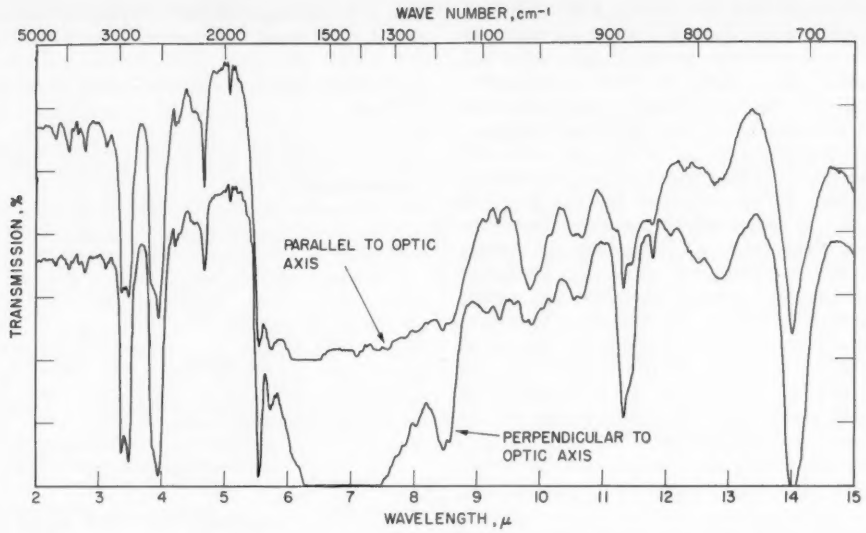

FIGURE 1. *Infrared absorption spectra of calcite crystals of different orientations.*

cedure is employed: (a) The spectra are subdivided with respect to crystal structure because there appear to be good correlations within a given structure. (b) Spectra are shown for each material studied. For each crystal type except the aragonite type at least one spectrum is shown on an enlarged scale for each of the three temperatures studied. These spectra are given in the same figure but displaced vertically. For other materials of the same crystal type two spectra on a small scale are shown, one at room temperature, and the other at liquid helium temperature. These spectra are drawn on the same figure but displaced vertically. (c) The discussion will also be divided, first according to the vibrations of interest. These sections are then further subdivided according to crystal structure. The major discussion will consist of three parts: first, the fundamentals; second, librations; and third, fundamental overtones and combinations.

3.2. Fundamental Internal Frequencies

A discussion of the fundamental internal frequencies for the carbonate and nitrate ions will be given before any additional features of the spectrum are analyzed in terms of lattice modes or combinations. This analysis may be carried out to three stages of approximation for the selection rules applicable to possible infrared transitions. First, the symmetry of the free ion may be assumed, ignoring any effects due to the crystal field symmetry. This assumption would not be expected to be a valid approximation to the actual situation. Second, the site group approximation may be used in which the selection rules for the ions are derived from the symmetry of the site which they occupy in the crystal lattice. In effect the ion is considered as if it were an independent entity possessing the symmetry of the lattice site. This treatment will predict some effects arising from the crystal field symmetry but will not adequately describe those effects due to the interaction of a given ion with its neighbors. Finally the factor group analysis may be considered. This treatment considers the vibrations of the crystal as arising from the motion of the m atoms in the unit cell to give $3m$-3 fundamentals (including both internal and lattice modes). The selection rules are derived from the factor group symmetry which is isomorphous with the space group symmetry. The factor group analysis will differ from the site group analysis in that coupling of vibrations between ions in different sites is included. Vibrations may show higher degeneracy, may become inactive, or may be repeated several times compared to the results of the site group approximation.

a. Free Ion Approximation

Free carbonate and nitrate ions are classified in the point group D_{3h}. Table 1 gives the spectral activity, symmetry species, types of internal frequencies, and the lattice modes derived from transla-

TABLE 1. *Spectral activity for nitrate and carbonate ions of symmetry* D_{3h}

Species	Activity	Internal mode	Lattice modes derivable from translation or rotation
A_1'	Raman	ν_1	
A_1''			
A_2'			$L(R_z)$
A_2''	I.R.	ν_2	$L(T_z)$
E'	I.R., Raman	ν_3, ν_4	$L(T_x, T_y)$
E''	Raman		$L(R_x, R_y)$

I.R. —infrared active; R—Raman active.
L(T)—lattice mode derivable from translation along x, y, z, axis.
L(R)—lattice mode derivable from rotation about x, y, z, axis.
ν_1 —symmetric stretch; ν_2—out-of-plane bend; ν_3—degenerate antisymmetric stretch; ν_4—degenerate in-plane bend.

tions and rotations of the free ion. For the free ion, the active fundamentals and their approximate positions are: the out-of-plane bending (ν_2) observed generally near 850 cm^{-1}; the degenerate antisymmetric stretching (ν_3) which is usually very intense and observed in the 1400 cm^{-1} to 1500 cm^{-1} region; and the degenerate in-plane bending (ν_4) usually found near 720 cm^{-1}. The symmetric stretching mode (ν_1) is inactive in the infrared for the free ion approximation but is expected to have a frequency near 1060 cm^{-1}. Translations of the free ion would be infrared active (species A_2'' and E') but the modes derived from rotations of the free ion would be inactive in the infrared spectrum. The frequencies of the lattice modes would be expected to be less than 500 cm^{-1} and, therefore, unobserved in the present study. However, combinations of these modes with fundamental frequencies would be infrared active and might be observed. Combinations of fundamentals with a number of other lattice modes would be restricted by the D_{3h} symmetry.

Crystals with the calcite, cubic, hexagonal, and orthorhombic structures show spectra conforming reasonably well with the predictions of the free-ion selection rules insofar as the fundamental internal frequencies are concerned. ν_2 and ν_4 are always observed in the expected positions although ν_4 is occasionally weak in some of the nitrates. ν_3 is always observed but with such great intensity that it is not possible to determine whether it is a single or multiple band or even to locate its position with reliability. The symmetric stretching band ν_1 is usually not observed as expected or when present is generally weak. The free-ion model must be rejected because it does not adequately describe the complex spectra of the aragonite crystals shown in figures 9 to 15 nor does it permit sufficient flexibility in the selection rules for combinations between internal and lattice modes to explain the elaborate band structure observed in most specta. For example the D_{3h} selection rules predict that combinations of ν_1 with the lattice libration frequency derived from rotation in species A_2' should be inactive. For reasons to be discussed later a whole series of such bands are believed to be present in the spectra.

b. Site Group Approximation

The selection rules for the various crystal structures in the site group approximation may be obtained from the space group symmetry and the tables given by Halford [30] showing the various sites for each space group. In the calcite type crystals of space group D_{3d}^6 containing 2 molecules per unit cell, the anions occupy sites of D_3 symmetry and the cation's sites of symmetry C_{3i}. In the cubic structures of space group T_h^6 containing 4 molecules per unit cell the anions must lie on sites with symmetry C_3 and the cations on sites of symmetry C_{3i}. Similarly in the aragonite structures of symmetry V_h^{16} with 4 molecules per unit cell both anions and cations occupy sites of symmetry C_s. The hexagonal and orthorhombic crystals will not be discussed because of uncertainties concerning the space groups. The results of the site group approximation for the selection rules are given in table 2.

TABLE 2. *Spectral activity for nitrate and carbonate ions in calcite, aragonite, and cubic structures for the site group approximation*

Calcite structure (site symmetry D_3)

Species	Activity	Internal mode	Lattice mode for anion*
A_1	Raman	ν_1	
A_2	I.R.	ν_2	L(T), L(R)
E	I.R., Raman	ν_3, ν_4	L(T), L(R)

* There are 3 lattice modes of translational origin associated with the cations on sites C_{3i} which are infrared active.

Aragonite structures (site symmetry C_s)

Species	Activity	Internal mode	Lattice mode for anion*
A′	I.R., Raman	ν_1, ν_3, ν_4	2L(T), L(R)
A″	I.R., Raman	ν_2, ν_3, ν_4	L(T), 2L(R)

* There are 3 lattice modes for the cations on sites of symmetry C_s which are active in both infrared and Raman.

Cubic structures (site symmetry C_3)

Species	Activity	Internal mode	Lattice mode for anion*
A	I.R., Raman	ν_1, ν_2	L(T), L(R)
E	I.R., Raman	ν_3, ν_4	L(T), L(R)

* There are 3 lattice modes associated with the cations on sites of symmetry C_{3i} which are inactive in the Raman but active in the infrared spectrum (species B_u and E_{1u}).

Calcite type structures. In the calcite type crystals the selection rules require that ν_2 (species A_2) and ν_3 and ν_4 (species E) are infrared active while ν_1 remains infrared inactive. This prediction agrees with the observed fundamentals but again the selection rules are too restrictive and fail to account for the large number of sum and difference modes believed to be due to lattice modes. As an example, lattice modes of rotational or translational origin in species A_2 would be expected to give a series of combination bands with every other band forbidden by the selection rules. This is not believed to be the case.

Aragonite type structures. In these structures the site symmetry C_s yields selection rules requiring the degenerate stretching and bending modes, ν_3 and ν_4, to be split and the symmetric stretching mode, ν_1, to be active in the infrared spectrum. The out-of-plane bending ν_2 remains active. The low temperature spectra show that ν_3 is split (for example, see spectrum of $SrCO_3$). However, there appear to be at least three components of ν_3 in $SrCO_3$. This does not agree with the selection rules which predict two components only. Similarly, ν_1 is active as predicted but in addition at least one other component

of ν_1 appears to be present which is unaccounted for. Considerations of a similar nature arise regarding ν_2 and ν_4.

Cubic structures. With the site symmetry C_3 the selection rules predict that in addition to ν_2 (species A) and ν_1 and ν_4 (species E) that ν_1 (species A) should also be infrared active. Spectra for the cubic crystals show a very weak band in this region which may represent the ν_1 vibration.

It is clear that while the site group approximation gives results which are in better agreement with the observations than the free ion approximation, the apparent discrepancies between prediction and observations in the aragonite structures makes the validity of the approximation questionable. The applicability of this treatment has been discussed previously [13] and it has been pointed out that the site group approximation is less applicable to ionic crystals than molecular crystals because of the much stronger coupling in ionic lattices.

c. Factor Group Approximation

Selection rules for the calcite, aragonite, and cubic crystal types under the factor group approximation are given in table 3. The internal and lattice frequencies are classified with regard to their respective symmetry species.

TABLE 3.—*Factor group selection rules for the calcite, aragonite and cubic structures*

Species	Activity	Internal mode	Lattice modes
Calcite structure-space group D_{3d}^6; 2 molecules/unit cell; total frequencies—27			
A_{1g}	Raman	ν_1	1
A_{1u}		ν_2	1
A_{2u}	I.R.	ν_2	2
A_{2g}		ν_1	1
E_{1u}	I.R.	ν_3, ν_4	3
E_{1g}	Raman	ν_3, ν_4	2
Aragonite structure-space group V_h^{16}; 4 molecules/unit cell; total frequencies—57			
A_g	Raman	ν_1, ν_2, ν_3, ν_4	5
A_u		ν_3, ν_4	4
B_{1g}	Raman	ν_3, ν_4	4
B_{1u}	I.R.	ν_1, ν_2, ν_3, ν_4	4
B_{2g}	Raman	ν_1, ν_2, ν_3, ν_4	5
B_{2u}	I.R.	ν_3, ν_4	3
B_{3g}	Raman	ν_3, ν_4	4
B_{3u}	I.R.	ν_1, ν_2, ν_3, ν_4	4
Cubic structure-space group $T^1{}_h$ 4 molecules/unit cell; total frequencies—105			
A_g	Raman	ν_1, ν_2	2
A_u		ν_1, ν_2	3
E_g	Raman	ν_3, ν_4	2
E_u		ν_3, ν_4	3
F_g	Raman	ν_1, ν_2, ν_3, ν_4, ν_3, ν_4	6
F_u	I.R.	ν_1, ν_2, ν_3, ν_4, ν_3, ν_4	8

Calcite type structures. For calcite structures, the active modes in the infrared are ν_2 (species A_{2u}), ν_3 (species E_{1u}), and ν_4 (species E_{1u}). The symmetric stretch, ν_1, is again inactive. As before, the predictions agree well with the observed fundamentals. There are now effectively no selection rules governing combinations between fundamentals and lattice modes [78].

Aragonite type structures. In these crystals the selection rules predict that three nondegenerate components of ν_3 and ν_4 (species B_{1u}, B_{2u}, and B_{3u}) should result from the splitting of the degenerate stretching and bending modes of the free ion. In the $SrCO_3$ spectrum three such bands can be observed at 1362, 1445, and 1522 cm^{-1}. These are sharp, strong, bands and may be taken to represent the three components of ν_3. The very strong broad band near 1600 cm^{-1} is believed to arise from combinations and will be discussed later. Two of the three components of ν_4 are found at 701 cm^{-1} and 711 cm^{-1} while the third may either be the weaker band near 738 cm^{-1} or be unresolved from the 701 to 711 cm^{-1} doublet. The selection rules require ν_1 and ν_2 to be infrared active in species B_{1u} and B_{3u}. The two components of ν_1 can be assigned as the two sharp bands observed near 1050 cm^{-1} and 1072 cm^{-1} in the low temperature $SrCO_3$ spectra. There are undoubtedly a number of bands, partly unresolved, near the expected position for the two components of ν_2. Some of these are undoubtedly lattice combination modes but in any case there appears to be little difficulty in concluding that ν_2 consists of at least two components. Similar assignments are possible in the other aragonite type structures. It should be noted that Decius [14, 15] has pointed out that the out-of-plane bending modes in aragonite type crystals are strongly coupled as a result of the proximity of the anions. This coupling produces a splitting of ν_2 when isotopic species are involved. The relative intensities involved here, however, appear to be too great to be attributed to the natural abundance of isotopes.

Cubic structures. In the cubic structures the factor group selection rules show that the only active infrared species is F_u with six triply degenerate internal frequencies and eight triply degenerate lattice modes. The six internal frequencies are derived from ν_1 and ν_2 and two each from ν_3 and ν_4. ν_1 is observed very weakly if at all and can hardly be considered as an active fundamental. ν_2 can only be assigned near 812 cm^{-1}, its usual position. There may be two components of ν_3 but the great intensity of the band prevents any attempts to locate their positions. The splitting of ν_3 has been observed in the cubic structures by Couture and Mathieu [10] who studied the Raman spectrum. The two components of ν_4 must be considered unresolved in the band near 722 cm^{-1} in the cubic nitrates.

Some basis must be found for the assignment of the large number of nonfundamental frequencies some of which are very strong. These bands are observed in the low temperature spectra of all the nitrates and carbonates. The factor group treatment forms an adequate basis for assigning these bands as there are in principle no selection rules governing the combinations of lattice modes with internal modes [78]. However, there is no indication of the relative intensities to be expected for sum and difference bands.

3.3. Libration-Fundamental Summation and Difference Bands in the 700 cm^{-1} to 1500^{-1} Region

In this section the large number of bands occurring in the 700 cm^{-1} to 1500 cm^{-1} region of the spectrum are discussed. These bands will be interpreted tentatively as combinations between fundamental internal vibrations and a low-lying mode of the order of 20 cm^{-1}—30 cm^{-1}. The justification for considering the low frequency mode as a libration fundamental will be given later but the interpretation will be made in accordance with this hypothesis.

The proposed model is shown schematically in figure 2 which assumes an ion on a site of symmetry C_3. The potential energy curve for libration is represented by the broken curve on the ground state vibrational level ($n=0$) and the first excited vibrational level ($n=1$). The potential energy is assumed to be independent of the vibrational state. In each of the three potential wells there are seven excited librational levels ($J=1-J=7$) shown. These levels are shown evenly spaced, i.e., anharmonicity corrections are neglected. Transitions between energy states are indicated by the vertical lines. No transitions are indicated between librational levels in the same vibrational state because the energies involved are too low to be of interest here.

At any given temperature transitions in all three potential wells will be similar since the three configurations of the ion are equivalent. With this in mind the three potential minima of figure 2 are utilized to demonstrate the effect of temperature on the resulting spectrum. At very low temperatures where all ions are in the ground state, only summation bands are possible as indicated in the left potential minimum. At intermediate temperatures, in addition to the summation bands shown at the lowest temperature some difference bands arise from the thermal excitation of some ions into the lower librational levels in the ground vibrational level. At still higher temperatures, in addition to the previous transitions, lower energy difference bands arise from thermal excitation to the higher librational levels in the ground vibrational state. Transitions to rotational levels which exist above the potential barriers are not indicated in figure 2. All possible transitions are not shown except at the lowest temperature.

a. Calcite Type Structures

Many calcite type crystals show spectra which are lacking in detail although there is evidence of unresolved absorption in the region of interest. However, the spectra for $NaNO_3$ shown in figure 3 are most informative. It will be noted that the diffuse absorption between approximately 900 cm^{-1} and 1050 cm^{-1} at room temperature (top spectrum), is resolved at liquid helium temperature (lower spectrum) into a series of step like bands located at 913 cm^{-1}, 938 cm^{-1}, 963 cm^{-1}, 991 cm^{-1}, 1021 cm^{-1}, 1058 cm^{-1}, and 1071 cm^{-1}. These bands have a nearly uniform separation varying from about 25 cm^{-1} to 37 cm^{-1}. In the low temperature spectrum other bands are also resolved and the resulting observations are tabulated in table 4.

TABLE 4. *Assignments for* $NaNO_3$ *at liquid helium temperature for libration combinations*

Frequency	Separation from fundamental	Frequency	Separation from fundamental	Frequency	Separation from fundamental	Assignment
cm^{-1}	cm^{-1}	cm^{-1}	cm^{-1}	cm^{-1}	cm^{-1}	
727 (ν_4)		838 (ν_2)		1068 (ν_1)		ν_0
747 vw	20	?		1103 w	32	$\nu_0 + L$
778 vw	51	?		?		$\nu_0 + 2L$
803 vw	75	913 m	75	1143 vw	75	$\nu_0 + 3L$
?		938 m	100	1176 sh	108	$\nu_0 + 4L$
?		963 m	125	1192 s	124	$\nu_0 + 5L$
880 ?	153	991 s	153	1228 w	160	$\nu_0 + 6L$
907 sh	180	1021 s	183	?		$\nu_0 + 7L$
945 sh	218	1058 s	220	?		$\nu_0 + 8L$
960 sh ?	233	1071 vs	233	1311 s	243	cutoff

Although they are diffuse and poorly defined at higher temperatures, the 913 cm^{-1} – 1071 cm^{-1} series of bands appear to shift by 3 cm^{-1} to 7 cm^{-1} between the temperature of liquid nitrogen and that of liquid helium with the larger shifts associated with the higher frequency bands. In the same temperature interval the fundamental ν_2 shows no detectable shift and ν_4 a shift of at most 1 cm^{-1}. From its temperature dependence and intensity it is believed that the 1071 cm^{-1} band represents the band limit or cutoff frequency of the series of bands starting at 913 cm^{-1} rather than the fundamental ν_1 which is inactive in all calcite structures. This series of bands may be interpreted as combinations of a mode of frequency 20 cm^{-1} – 30 cm^{-1} with ν_2. Similarly other bands in the structure may be interpreted as combinations of the same low frequency mode with ν_4 and the inactive ν_1 fundamental. The cutoff for the series of bands originating from ν_1 is believed to be the strong band at 1311 cm^{-1}. The cutoff for the series from ν_4 is not apparent but may tentatively be taken as a shoulder appearing at 960 cm^{-1}. The differences between the cutoff frequencies and the respective fundamentals for the three series of bands are 243 cm^{-1} (ν_1), 233 cm^{-1} (ν_2), and possibly 233 cm^{-1} (ν_4). The bands and assignments are given in table 4. These data as well as all other tabulated data refer only to observations at liquid helium temperature and include only libration-fundamental summation bands with ν_1, ν_2, and ν_4. Tabular data are recorded only for reproducible bands and where there is doubt about the existence of a band the recorded frequency is followed by a question mark. The following abbreviations are used in all tables: very weak—vw; weak—w; shoulder—sh; medium—m; strong—s; very strong—vs; broad—b. From the tabular data it will be noted that the correlation between the three series is reasonably good. The energy level spacing varies but the apparent variation is estimated to be of the same order of magnitude as the error associated with determining the positions of the weak, frequently broad, combination bands.

Although no combination bands of the 20 cm^{-1} —30 cm^{-1} mode with ν_3 are tabulated for any spec-

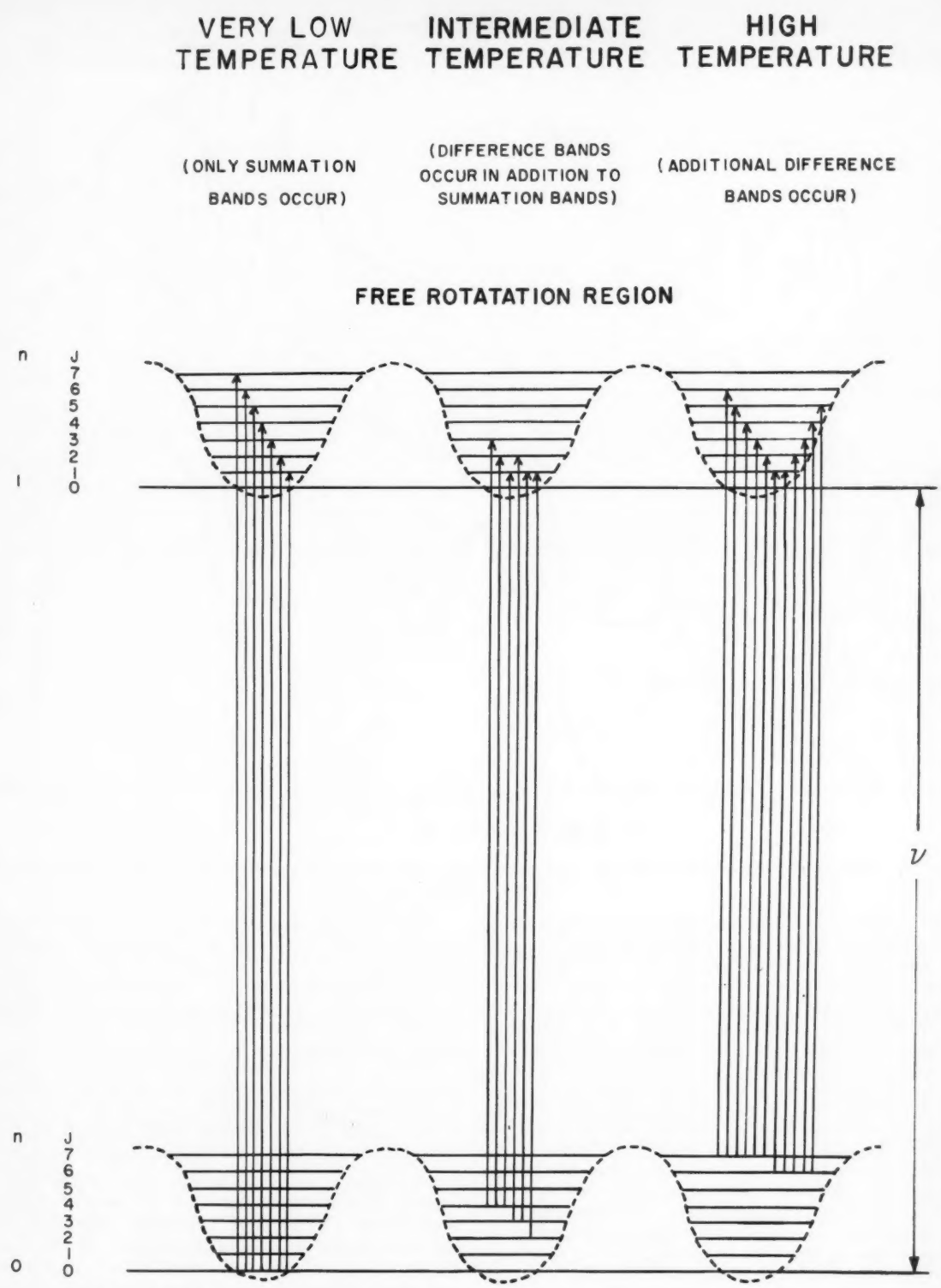
VERY LOW TEMPERATURE
INTERMEDIATE TEMPERATURE
HIGH TEMPERATURE
(ONLY SUMMATION BANDS OCCUR)
(DIFFERENCE BANDS OCCUR IN ADDITION TO SUMMATION BANDS)
(ADDITIONAL DIFFERENCE BANDS OCCUR)
FREE ROTATATION REGION
n J 7 6 5 4 3 2 1 0
1
n J 7 6 5 4 3 2 1 0
0
ν

FIGURE 2. *Energy level diagram for effect of temperature on libration-vibration combination bands.*

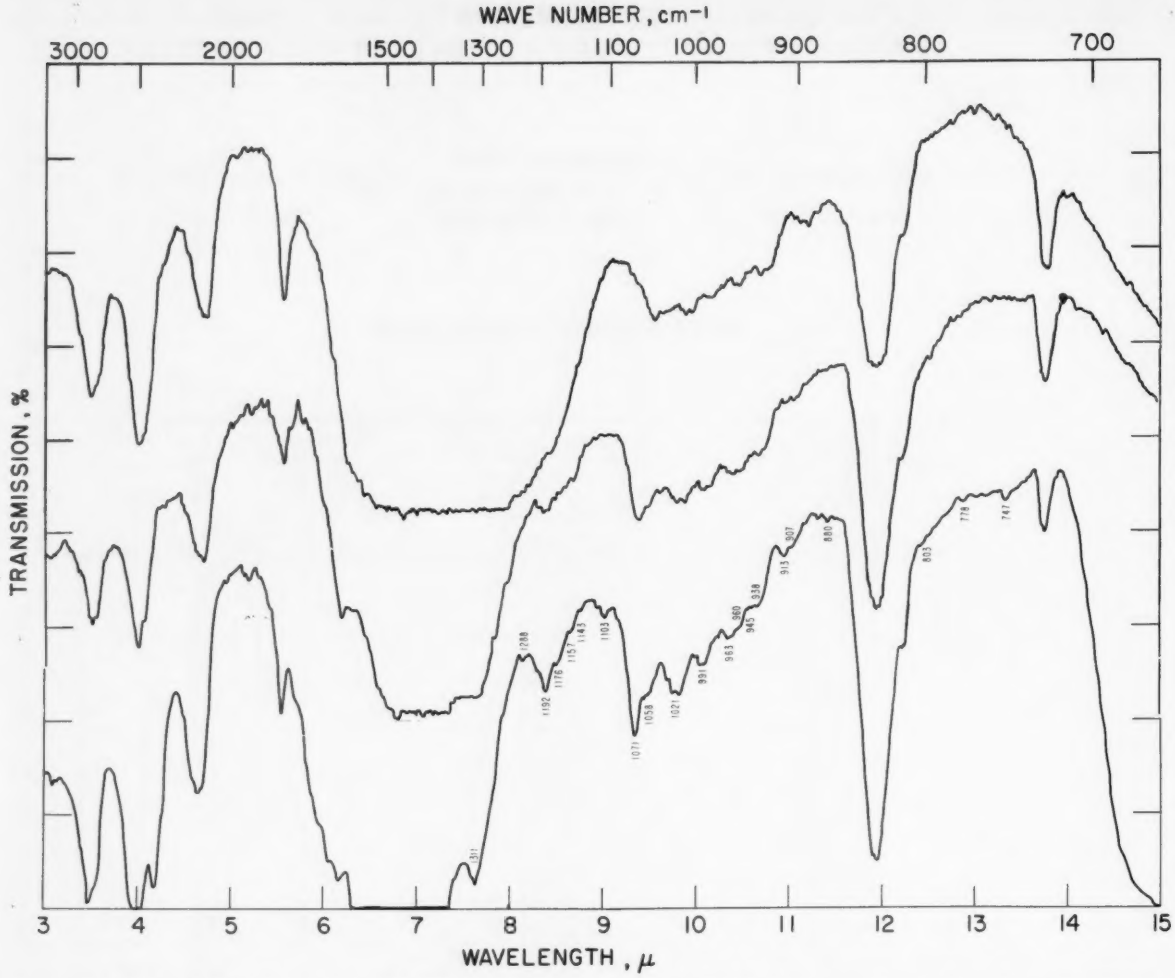

FIGURE 3. *Infrared absorption spectra of* $NaNO_3$ *at room temperature (top), liquid nitrogen temperature (center), and liquid helium temperature (bottom).*

trum many instances of summation bands originating from ν_3 have been observed. In this frequency region the instrumental dispersion is too low and the intensity of ν_3 is usually too great to permit location of combinations with any certainty. Evidence for the existence of combinations with ν_3 is indicated by figure 3 and all subsequent figures. The marked increase in transmission of all crystals on the low frequency side of ν_3 as the temperature is lowered may be attributed to the elimination of difference bands between ν_3 and a low frequency mode at lower temperatures. A corresponding change does not occur on the high frequency side of ν_3, where the summation bands would be expected to become stronger at lower temperatures. Furthermore, the rather abrupt increase in transmission observed in most spectra on the high frequency side of ν_3 occurs at a frequency which is of the correct order of magnitude for the cutoff for a series of combination bands originating from the fundamental ν_3.

Although the assignments given in table 4 account for all bands it cannot be considered completely satisfactory. Several expected bands are missing and the band at 1192 cm^{-1} is unexpectedly strong. A similar situation will be encountered in all other spectra. All assignments, therefore, are made with some qualifications.

Spectra at room temperature and liquid helium temperature are given for the other calcite structures $MgCO_3$, $CaCO_3$, $FeCO_3$, and $MnCO_3$ in figures 4, 5, 6, and 7 respectively with tabular data for $CaCO_3$ listed in table 5. Satisfactory resolution of bands was not obtained on any specimen of $MgCO_3$ despite several experiments on crystals of differing thicknesses. The strong band near 1250 cm^{-1} may represent the ν_1 cutoff and that near 1120 cm^{-1} the ν_2 cutoff. A low frequency mode of about 25 cm^{-1} and a cutoff frequency of approximately 230 cm^{-1} are indicated on the basis of the several experiments.

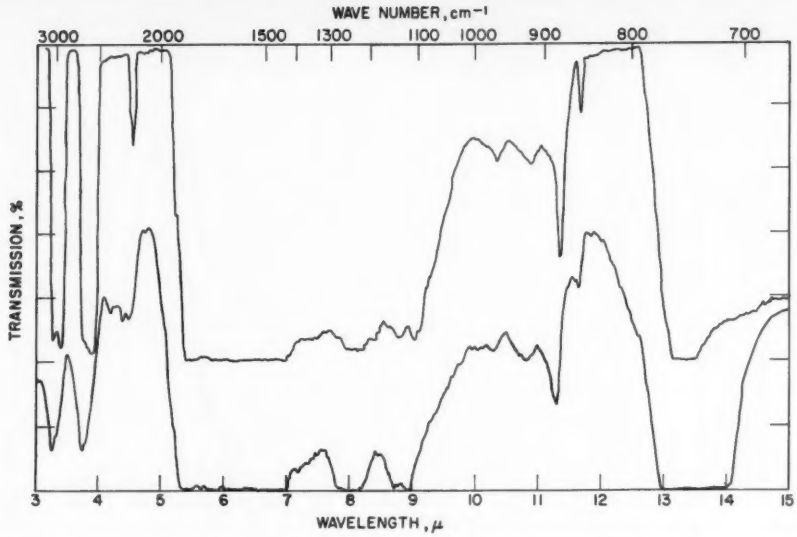

FIGURE 4. *Infrared absorption spectra of* $MgCO_3$ *at room temperature (top) and liquid helium temperature (bottom).*

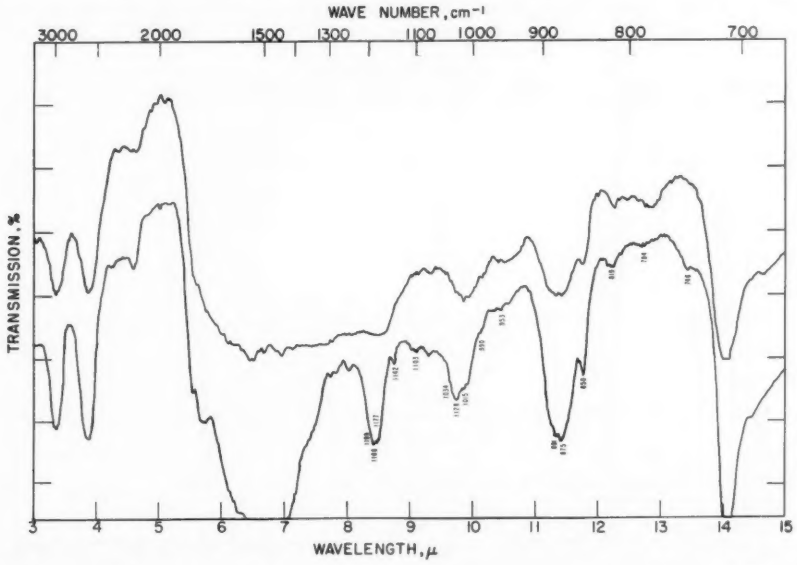

FIGURE 5. *Infrared absorption spectra of* $CaCO_3$ *(calcite) at room temperature (top) and liquid helium temperature (bottom).*

TABLE 5. *Assignments for* $CaCO_3$ *at liquid helium temperature for libration combinations*

Frequency	Separation from fundamental	Frequency	Separation from fundamental	Frequency	Separation from fundamental	Assignment
cm^{-1}	cm^{-1}	cm^{-1}	cm^{-1}	cm^{-1}	cm^{-1}	
712 (ν_4)		881 (ν_2)		1070 (ν_1)		ν_0
746 m	34	?	?	1103 w	33	ν_0+L
784 w	72	953 w	72	1142 m	72	ν_0+2L
819 m	107	990 sh	109	1177 s	107	ν_0+3L
850? s	138	1015 s	134	1186 s	116	ν_0+4L
Cutoff masked by ν_2	?	1028 s	147	1199 sh	132	ν_0+5L
		1034?	153	1220	150	cutoff

Tabular data for $CaCO_3$ are given in table 5. A libration frequency of about 35 cm^{-1} and an average cutoff frequency of about 150 cm^{-1} are indicated. Three weak bands at 1075 cm^{-1}, 1245 cm^{-1}, and 1283 cm^{-1} are not accounted for by the assignments. Although the band at 1075 cm^{-1} might be taken as the inactive ν_1 fundamental this is not believed to be the case. Raman spectroscopy has located ν_1 near 1086 cm^{-1} and this fundamental is invariably observed as a sharp band in the infrared spectrum when it is active. The band at 1075 cm^{-1} however, is quite broad.

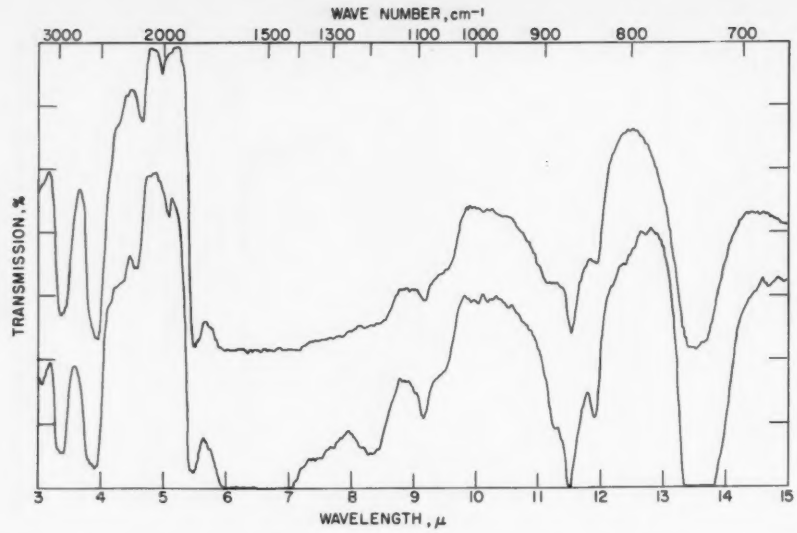

FIGURE 6. *Infrared absorption spectra of* $FeCO_3$ *at room temperature (top) and liquid helium temperature (bottom).*

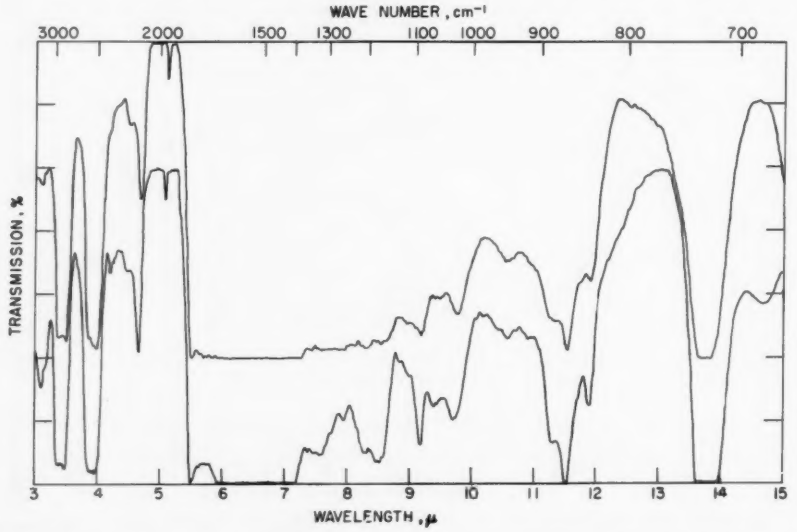

FIGURE 7. *Infrared absorption spectra of* $MnCO_3$ *at room temperature (top) and liquid helium temperature (bottom).*

No data are tabulated for $FeCO_3$ and $MnCO_3$ because of the questionable purity of the specimens. As shown by the spectra both materials exhibit the same general absorption pattern as the other calcite structures. Cutoff frequencies are estimated to be 150 cm^{-1} for $FeCO_3$ and 160 cm^{-1} for $MnCO_3$ on the basis of tentative assignments. The $MnCO_3$ spectrum which shows much fine structure can be interpreted with a single libration frequency of 15 cm^{-1} or with two separate frequencies of 30 cm^{-1}.

b. Aragonite Type Structures

Spectra for two temperatures are given for $SrCO_3$ in figure 8 and the tabular frequencies observed in table 6. Spectra at room temperature and liquid He temperature and the tabulated frequencies are given in figures 9, 10, 11, and 12, and tables 7, 8, 9, and 10 for $CaCO_3$ (aragonite), $BaCO_3$, $PbCO_3$, and KNO_3 respectively. Additional expanded spectra at liquid helium temperatures covering the range from about 1800 cm^{-1} to 770 cm^{-1} for $SrCO_3$ and $CaCO_3$ (aragonite) are given in figures 13 and 14.

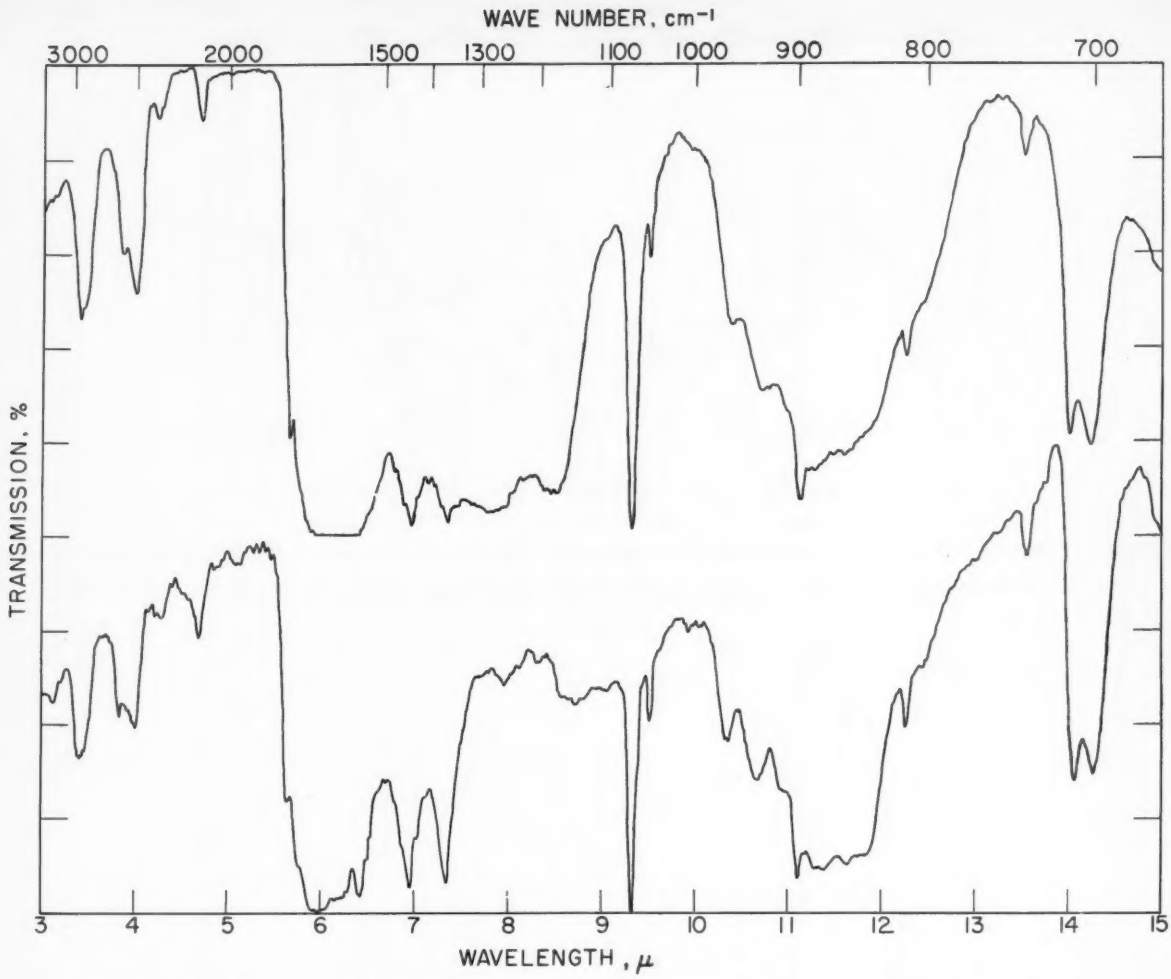

FIGURE 8. *Infrared absorption spectra of* $SrCO_3$ *at room temperature (top) and liquid helium temperature (bottom).*

TABLE 6. *Observed frequencies for* $SrCO_3$ *at liquid helium temperature*

Frequency	Separation from fundamental	Frequency	Separation from fundamental	Frequency	Separation from fundamental
cm^{-1}	cm^{-1}	cm^{-1}	cm^{-1}	cm^{-1}	cm^{-1}
701, 711 ν_4		863 ν_2		1072 ν_1	
				1108 vw	36
737 ν_4?	36?	908 vw	45	1147 vb	75
803 wb	92?	913 mb	50	1165 vb	93
816 s	105?	937 mb	73	1200 w	128
861 sb	150?	967 sb	104	1230 w	158
879 sb	168?	995 vw	132	1256? w	184
900 s	189?	1008 vw	145	1261? w	189
		1042 w sh	179		
		1050 m	187		

TABLE 7. *Observed frequencies for* $CaCO_3$ *(aragonite) at liquid helium temperature*

Frequency	Separation from fundamental	Frequency	Separation from fundamental	Frequency	Separation from fundamental
cm^{-1}	cm^{-1}	cm^{-1}	cm^{-1}	cm^{-1}	cm^{-1}
701, 717 ν_4		866 ν_2		1086 ν_1	
—		—		1102 s	16
741 mb	24?	—		1110 sh	24
—		—		1121 m	35
—		—		1133 msh	47
775 w	58?	924 w	58	1144 s	58
—		—		1148 sh	62
—		—		1155 wsh	69
809? sh	92?	—		1176 sh	90
—		969 w	103	1182 w	96
—		983 w	117	1201 m	115
839 sb	122?	989 w	123	—	
846? sb	129?	996 sh	130	1215 m	129
—		1018 w sh	142	—	
—		—		1245 w	159
883 sb	166?	1034 b	168	1254 w	168
903 b	184?	1055 wb	189	1278 sh	192
912 s	195?	1061 m	195	1291 mb	205

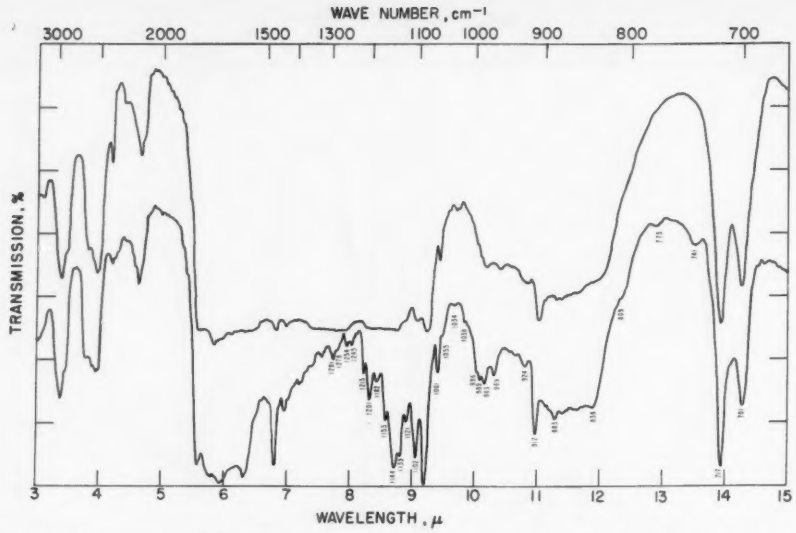

FIGURE 9. *Infrared absorption spectra of* $CaCO_3$ *(aragonite) at room temperature (top) and liquid helium temperature (bottom).*

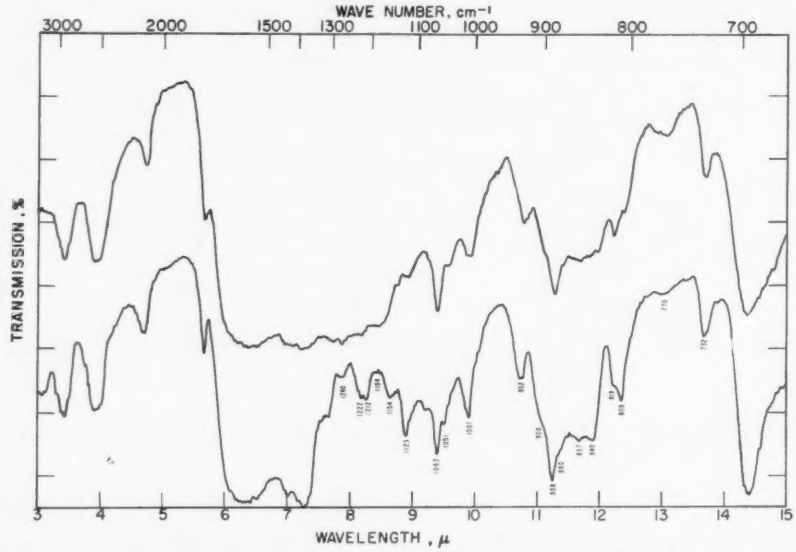

FIGURE 10. *Infrared absorption spectra of* $BaCO_3$ *at room temperature (top) and liquid helium temperature (bottom).*

TABLE 8. *Observed frequencies for* $BaCO_3$ *at liquid helium temperature*

Frequency	Separation from fundamental	Frequency	Separation from fundamental	Frequency	Separation from fundamental
cm^{-1}	cm^{-1}	cm^{-1}	cm^{-1}	cm^{-1}	cm^{-1}
694 ν_4		857 ν_2		1062 ν_1	
732 m (ν_4?)	38	900 m	43	1075 ?	13
770 vw	76	932 m	75	1123 m	61
808 m	114	—		1154 m	92
818 sh	124	—		1184 vw	122
840 s	156	1007 m	150	1212 m	150
880 sh	186	1038 w sh	181	1222 m	160
888 s	194	1051	194	—	

TABLE 9. *Observed frequencies for* $PbCO_3$ *at liquid helium temperature*

Frequency	Separation from fundamental	Frequency	Separation from fundamental	Frequency	Separation from fundamental
cm^{-1}	cm^{-1}	cm^{-1}	cm^{-1}	cm^{-1}	cm^{-1}
684 ν_4		842 ν_2		1057 ν_1	
727 m ν_4?	42	896 w sh	54	1082 w	25
734 m ν_4?	50	911 w	69	1101 sh	43
—		—		1118 s	61
768 vw	84	925 w sh	83	1143 sh	86
788 mb	104	938 w sh	96	1161 w	104
797 mb	113	958 w sh	116	—	
809 wb	125	977 w sh	135	1187 w	130
818 vw	134	—		—	
827 m	143	996 vw	154	—	
854 sb	170	1011 vw	169	1228 m	171
—		1022 wb	180	1234 m	177
877 s	193	1036?	194	1257 m sh	200 cutoff?

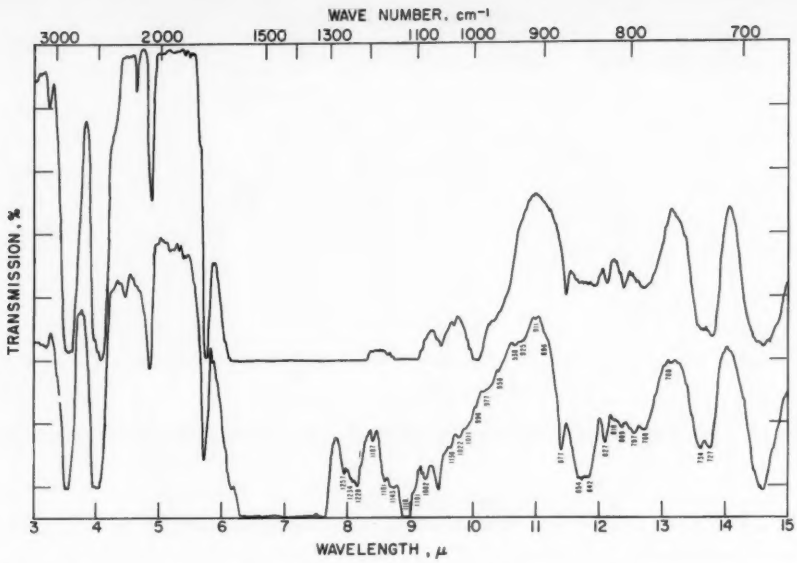

FIGURE 11. *Infrared absorption spectra of* $PbCO_3$ *at room temperature (top) and liquid helium temperature (bottom).*

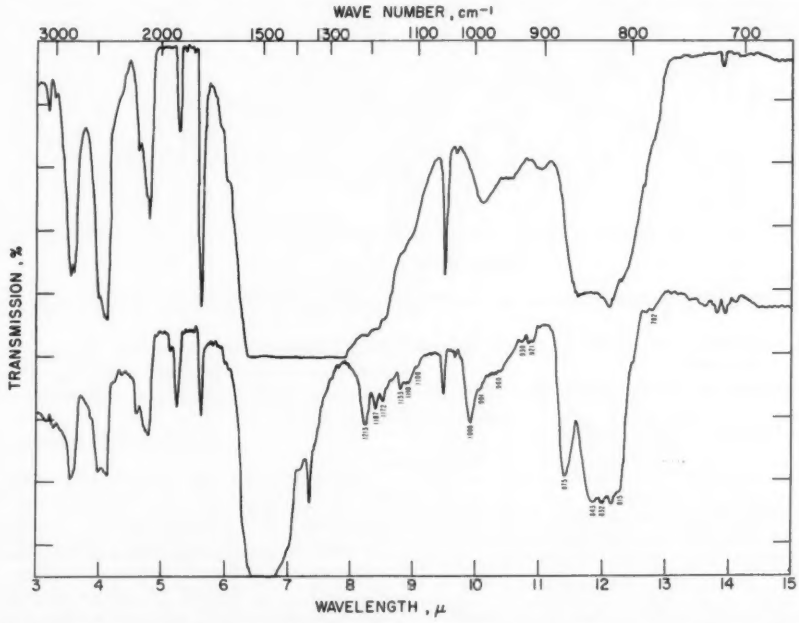

FIGURE 12. *Infrared absorption spectra of* KNO_3 *at room temperature (top) and liquid helium temperature (bottom).*

Only general observations are given for these spectra. Attempts to analyze the highly complex structure observed in figures 13 and 14 have met with only indifferent success. In part, this is probably the result of the more complex internal fundamental bands observed in these structures which were discussed earlier. At the very least this would produce many overlapping band systems. In part the complexity may arise from further splitting of ν_2 from isotope effects first noted by Decius [15] in the aragonites. Finally, there are strong indications that at least two libration frequencies may be involved in these spectra to produce still greater overlapping.

That combination modes are involved is clearly shown by comparing the normal and low temperature spectra. Elimination of the difference modes with ν_1 is clearly seen in figures 9, 10, and 11 so that there is little doubt that a liberation frequency of approximately 30 cm^{-1} is present. Attempts have been

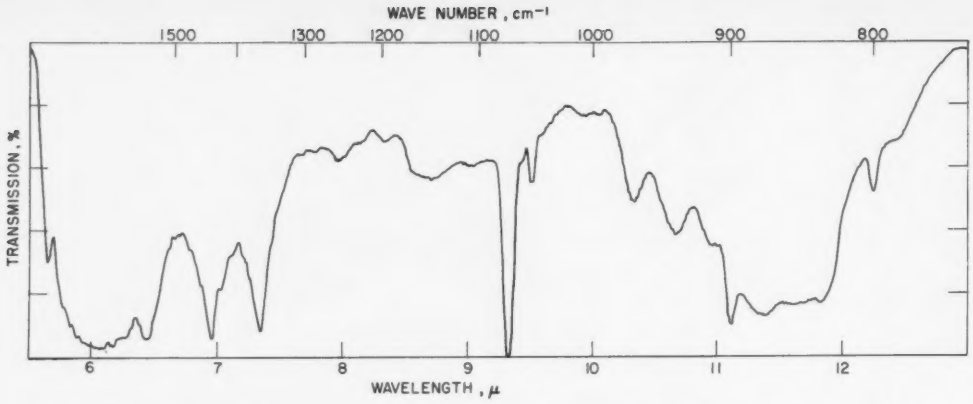

FIGURE 13. *Infrared absorption spectrum of* $SrCO_3$ *at liquid helium temperature (expanded scale).*

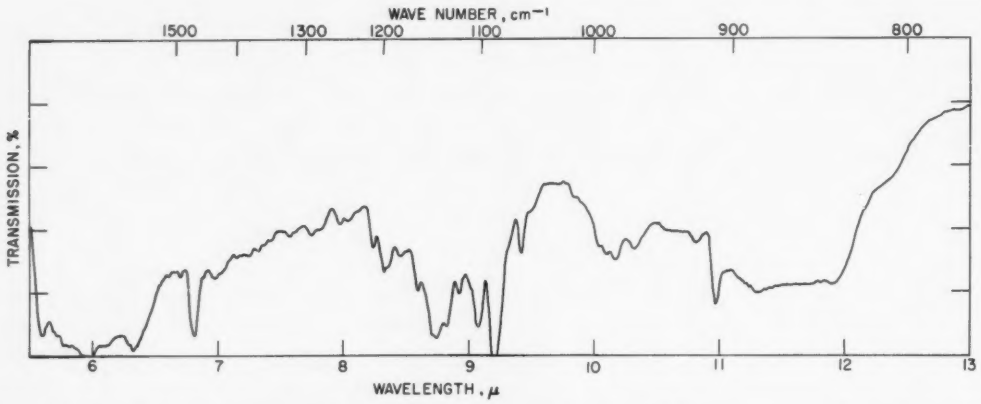

FIGURE 14. *Infrared absorption spectrum of* $CaCO_3$ *(aragonite) at liquid helium temperature (expanded scale).*

TABLE 10. *Observed frequencies for* KNO_3 *at liquid helium temperature*

Frequency	Separation from fundamental	Frequency	Separation from fundamental	Frequency	Separation from fundamental
cm^{-1}	cm^{-1}	cm^{-1}	cm^{-1}	cm^{-1}	cm^{-1}
714 ν_4		827 ν_2		1051 ν_1	
—		—		1100 wb	49
782	68	—		1119 b	68
—		921? b	94	1133 mb	82
815 s	101	930 vw	103	—	
832 b	118	—		1172 m	121
843 b	129	960 wb	133	1187 m	136
875 s	161	991 w sh	164	1213 s	162
		1008 s	181		

made to correlate bands arising from the various fundamentals in the tabular data. It appears that correlations exist despite the failure to analyze the data.

One outstanding characteristic of the carbonate aragonites is to be found in the very broad, intense band found in the ν_2 region. This band completely obscures the ordinarily strong ν_2 band found in thin polycrystalline films of these materials [77]. The sharp strong band on the high frequency edge of this absorption complex does not correspond to the usual out-of-plane bending frequency, but may represent the cutoff for a series of liberation modes with ν_4.

c. Cubic Type Structures

The spectra of the cubic nitrates show many bands falling into a regular series that may be assigned to combinations between a harmonic liberation mode and the fundamentals ν_1, ν_2, and ν_4. Spectra at three temperatures are shown for $Pb(NO_3)_2$ in figure 15 while similar spectra at two temperatures are given in figures 16 and 17 for $Ba(NO_3)_2$ and $Sr(NO_3)_2$ respectively. Assignments at liquid helium temperature are tabulated in tables 11, 12, and 13. In the spectra it is noted that bands falling between 850 cm^{-1} and 1250^{-1} have relatively large frequency shifts with temperature, while the fundamentals ν_2 and ν_4 appear to be unaffected by the same temperature change. These bands may be attributed to the combinations of a low lying librational mode with the fundamentals, with the librational mode being relatively temperature dependent through the effect of expansivity on volume.

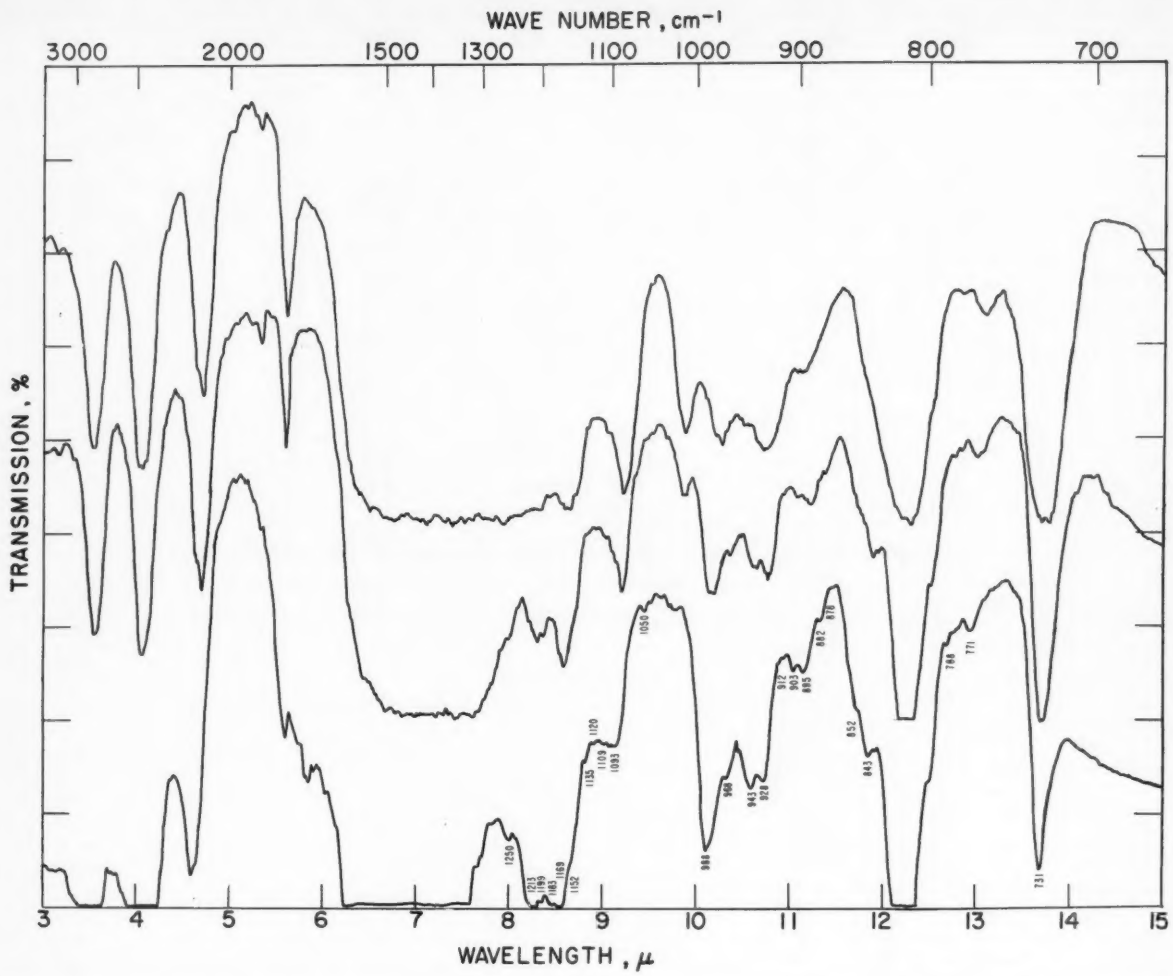

FIGURE 15. *Infrared absorption spectra of* $Pb(NO_3)_2$ *at room temperature (top), liquid nitrogen temperature (center), and liquid helium temperature (bottom).*

TABLE 11. *Assignments for* $Pb(NO_3)_2$ *at liquid helium temperature for libration combinations*

Frequency	Separation from fundamental	Frequency	Separation from fundamental	Frequency	Separation from fundamental	Assignment
cm^{-1}	cm^{-1}	cm^{-1}	cm^{-1}	cm^{-1}	cm^{-1}	
731 ν_4		817 ν_2		1058 ν_1		ν_0
—		838 ?	21	—		ν_0+L
771	40	852 sh	35	1093 s	35	ν_0+2L
788	57	—		≈1109 vw	51	ν_0+3L
?		882 m	65	1120? vw	62	ν_0+4L
?		—		1135 sh	77	ν_0+5L
?		912 vw	95	1152 sh	94	ν_0+6L
843	113	928 s	111	1169 s	111	ν_0+7L
858 sh	127	943 s	126	1183 sh	125	ν_0+8L
878 sh	147	968 s	146	1199 sh	141	ν_0+9L
895	164	—		1213 vs	153	ν_0+10L
903	172	988 vs	171	1220	162	cutoff

TABLE 12. *Assignments for* $Ba(NO_3)_2$ *at liquid helium temperature for libration combinations*

Frequency	Separation from fundamental	Frequency	Separation from fundamental	Frequency	Separation from fundamental	Assignment
cm^{-1}	cm^{-1}	cm^{-1}	cm^{-1}	cm^{-1}	cm^{-1}	
722 ν_4		813 ν_2		1052 ν_1		ν_0
—		—		—		ν_0+L
765	43	—		1086 vs	34	ν_0+2L
785 b	63	866 vw	53	1105 m sh	53	ν_0+3L
—		—		1125 s	73	ν_0+4L
—		—		1139 s	87	ν_0+5L
—		—		1156 s	104	ν_0+6L
838 sh	116	931 m	118	1172 w sh	120	ν_0+7L
857 w	135	949 m	136	1188 sh	136	ν_0+8L
876 w	154	969 m	156	1209 sh	157	ν_0+9L
889 sh	167	982 sh	169	1220 ?	168	ν_0+10L
898 s	176	993 s	180	1231 s	179	ν_0+11L
?		?		?		ν_0+12L
913 m	191	1004	191	1245	193	cutoff

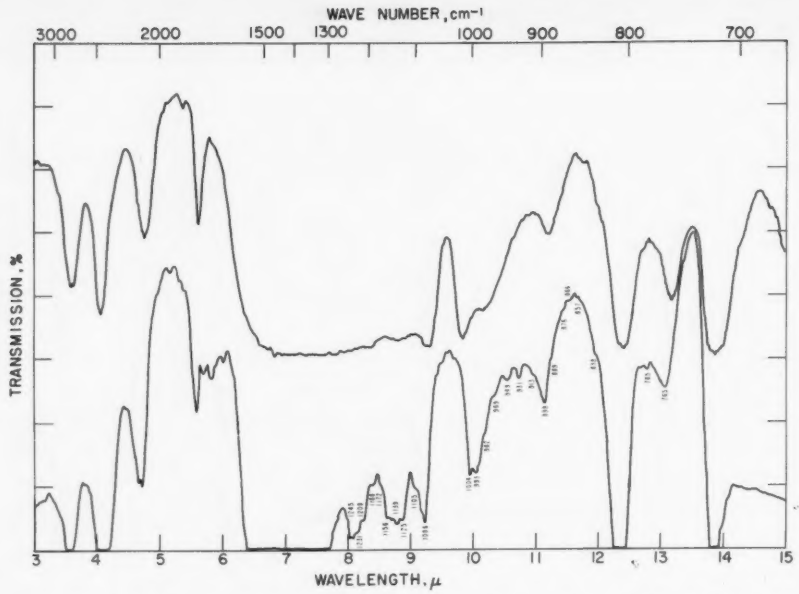

FIGURE 16. *Infrared absorption spectra of* $Ba(NO_3)_2$ *at room temperature (top) and liquid helium temperature (bottom).*

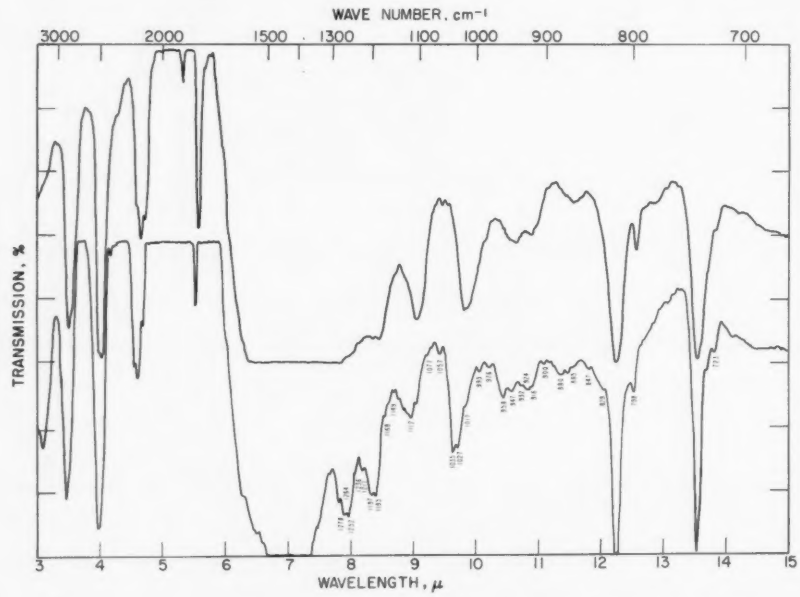

FIGURE 17. *Infrared absorption spectra of* $Sr(NO_3)_2$ *at room temperature (top) and liquid helium temperature (bottom).*

Inspection of the tables shows a rather systematic series of bands arising from each of the fundamentals. In the region between ν_2 and the cutoff for the series arising from ν_4 the band structure is highly complex. Assignments in this region are not unequivocal as may be seen from the vacancies in the tables. The combination bands are neither sharp nor strong so that errors in positions may easily amount to a few cm^{-1}. With this uncertainty the variation in spacing appears to be of the order of the errors in locating the bands.

The behavior of the two bands located symmetrically on either side of the inactive or very weak ν_1 frequency (circa 1050 cm^{-1}) provide a convincing argument for the assignments given. These bands are believed to arise from sum and difference tones of the libration and the symmetric stretch. In the room temperature spectra these bands are very

TABLE 13. *Assignments for $Sr(NO_3)_2$ at liquid helium temperature for libration combinations*

Frequency	Separation from fundamental	Frequency	Separation from fundamental	Frequency	Separation from fundamental	Assignment
cm^{-1}	cm^{-1}	cm^{-1}	cm^{-1}	cm^{-1}	cm^{-1}	
738 (ν_4)		815 ν_2		1057 ν_1		ν_0
754 ?	16	829 sh	14	1077 sh	20	ν_0+L
—		?		—		ν_0+2L
798 s	60	?		1112 s b	55	ν_0+3L
—		?		—		ν_0+4L
829 sh	91	?		1149 vw	92	ν_0+5L
847 w	109	924 m	109	1168 w sh	111	ν_0+6L
865 w	127	?		1185 s	128	ν_0+7L
880 m	142	?		1197 s	140	ν_0+8L
900 ? vw	162	976 w	161	1217 m	160	ν_0+9L
916 w sh	178	993 m	178	1236 sh	179	ν_0+10L
932 sh	194	1012 sh	197	1252 s	195	ν_0+11L
947 m	209	1027 sh	212	1264 s	209	ν_0+12L
958 s	220	1035 vs	220	1278 m	221	cutoff

prominent features of the spectra. In $Sr(NO_3)_2$ the bands appear to be located at 1103 cm^{-1} and 1029 cm^{-1} and the difference between these values appears to be four times the librational frequency giving a libration mode of 19 cm^{-1}. In $Pb(NO_3)_2$ the bands are at 1086 cm^{-1} and 1012 cm^{-1} giving L = 18 cm^{-1}, while in $Ba(NO_3)_2$ the corresponding values are 1074 cm^{-1}, 1015 cm^{-1} with L = 15 cm^{-1}. These values of the librational frequency may be lower than the corresponding values given in the tables for liquid helium temperature, but the value of the libration frequency is temperature dependent as shown by the temperature dependence of the libration bands. From figure 15 it will be noted that as the temperature is lowered the summation band located at 1086 cm^{-1} at room temperature in $Pb(NO_3)_2$ shifts to about 1088 cm^{-1} at liquid nitrogen temperature and to approximately 1093 cm^{-1} at liquid helium temperature. Simultaneously the difference band located at 1012 cm^{-1} which is very strong at room temperature is reduced to about one-half of this intensity at liquid nitrogen temperature and to a very weak, questionable band at liquid helium temperature. The intensity behavior corroborates the interpretation as a difference band and the low temperature required for its removal is conclusive evidence for a low frequency transition. As mentioned earlier this difference band constitutes a thermometer in the spectrum.

The effect of temperature on the cutoff frequency for combinations with ν_2 observed in the same figure appears to result in an increase of the cutoff from 975 cm^{-1} at room temperature, to 985 cm^{-1} at liquid nitrogen temperature and to about 988 cm^{-1} at liquid helium temperature. Simultaneously the cutoff appears to increase in intensity and become noticeably sharper. The effect of temperature on the intensity will be discussed later.

An analagous behavior is exhibited by $Sr(NO_3)_2$ and $Ba(NO_3)_2$. It should be noted that the strong 1015 cm^{-1} band in the room temperature spectrum of $Ba(NO_3)_2$ does not represent the cutoff for the ν_2 series. The 1015 cm^{-1} band is the ν_1 difference mode and is eliminated on cooling. The ν_2 series cutoff appears to be represented by the strong shoulder near 980 cm^{-1} which shifts to 1004 cm^{-1} on cooling. In $Sr(NO_3)_2$ the difference band located near 1015 cm^{-1} at room temperature appears to be obliterated by the ν_2 cutoff which shifts from an unknown position at room temperature to about 1032 cm^{-1} at liquid nitrogen temperature and to approximately 1035 cm^{-1} at liquid helium temperature.

As in all other spectra the effect of cooling on ν_3 is to produce a marked increase in transmission on the low frequency side of ν_3 with an absence of a similar effect on the high frequency side. This is in accord with the elimination of the difference modes ν_3-nL on cooling with no corresponding elimination of the summation bands. The ν_3 cutoff is estimated to be of the correct order of magnitude if it is taken at the frequency at which the specimens show transmission on the high frequency side of ν_3.

d. Miscellaneous Structure Types

Data are given here for $TlNO_3$, $AgNO_3$, $CsNO_3$, and $RbNO_3$. Spectra are given at three temperatures for $TlNO_3$ in figure 18. Spectra for two temperatures are given in figures 19, 20, and 21 for $AgNO_3$, $CsNO_3$, and $RbNO_3$, respectively. The corresponding frequencies are given in tables 14, 15, 16, and 17. In the experiments using $AgNO_3$ difficulties were encountered because of the reaction between the copper bar and $AgNO_3$. Successful runs were obtained by cementing the $AgNO_3$ crystal to a silver strip which was attached to the copper bar. The thermal path for $AgNO_3$ was longer and more doubtful than for any other specimen. However, comparison of the two spectra for the $AgNO_3$ show that considerable cooling was effected.

These spectra contain a wealth of fine structure of which only a portion appears to be explained by the present analysis. There are indications that at least two low frequency libration modes are coupling with the fundamentals giving rise to two overlapping series of bands with two cutoff values. As shown in table 14, half of the bands for $TlNO_3$ can be assigned with a 25 cm^{-1} libration mode but there are also at least nine unassigned bands.

TABLE 14. *Assignments for $TlNO_3$ at liquid helium temperature for libration combinations*

Frequency	Separation from fundamental	Frequency	Separation from fundamental	Frequency	Separation from fundamental	Assignment
cm^{-1}	cm^{-1}	cm^{-1}	cm^{-1}	cm^{-1}	cm^{-1}	
715 ν_4		828 ν_2		1044 ν_1		ν_0
740 s	25	860 sh	32	1068 sh	24	ν_0+L
—		—		1090 m	46	?
768 sh	53	880 wb	52	1096 m	52	ν_0+2L
—		—		1101 sh	57	?
791 m	76	905 w	77	1115 w	71	ν_0+3L
—		913 m	85	1127 vw	83	?
—		—		1138 w	94	?
—		931 w	103	1147 s	103	ν_0+4L
—		—		1150 vs	106	?
—		—		1160 sh	116	?
—		—		1168 sh	124	?
—		956 m	128	1175 s	131	ν_0+5L
850 sh	145	975 s	147	1193 b sh	149	?
885 w	160	989 m	161	1207 m	163	?
—		1003 s	175	1224 m	180	ν_0+7L
—		1023 m	195	—		?
922 w	207	1030	202	1246 w	202	ν_0+8L
943 sh	228	1054 vw	226	1280? sb	236	ν_0+9L
975 s	260	1080 m	252	1294? b	250	cutoff

TABLE 15. *Observed frequencies in $AgNO_3$ at liquid helium temperature*

Frequency	Separation from fundamental	Frequency	Separation from fundamental	Frequency	Separation from fundamental
cm^{-1}	cm^{-1}	cm^{-1}	cm^{-1}	cm^{-1}	cm^{-1}
—		806 ν_2		1046 ν_1	
711 ν_4		835	29	1078 s	32
735 ν_4		—		1086	40
—		—		1093	47
—		862 sh	56	1103 s	57
—		868	62	—	
—		—		1122 m	76
—		897	91	1136 m	90
—		909	103	1150 m	104
—		929	123	1164 sh	118
—		—		1179 sh	133
—		948	143	1195 m	149
—		—		1214 w	168
—		987	181	1230 sh	184
—		1000	196	1242 s	196
—		1017	211	—	
960	225	1025	219	Obscured?	cutoff?

TABLE 16. *Assignments for $CsNO_3$ at liquid helium temperature for libration combinations*

Frequency	Separation from fundamental	Frequency	Separation from fundamental	Frequency	Separation from fundamental	Assignment
cm^{-1}	cm^{-1}	cm^{-1}	cm^{-1}	cm^{-1}	cm^{-1}	
719 ν_4		833 ν_2		1053 ν_1		ν_0
—		860	27	—		ν_0+L
764 mb	45	880 wb	47	1103 s	50	ν_0+2L
797 vw	78	900 w	67	1124 s	71	ν_0+3L
?		933 m	100	1152 m	99	ν_0+4L
?		956 s sh	123	1178 sh	125	ν_0+5L
?		980 vs	147	1185 s	132	?
≈880 b	163	994 vs	161	1213 vs	160	cutoff

TABLE 17. *Assignments for $RbNO_3$ at liquid helium temperature for libration combinations*

Frequency	Separation from fundamental	Frequency	Separation from fundamental	Frequency	Separation from fundamental	Assignment
cm^{-1}	cm^{-1}	cm^{-1}	cm^{-1}	cm^{-1}	cm^{-1}	
726 ν_4		844 ν_2		1061 ν_1		ν_0
748	22	—		1084 vw	24	ν_0+L_1
780	54	—		1111 s	51	ν_0+2L_1
793 w	67	—		1126 s	66	ν_0+2L_2
—		928 m b	76	1140 s	80	ν_0+3L_1
—		—		1153 m	93	ν_0+3L_2
—		950 sh	106	1170 vw	110	ν_0+4L_1
—		964 m	120	1186 w	126	ν_0+4L_2
866 sh	140	988 s	144	1206 s	146	cutoff L_1
890 br	164	1005 s	161	—		ν_0+5L_2
≈901 b	175	1019 s	175	1232 s	172	cutoff L_2

The tabular data for $AgNO_3$ are not assigned. The complexity of the spectrum may be less than that of $TlNO_3$ and it seems that at least two librational modes are required. One peculiarity of the spectrum is the frequent appearance of triplet bands. One libration mode of 30 cm^{-1} with a cutoff of approximately 220 cm^{-1} appears reasonably certain.

Although the spectra of $CsNO_3$ and $RbNO_3$ appear to be similar, a somewhat different assignment can be given. A single libration mode of 30 cm^{-1} and a cutoff of 160 cm^{-1} is given for $CsNO_3$. A similar assignment for $RbNO_3$ is not obvious. Instead two modes one at 25 cm^{-1} and the other 30 cm^{-1} with barriers of 146 cm^{-1} and 175 cm^{-1} are indicated. However, it would appear that the 1153 cm^{-1} band might represent a cutoff not indicated by the assignment. Raman studies [36] show two frequency shifts of 109 cm^{-1} and 147 cm^{-1} for $RbNO_3$ both of which are observed in the spectra here. The 147 cm^{-1} band appears to correspond with one of the cutoff values.

e. Discussion of Raman and Infrared Assignments

The preceding analyses and assignments of the infrared spectra have been made with a minimum of reference to the considerable literature on the Raman spectra of the carbonates and nitrates (see Introduction). It may be noted that, so far as can be ascertained, the Raman shifts have never been assigned to a series of bands arising from librational motion of the anion about the trigonal axis. Some Raman bands have been assigned to libration perpendicular to this axis. Couture [10] pointed out that the fundamental libration used here should be inactive or at most weakly active in the Raman spectrum. However, analysis shows that the *combination* bands should be active in the infrared. It may be noted that no shift as low as 30 cm^{-1} has been reported in the Raman spectra of these materials but Krishnamurti [42] has recently reported that the few shifts obtained by routine Raman studies appear to consist of bands covering a wide frequency range when high resolution and long exposures are employed. He attributed the fine structure to superlattice vibrations.

In the present data the separations between the fundamental and the summation bands can be identified in part with a series of Raman shifts reported for the material of interest. The Raman assignments for these shifts involve individual translational and librational lattice modes. The evidence in favor of the librational assignment as opposed to the translational assignment and vice versa will be summarized here.

The effect of temperature on sum and difference bands of the fundamental ν_1 observed in many spectra represents good evidence that a very low lying frequency of the order 20 cm^{-1}–30 cm^{-1} is involved. The additional finding that this frequency represents the separation of a large number of bands in almost all spectra studied is considered to be significant. Furthermore, all structures, both carbonates and nitrates, yield a spectrum in which a frequency difference of the order of 20 cm^{-1}–30 cm^{-1} appears independent of the cation. The materials studied here contain one common factor—a planar anion having trigonal symmetry—and it appears that the recurring frequency difference should be attributed to this source. A librational motion of these anions all of which have essentially the same principal moments of inertia would be expected to occur at a frequency determined largely by the interionic potential forces. There is evidence that the anions are closely packed in these crystals [45, 77] and the interionic forces would be of the same general order of magnitude. It appears reasonable to conclude that the low frequency fundamental

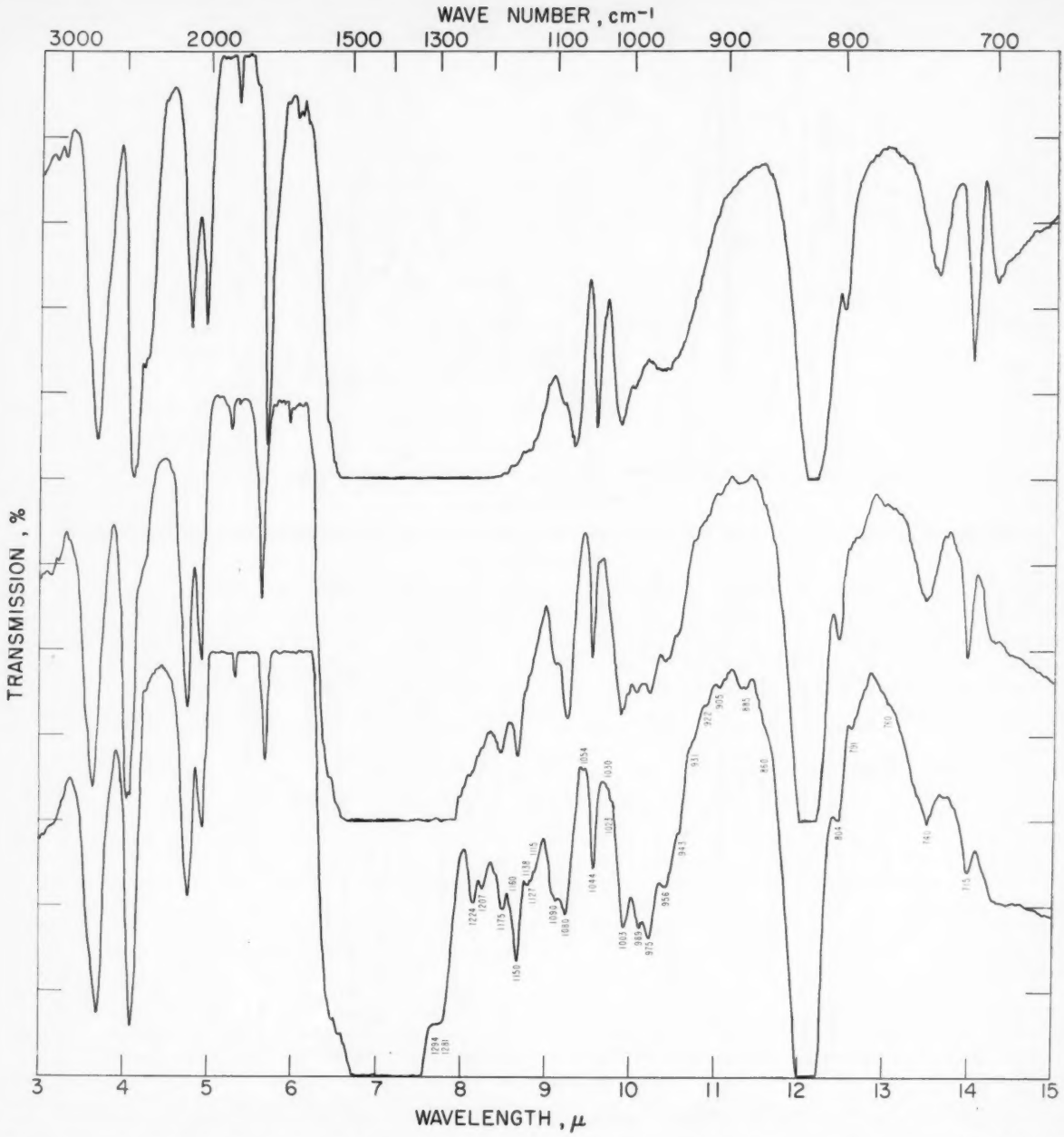

FIGURE 18. *Infrared absorption spectra of* $TlNO_3$ *at room temperature (top), liquid nitrogen temperature (center), and liquid helium temperature (bottom).*

arises from libration of the anions. The nature of the libration is not apparent and, as noted in the previous discussion, more than one frequency appears to be involved in some instances. However, based on the X-ray and neutron diffraction data previously cited which indicate libration about the trigonal axis, it is concluded that the libration responsible for the 20 cm^{-1}–30 cm^{-1} band spacing is a torsional oscillation about the trigonal axis.

Conversely, the bands observed here could be assigned to a large number of separate translational lattice modes in combination with the fundamentals. However, it seems unlikely that individual translational modes would have frequencies such as to yield a series of bands with uniform spacing. It is even more unlikely that similar series would be produced by such a variety of structures and cations. Therefore, the explanation that individual transla-

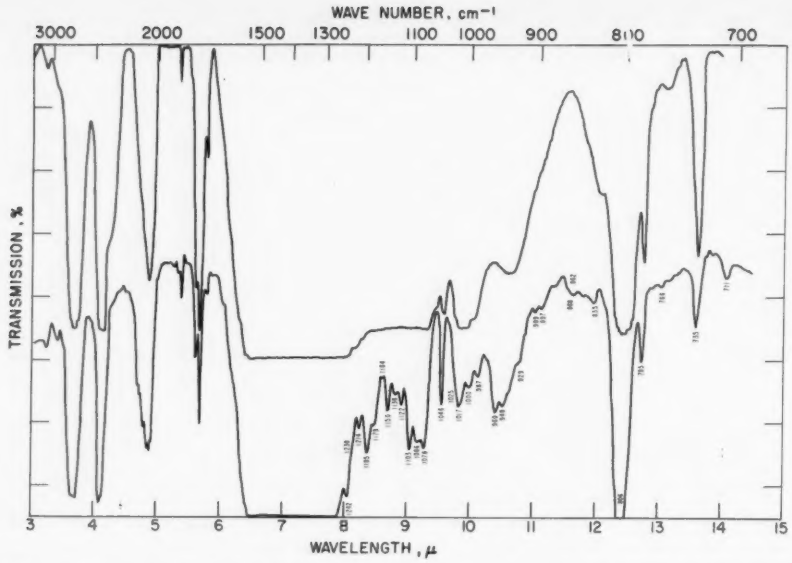

FIGURE 19. *Infrared absorption spectra of* $AgNO_3$ *at room temperature (top) and liquid helium temperature (bottom).*

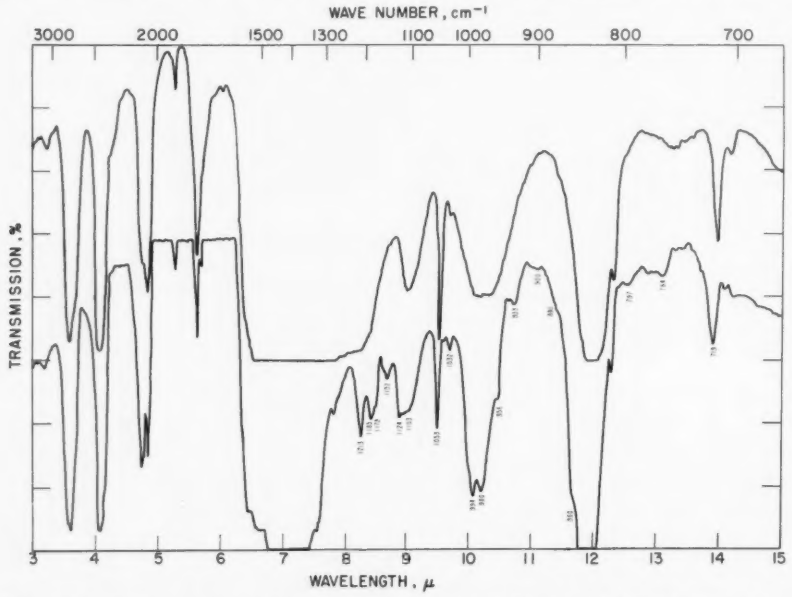

FIGURE 20. *Infrared absorption spectra of* $CsNO_3$ *at room temperature (top) and liquid helium temperature (bottom).*

tional modes are involved must be rejected. However, there remains the possibility that the bands arise from combinations between the fundamental and successive levels of a translational mode of frequency near 30 cm^{-1}. The relative insensitivity of the frequency to the crystal structure and the mass of the cation and the independent evidence for libration makes this interpretation appear doubtful. In addition the band limit or cutoff frequency which is of the same general order of magnitude in all these materials is readily understood in terms of libration. It can be explained with somewhat more difficulty for translation. It appears that the majority of evidence available at this time appears to favor the interpretation of the data in terms of libration. However, it must be emphasized that on the basis of the present evidence, a translational origin for the observed bands cannot be rejected unequivocally.

The effect of temperature on the frequency, intensity, and shape of the summation bands has been noted in the discussion. It is to be expected that the frequencies of the bands involving a lattice mode should be more temperature dependent than

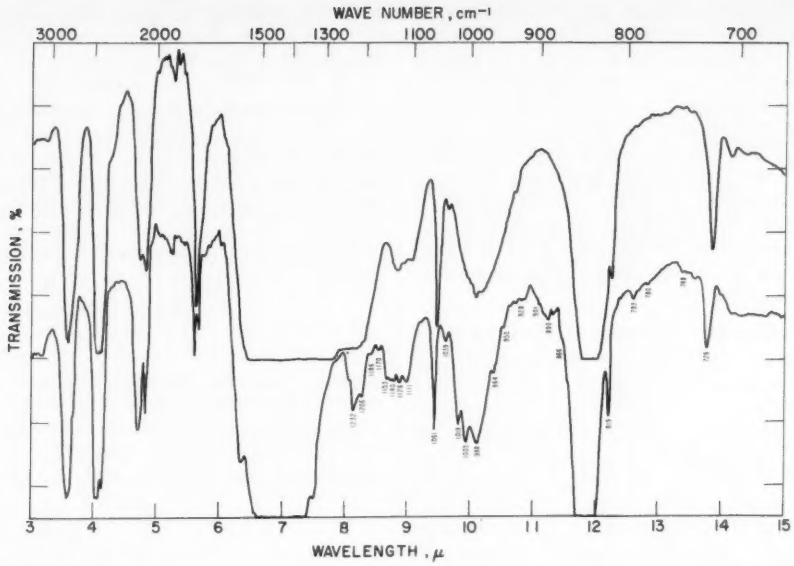

FIGURE 21. *Infrared absorption spectra of* $RbNO_3$ *at room temperature (top) and liquid helium temperature (bottom).*

the fundamentals. The lattice frequencies will depend on the interionic forces which are directly affected by the change in volume produced by cooling. If the forces are principally repulsive a shift to higher frequencies would be expected on cooling. This is actually observed. The fundamental internal frequencies have been shown to be rather insensitive to changes in volume. The intensity of the summation bands is expected to increase with decreasing temperature in these experiments. At ordinary temperatures, the higher librational levels are expected to be densely populated because of the low energy involved. As the temperature is lowered the lower levels increase in population at the expense of the higher levels. In absorption the intensity depends on the population of the lower of the two levels involved and, all other factors being equal, intensity should increase markedly as the lower levels become populated. Simultaneously it appears reasonable that the individual librational band widths should decrease.

Translational lattice modes must exist and no attempt has been made to identify these modes which would be active in combination with the fundamentals. However, in every spectrum there appear to be a few bands not falling into a regular sequence which might be assigned in this manner. There are also many unusually strong bands which might be attributed to superposition of a libration and translation combination with the fundamental. Such coincidences would be expected to be of frequent occurrence in a series of close spaced bands and might produce resonance splitting effects. Such splitting may produce the variation in spacing observed in some series of bands.

On the basis of the librational motion the cutoff frequencies are readily interpreted. According to Lander [45] the oxygen-oxygen interaction between neighboring anions defines the ordering. Spectroscopic data on the nitrates, carbonates, and borates [77] has also been interpreted in this manner. In a given crystal the anion should orient in the potential field in such a position that its oxygen atoms would be at a maximum distance from the neighboring oxygens. This position is not unique, however, as equivalent positions can be obtained by a rotation about the trigonal axis, potential minima being found every 120° or every 60° depending on the symmetry of the site. If sufficient energy is available a librating anion can surmount the energy barrier imposed by the repulsive forces of neighboring oxygen atoms and either rotate freely or, on losing energy, take up an equivalent position displaced by 120° or 60° from the original position. Therefore the librational bands should terminate at a frequency corresponding to the "free rotation" energy barrier.

No convincing arguments can be offered at this time for the intensity relationships in a series of bands. Hexter and Dows [35] have calculated that higher order combinations of the type postulated here should decrease in intensity exponentially. However, these calculations did not consider the interactions between neighboring ions. It appears reasonable to suppose that libration of the anion produces a change in the electronic charge distribution of the oxygen atoms. It appears likely that the perturbation of the charge distribution increases with increasing amplitude of the oscillation and should reach a maximum at the top of the barrier. What the effect of this change in charge distribution would be on the relative intensities is not clear so that this question cannot be answered at this time.

At the top of the energy barrier the librational modes change rapidly from a vibrational type to a

rotational type. The intensity of transitions from a state corresponding to the ground vibrational level ($n=0$) and the ground librational level ($J=0$) to the upper vibrational level ($n=1$) and the upper rotational levels (say $J \geqq 10$) would be very weak because such transitions are forbidden by rotational selection rules. Therefore if librational transitions below the top of the barrier have appreciable intensity because of electrical anharmonicity a rather sharp cutoff or band limit is indicated. Rotational transitions in addition to being forbidden would be expected to be very weak because of the absence of electrical anharmonicity in rotational motion.

f. Discussion of Libration and Energy Barrier Data

The observed data on libration frequencies and apparent energy barriers are tabulated in the first two columns of table 18. The libration frequencies listed correspond to maximum values observed for each substance, i.e., average values derived from the lower energy levels. Despite the wide variation in structure it is interesting to note that variations of the absolute values of libration frequency and energy barrier are relatively small. Libration frequencies appear to range from 15 cm^{-1} to 36 cm^{-1} and energy barriers from 140 cm^{-1} to 250 cm^{-1}. No reliable libration frequency was observed from $MgCO_3$ although the probable barrier is listed in table 18. The barriers tabulated represent the average estimates of the bands assigned as the three cutoff values of the three series of bands arising from combinations with ν_1, ν_2, and ν_4 which usually agree very well with each other.

Although qualitative arguments for libration have been presented in the previous section it remains to be demonstrated that the observed energy barriers are quantitatively of the correct order of magnitude. The following discussion will be limited to the calcite and cubic structures because of the uncertainties involved in the other structures. In addition only the data for $NaNO_3$ and $CaCO_3$ among the calcite structures will be considered because of doubts concerning the purity of the other materials. Column 3 of table 18 lists approximate anharmonicity corrections calculated from the observed frequencies for $CaCO_3$ (table 5), $NaNO_3$ (table 4), $Sr(NO_3)_2$ (table 13), $Ba(NO_3)_2$ (table 12), and $Pb(NO_3)_2$ (table 11). The anharmonicity corrections are observed to much larger for the calcite structures than for the cubic structures. This difference will be discussed subsequently. From the observed libration frequencies and the anharmonic corrections, the potential barrier for rotation may be calculated as follows.

TABLE 18. *Collected libration frequencies and energy barriers from infrared spectra at liquid helium temperature*

Material	Observed barrier [a]	Libration frequency, ν_L	Approximate anharmonicity correction	Calculated barrier [b]
	cm^{-1}	cm^{-1}	cm^{-1}	cm^{-1}
$MgCO_3$	220			
$CaCO_3$	152	36	1	162
$FeCO_3$	150	25?		
$MnCO_3$	160	25?		
$NaNO_3$	238	32	3	155
$Sr(NO_3)_2$	220	20	0.5	198
$Ba(NO_3)_2$	191	19	.5	179
$Pb(NO_3)_2$	167	18	.5	161
$TlNO_3$	255	25?		
$AgNO_3$	223	30?		
$CsNO_3$	161	25		
$RbNO_3$	175, 146	15, 30		

[a] Experimental values neglecting zero point energy. Approximate correction for zero point energy is $\nu_L/2$.

[b] Calculated barriers including correction for anharmonicity but neglecting correction for zero point energy. Approximate correction for zero point energy is $\nu_L/2$.

Assuming a rotational potential energy of the form

$$V=\frac{V_0}{2}(1-\cos n\theta) \tag{1}$$

where V_0 is the energy barrier, n the number of potential minima in a complete cycle, and θ the angular displacement from the equilibrium position, the potential barrier can be calculated from the libration frequency through the relationship

$$\nu_c=n\sqrt{\frac{V_0 h}{8\pi^2 cI}}. \tag{2}$$

In eq (2), ν_c corresponds to the corrected libration frequency, I the moment of inertia of the anion, and the other quantities have their usual significance. The corrected libration frequency is taken as equal to the observed libration frequency plus twice the anharmonic correction [33]. Taking the C—O and N—O bond lengths to be 1.25 A and 1.22 A, respectively, and independent of structure [80], the following two relationships for the potential barriers are obtained.

$$\text{for carbonates } V_0=4.26(\nu_c/n)^2. \tag{3}$$

$$\text{for nitrates } V_0=4.47(\nu_c/n)^2. \tag{4}$$

In calcite structures the anions occupy sites of symmetry D_3 and $n=6$. In the cubic structures the site symmetry is C_3 and $n=3$. Using eqs (3) and (4) and the corresponding data from table 18 the barriers were calculated and are given in column 4 of the table. The calculated barriers as tabulated have been corrected for the zero point energy contribution so as to be comparable with the observed values, that is the tabulated values represent the calculated barriers minus ½ the libration frequency.

A comparison of observed and calculated barriers shows that except for $NaNO_3$ the agreement is quite encouraging. Inasmuch as the libration frequencies cannot be determined with precision because of the width of the bands, and since a similar error exists in determining the cutoff frequencies, it is considered that the agreement between calculated and observed barriers is probably within the experimental error even in the case of $NaNO_3$. Furthermore the calculated barrier is dependent on the exact shape of the potential energy curve and on the bond distance used. The fact that the observed and calculated barriers are of the same order of magnitude supports the present interpretation of the observed spectra in

terms of librational oscillations of anions that produce a series of bands terminating in a cutoff frequency which corresponds to the potential barrier for rotation.

The fact that the barriers are of the same order of magnitude implies that in these crystals the forces are of the same nature. This conclusion has been reached previously [77]. The smaller anharmonicity corrections of the cubic salts as compared with those of the calcites are to the expected. In the former there appear to be broader potential wells ($n=3$) than in the latter ($n=6$) and the levels are closer (20 cm^{-1} as compared to 30 cm^{-1}).

It will be noted that the agreement between calculated and observed barriers also implies that the assignments of the individual libration bands is essentially correct. If the data for $CsNO_3$ and $RbNO_3$ are used to calculate barriers it appears most likely that the nitrate ions must occupy sites of six-fold symmetry in these structures. However, similar calculations for $TlNO_3$ and $AgNO_3$ are not possible because of the great uncertainty in assigning the libration bands. From this point of view it is not surprising that the aragonite spectra is so complex because the anions occupy sites of symmetry C_s.

The absolute value of the potential barriers observed requires the conclusion that at ordinary temperatures, i.e., 300 °K, a considerable number of anions have energies in excess of the hindering rotational barrier. If large numbers of anions rotate, it is conceivable that the structure may become unstable. Several phase changes occur in the nitrates at moderate temperatures but the corresponding transitions in the carbonates take place only at relatively high temperatures [45]. There is no obvious correlation between the transition temperature and the height of the energy barrier. It must be concluded, therefore, that the cohesive energy of the crystal lattice is sufficient to accommodate considerable variation in the anion disorder and that the transitions are not caused primarily by the effect of the disordering. Since similar transitions in nitrates and carbonates are separated by several hundred degrees in temperature it appears that the cohesive energy, which is expected to be roughly four times as great in the carbonates, must largely determine the transition temperature. On the basis of the present interpretation most of the carbonate ions would have energies above the rotational energy barriers at temperatures well below the transition temperatures.

3.4. Overtones and Combinations of Fundamentals

Inspection of figures 1–21 for the carbonates and nitrates shows that numerous strong bands occur in the range 1700 cm^{-1} to 3000 cm^{-1}. The prism instrument provided insufficient dispersion and resolution for accurate study of this region. However, the number and strength of the bands indicate that free ion selection rules are not applicable in these crystals. In most spectra two sharp bands are observed, one near 1750 cm^{-1} and the other much weaker near 1800 cm^{-1}. Without exception these bands are located within a few wave numbers of the positions expected for the combinations $\nu_1+\nu_4$ and $\nu_1+\nu_2$, respectively. These bands can be assigned confidently. The other bands cannot.

For further study of this region several spectra were obtained on a grating spectrometer. The spectral regions from 1600 cm^{-1} to 4000 cm^{-1} for the liquid helium runs are given in figures 22, 23, 24, and 25 for $CaCO_3$, KNO_3, $BaCO_3$, and $Ba(NO_3)_2$ respectively. Frequencies of bands identifiable with certainty are listed in tables 19, 20, 21, and 22. The studies showed no appreciable shift of band positions in this region as the temperature was lowered although considerable sharpening of bands occurred at low temperature. Inspection of the spectra shows a very complex band system in this region and no assignments are given. It is particularly noted that in regions in which bands would be expected to correspond to the combinations $\nu_1+\nu_3$ and $2\nu_3$ the spectra show strong broad bands which appear to contain unresolved structure. Also of interest are the many bands appearing to contain shoulders extending more than 100 cm^{-1} to higher frequencies. Conversely similar shoulders are missing on the low frequency side. The spectra of KNO_3 and $Ba(NO_3)_2$ are particularly complex in this region. Several triple groups are evident in $Ba(NO_3)_2$ with components separated by about 30 cm^{-1} and 40 cm^{-1}. In general this region of the spectra does not offer any evidence to contradict the libration hypothesis and the complexity and broad bands would be expected if there is a libration-fundamental combination involved.

TABLE 19. *Overtones and fundamental combinations observed for calcite*

Frequencies	Frequencies	Fundamentals
cm^{-1}	cm^{-1}	cm^{-1}
3935 m	2798 m sh	ν_1—1070
3735 w	2560 vs	ν_2—881
3587 m	2490 s	ν_3—1460?
3218 m	2330 mb	ν_4—712
3175 m	2210 mb	
2915 vs	2142 m	
	1960 m	

TABLE 20. *Overtones and fundamental combinations observed for* KNO_3

Frequencies	Frequencies	Fundamentals
cm^{-1}	cm^{-1}	cm^{-1}
3734 m shoulder to 3900	2395 s sh	ν_1—1051
3425 m shoulder to 3550	2360 m	ν_2—827
3103 w	2335 mb	ν_3—1420
3006 w	2150 mb	ν_4—714
2850 mb shoulder to 2970	2090 mb	
2782 mb	2060 m	
2733 m	1920 w	
2718 sh	1890 m	
2695 m	1875 ms ($\nu_1+\nu_2$)	
2550 mb shoulder to 2610	1762 s ($\nu_1+\nu_4$)	
2485 sb	1745 m	
2422 m		

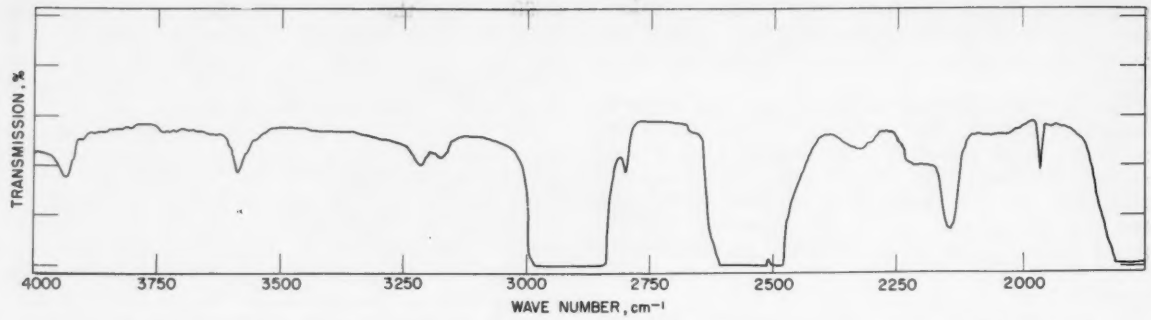

FIGURE 22. *Infrared absorption spectrum of* $CaCO_3$ *(calcite) at liquid helium temperature (1600 cm⁻¹ to 4000 cm⁻¹).*

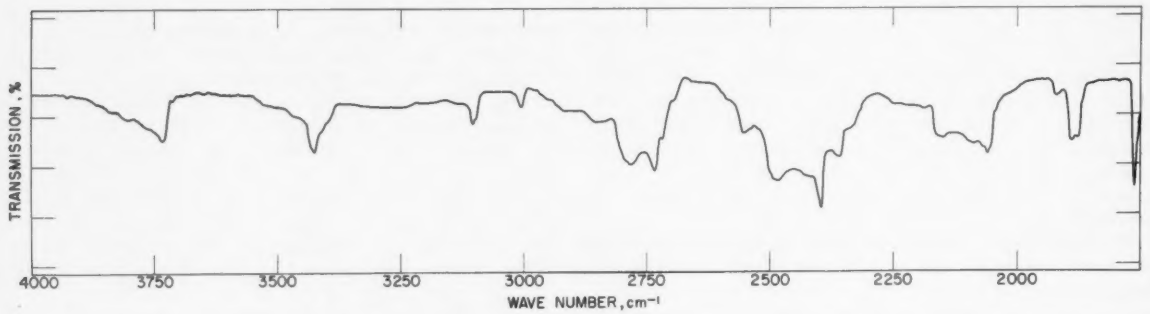

FIGURE 23. *Infrared absorption spectrum of* KNO_3 *at liquid helium temperature (1600 cm⁻¹ to 4000 cm⁻¹).*

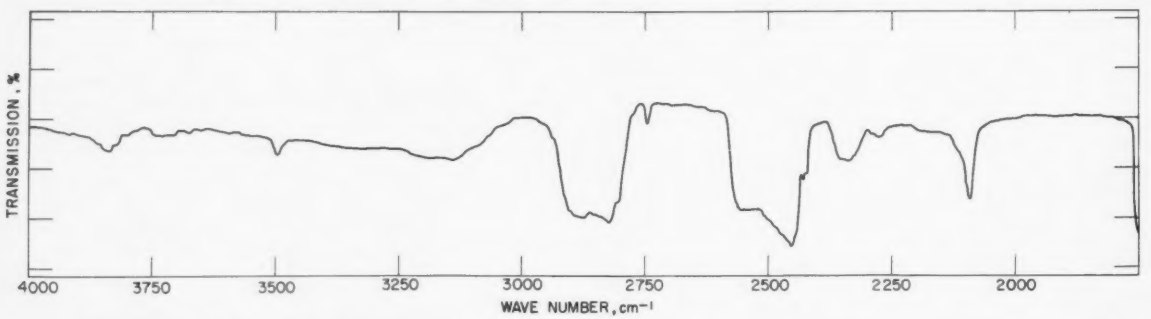

FIGURE 24. *Infrared absorption spectrum of* $BaCO_3$ *at liquid helium temperature (1600 cm⁻¹ to 4000 cm⁻¹).*

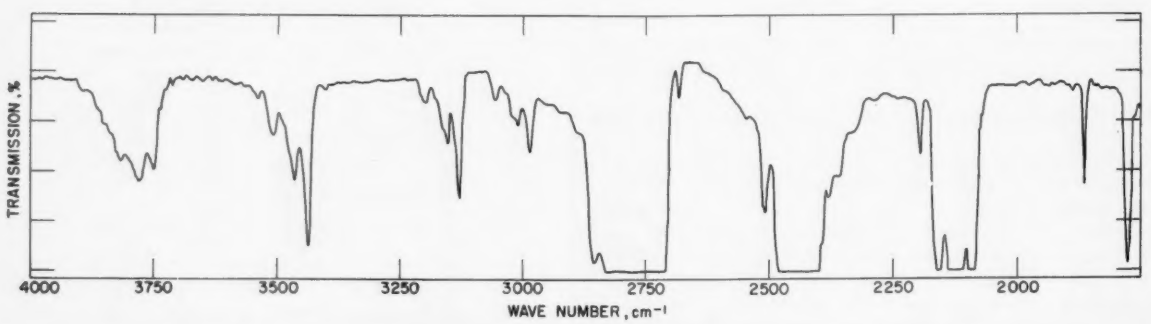

FIGURE 25. *Infrared absorption spectrum of* $Ba(NO_3)_2$ *at liquid helium temperature (1600 cm⁻¹ to 4000 cm⁻¹).*

TABLE 21. *Overtones and fundamental combinations observed for* $BaCO_3$

Frequencies	Frequencies	Fundamentals
cm^{-1}	cm^{-1}	cm^{-1}
3840 wb	2452 s	ν_1−1062
3498 w	2430 sh	ν_2−857
2880 sb	2423 sh	ν_3−1470
2820 b	2340 b	ν_4−732, 694
2805 sh	2092 sh	
2746 w	1755 sh ($\nu_1+\nu_4$)	
2550 sb	1748 s	
	1735 sh	

TABLE 22. *Overtones and fundamental combinations for* $Ba(NO_3)_2$

Frequencies	Frequencies	Fundamentals
cm^{-1}	cm^{-1}	cm^{-1}
3817	2683 m sh	ν_1−1052
3780 s	2550 b	ν_2−813
3750	2510 b	ν_3−1400?
3508	2440 b	ν_4−722
3465 s	2380 b	
3435	2360 b	
3200	2330 b	
3155 s	2290 b	
3128	2195 m	
3055	2156 vs	
3010 m	2120 vs	
2985	2090 s	
2885 w	1863 m ($\nu_1+\nu_2$)	
2855 s	1775 s ($\nu_1+\nu_4$)	
2770 vs	1620	

4. Conclusion

Infrared absorption spectra of inorganic nitrates and carbonates have been obtained on single crystals at room temperature, liquid nitrogen temperature, and liquid helium temperature. The diffuse absorption observed in the room temperature spectra between about 1400 cm^{-1} and 700 cm^{-1} is resolved at liquid helium temperature into a series of a large number of bands not attributable to fundamentals or combinations of fundamental frequencies of the anions. Most of these bands are readily interpreted as summation bands of fundamental frequencies with successive levels of a librating oscillator.

This interpretation is supported by the following, experimental observations:

1. The removal of the difference bands with reduction in temperature.
2. The large temperature dependence of the positions of individual bands as compared with that of the fundamentals.
3. The uniformity of the spacing of the individual bands within a given series of bands.
4. The similarity of the separation of the individual members of the separate series of bands from each of the fundamentals ν_1, ν_2, and ν_4.
5. The agreement in the separation of the band limits or cutoffs assigned from each of the fundamentals ν_1, ν_2, and ν_4.
6. The general similarity of the behavior in the vicinity of ν_3 with that observed at the other fundamentals, although the individual bands could not be distinguished.

The libration is considered to represent a planar torsional oscillation of the anion about the trigonal axis. The librational frequency appears to be dependent in part on the crystal structure and the ions involved. For a given material the librational frequency as determined from successive bands is reasonably constant. In the substances studied the librational frequency varied from about 15 cm^{-1} to 30 cm^{-1}.

Observed band limits in the spectra are interpreted as representing rotational energy barriers. These barriers are of the order of 200 cm^{-1} with the barrier height being dependent on the crystal structure and the ions involved. Barrier heights calculated from a cosine potential function agree reasonably well with the observed barriers for the cubic and calcite structures. Similar calculations have not been made for other structures studied because of doubtful assignments or unknown strucural details. In particular, the spectra of the aragonite structures are remarkable in detail and complexity and have not been analyzed successfully. However, the details of these and all other spectra studies appear to involve similar phenomena.

The question of whether this behavior is restricted to carbonates and nitrates cannot be answered fully. Preliminary studies on other salts at low temperatures indicates that similar band systems may exist. Further experiments are required to answer this question with certainty.

It is apparent that the band structure observed in these studies is not clearly seen in absorption spectra of thin films and polycrystalline specimens. In part, this may be due to the fact that it is customary in most instances to study specimens which do not absorb completely even in the strongest fundamentals and that the combination bands are too weak in comparison with the fundamentals to be observed under these circumstances. However, it would also appear likely that reduction of the crystal size below some minimum value as determined by the lattice mode might effectively eliminate the lattice mode and consequently the combination band. With lattice modes of low frequency the minimum crystal size might be readily attainable and preliminary investigations indicate some experimental evidence of a dimensional effect. Further study on these questions is under way.

The authors are indebted to L. Bolz for obtaining low temperature X-ray data.

5. Reference

[1] C. T. Anderson, J. Am. Chem. Soc. **56,** 340 (1934).
[2] C. T. Anderson, J. Am. Chem. Soc. **56,** 849 (1934).
[3] E. R. Andrew, J. Chem. Phys. **18,** 607 (1950).
[4] R. Bersohn and H. S. Gutowsky, J. Chem. Phys. **22,** 651 (1954).
[5] J. M. Bijvoet and J. A. A. Ketelaar, J. Am. Chem. Soc. **54,** 625 (1932).
[6] P. Chevin, W. C. Hamilton, and B. Post, American Crystallographic Assoc., Boulder, Colo. (July 31, 1961).
[7] M. Y. Colby and L. J. B. LaCoste, Z. Krist. **90,** 1 (1935).
[8] M. Y. Colby and L. J. B. LaCoste, Z. Krist. **84,** 299 (1933).

[9] L. Couture, Compt rend. **220,** 656 (1945).
[10] L. Couture and J. Mathieu, Ann. phys. **12,** 35 (1938).
[11] L. Couture and J. Mathieu, Compt. rend. **225,** 1140 (1947).
[12] L. Couture, Compt. rend. **220,** 87 (1945).
[13] L. Couture, J. Chem. Phys. **15,** 153 (1947).
[14] J. C. Decius, J. Chem. Phys. **23,** 1290 (1955).
[15] J. C. Decius, J. Chem. Phys. **22,** 1941 (1954).
[16] L. E. Drain, Faraday Soc. Discussions **19,** 200 (1955).
[17] D. A. Edwards, Z. Krist. **80,** 154 (1931).
[18] N. Elliott and J. Hastings, Acta Cryst. **14,** 1018 (1961).
[19] E. Ferrari, A. Sabatini, and P. Orioli, Gazz. chim. ital. **87,** 630 (1957).
[20] E. Ferrari, A. Sabatini, and P. Orioli, Ricerca sci. **27,** 1557 (1957).
[21] C. Finback and O. Hassel, J. Chem. Phys. **5,** 460 (1937).
[22] C. Finback and O. Hassel, Z. physik. Chem. **B35,** 25 (1937).
[23] J. Frenkel, Acta Physiocochim. **3,** 23 (1935).
[24] L. Guilotto and G. Olivelli, J. Chem. Phys. **16,** 555 (1948).
[25] G. Glockler, Rev. Mod. Phys. **15,** 111 (1943).
[26] E. F. Gross and A. A. Shultin, Sov. Phys. Dokl. **2,** 371 (1957).
[27] P. Gunther, Ann. Physik **51,** 828 (1916).
[28] H. S. Gutowsky, G. E. Pake, and R. Bersohn, J. Chem. Phys. **22,** 643 (1954).
[29] C. Haas and J. A. A. Ketelaar, Physica **22,** 1286 (1956).
[30] R. S. Halford, J. Chem. Phys. **14,** 8 (1946).
[31] W. C. Hamilton, Acta Cryst. **10,** 103 (1957).
[32] S. B. Hendricks, E. Posnjak, and F. Kracek, J. Am. Chem. Soc. **54,** 2766 (1932).
[33] G. Herzberg, Molecular Spectra and Molecular Structure, Vol. II, Infrared and Raman Spectra of Polyatomic Molecules, 7th ed., p. 178 (D. Van Nostrand & Co., New York, N.Y., 1956).
[34] R. M. Hexter, Spectrochim. Acta **10,** 291 (1958).
[35] R. M. Hexter and D. A. Dows, J. Chem. Phys. **25,** 504 (1956).
[36] J. H. Hibben, The Raman Effect and its Chemical Applications (Reinhold Publ. Corp., New York, N.Y., 1939) pp. 428 and 445.
[37] R. M. Hinde and E. A. Kellett, Acta Cryst. **10,** 383 (1957).
[38] D. F. Hornig, J. Chem. Phys. **16,** 1063 (1948).
[39] J. Jaffray, Ann. phys. **3,** 5 (1948).
[40] J. A. A. Ketelaar and B. Strijk, Rec. trav. chim, **64,** 174 (1945).
[41] F. C. Kracek, T. F. W. Barth, and C. J. Kasanda, Phys. Rev. **40,** 1034 (1932).
[42] D. Krishnamurti, Proc. Indian Acad. Sci. **46A,** 183 (1957).
[43] D. Krishnamurti, Proc. Indian Acad. Sci. **43A,** 210 (1956).
[44] R. S. Krishnan, Proc. Indian Acad. Sci. **31A,** 435 (1950).
[45] J. J. Lander, J. Chem. Phys. **17,** 892 (1949).
[46] W. M. Latimer and J. E. Ahlberg, Z. physik. Chem. **148,** 464 (1930).
[47] W. M. Latimer and J. E. Ahlberg, J. Am. Chem. Soc. **54,** 1900 (1932).
[48] A. W. Lawson, Phys. Rev. **57,** 417 (1940).
[49] H. A. Levy and S. W. Peterson, Phys. Rev. **86,** 766 (1952).
[50] H. A. Levy and S. W. Peterson, J. Chem. Phys. **21,** 366 (1953).
[51] T. Liebisch and H. Reubens, Ber. Akad. Wiss. Berlin 198 (1919).
[52] J. Louisfert, Compt. rend. **241,** 940 (1955).
[53] G. Lutz, Z. Krist. **114,** 232 (1960).
[54] F. A. Mauer, Formation and Trapping of Free Radicals (Academic Press Inc., New York, N.Y., 1960) ch. 5.
[55] T. M. K. Nedungadi, Proc. Indian Acad. Sci. **14A,** 242 (1941).
[56] Nernst and Schwers, Ber. Akad. Wiss. Berlin 355 (1914).
[57] R. Newman and R. S. Halford, J. Chem. Phys. **18,** 1291 (1950).
[58] R. Newman and R. S. Halford, J. Chem. Phys. **18,** 1276 (1950).
[59] L. Pauling, Phys. Rev. **36,** 430 (1930).
[60] L. Pauling and J. Sherman, Z. Krist. **84,** 213 (1933).
[61] R. C. Plumb and D. F. Hornig, J. Chem. Phys. **21,** 366 (1953).
[62] A. K. Ramdas, Proc. Indian Acad. Sci. **37A,** 441 (1953).
[63] B. L. Rao, Proc. Indian Acad. Sci. **14A,** 48 (1941).
[64] B. S. R. Rao, Proc. Indian Acad. Sci. **19A,** 93 (1944).
[65] S. Satoh, J. Sci. Research Inst. **48,** 59 (1948).
[66] C. Schaefer, C. Bormuth, and F. Matossi, Zeit. f. Phys. **39,** 648 (1926).
[67] C. H. Shomate and K. K. Kelley, J. Am. Chem. Soc. **66,** 1490 (1944).
[68] L. A. Siegel, J. Chem. Phys. **17,** 1146 (1949).
[69] W. V. Smith, O. L. Brown, and K. S. Pitzer, J. Am. Chem. Soc. **59,** 1213 (1937).
[70] J. C. Southard and R. A. Nelson, J. Am. Chem. Soc. **55,** 4865 (1933).
[71] Standard X-Ray Diffraction Powder Patterns, NBS Circular 539, Vol. 1–6.
[72] C. C. Stephenson, L. A. Landers, and A. G. Cole, J. Chem. Phys. **20,** 1043 (1952).
[73] L. Vegard and L. Bilberg, Norske Videns. Akad. Oslo, 1931–1933.
[74] E. L. Wagner and D. F. Hornig, J. Chem. Phys. **18,** 296 (1950).
[75] E. L. Wagner and D. F. Hornig, J. Chem. Phys. **18,** 305 (1950).
[76] L. Waldbauer and D. C. McCann, J. Chem. Phys. **2,** 615 (1934).
[77] C. E. Weir and E. R. Lippincott, J. Research NBS, **65A,** 173 (1961).
[78] H. Winston and R. S. Halford, J. Chem. Phys. **17,** 607 (1949).
[79] R. W. G. Wyckoff, Am. J. Sci. **9,** 145 (1925).

(Paper 66A5–176)

JOURNAL OF RESEARCH of the National Bureau of Standards—A. Physics and Chemistry
Vol. 66A, No. 5, September–October 1962

Foreign Gas Broadening of the Lines of Hydrogen Chloride and Carbon Monoxide

Earle K. Plyler and Robert J. Thibault

(June 7, 1962)

The Lorentz line shape formula is applied in the determination of half-width parameters due to foreign gas broadening. Various pressures of SO_2 and CO_2 are added to HCl and CO, respectively. The (1–0) and (2–0) HCl bands, as well as the (2–0) CO band, are investigated, and there is found to be a very definite relationship between the half-width and the rotational quantum number, J. No error of more than 5 percent should be expected for the values of γ^0 presented. Some pressure-shifts are observed for HCl, but no quantitative determinations are made.

1. Introduction

In recent years an interest has developed in the area of pressure-broadening effects. Several studies have been made in the field [1, 2, 3],[1] a great number of which have been restricted to the self-broadening of gases. There have also been some which have dealt with the broadening effects induced by the addition of a foreign gas to the sample under investigation. Many of these experiments, including the present one, have been performed using highly polar hydrogen chloride (see refs. 1, 2), because of its relative simplicity and freedom from overlapping. The proximity of the isotopic doublet HCl^{35} and HCl^{37} also allows one to establish a calibration reference without resorting to extrinsic methods.

Several similar studies have also been made with regard to carbon monoxide (see ref. 3). These have, for the most part, been limited to self-broadening.

The results of recent work on both HCl and CO have shown in general that the broadening effect becomes greater as one goes from a higher to a lower value of the rotational quantum number, J. This holds true for both self-broadening and foreign gas broadening.

The parameters of interest in such an investigation as this are the line strengths, shapes, and widths. From a knowledge of the line strength, S, information can be obtained regarding the quantum-mechanical transition probability. The width and shape of a line are directly related to the specific intermolecular forces involved in the broadening process. The relationship between these parameters may most easily be seen by referring to the well-known Lorentz line shape formula

$$k=\frac{S}{\pi}\frac{\gamma}{(\nu-\nu_0)^2+\gamma^2}, \tag{1}$$

where k is the extinction coefficient and γ is the Lorentz half-width.

The strengths of the individual lines of both HCl and CO have been measured by several investigators (see refs. 1, 2, 3). Emphasis in the present work, therefore, is placed on the evaluation of the half-width parameter, γ, of lines broadened by the addition of a foreign gas to the sample in question. A nonlinear molecular gas, namely sulfur dioxide, is added to HCl, while carbon dioxide is the foreign gas used in the CO broadening study. Both the (1–0) and (2–0) bands of HCl, as well as the (2–0) band of CO, are extensively investigated. Some measurements of the (1–0) CO band are made to be used as a comparison with the values obtained from the harmonic band.

A major difficulty encountered in work of this kind is the deviation of a spectral line from its true shape caused by instrumental distortion. Although the resolving power of the instrument used in this work is quite high, it is still necessary to modify the observed half-width values by the inclusion of a slit width correction. In certain cases, notably in the (2–0) band of HCl, these corrections become as large as 20 percent of the line half-width.

No attempt is made here to determine the absolute positions of the individual spectral lines, since this has been done quite accurately in the past [4, 5, 6].

2. Experiment

The spectrometer used in the present experiment is the high resolution grating spectrometer previously described by Plyler and Blaine [7]. The instrument was provided with double pass optics and had a total path length of approximately 13 m.

For the HCl study the source of radiation employed for both the (1–0) and the (2–0) bands was a 300 w Sylvania enclosed zirconium arc, while a Nernst glower was used for the investigation of CO broadening in the fundamental band. A 10,000 lines/in. Bausch and Lomb grating was employed in the first order for the (1–0) HCl band and for the (2–0) CO band. The second order of the grating was used for the (2–0) band of HCl. Suitable optical transmission filters were inserted in the path of radiation to insure the purity of the desired grating order.

[1] Figures in brackets indicate the literature references at the end of this paper.

645080—62——5

The detector used in all cases was a liquid-nitrogen cooled lead sulfide photodetecting cell. A satisfactory signal-to-noise ratio of about 50 was obtained with a spectral slit width of 0.04 cm^{-1} in the HCl fundamental, 0.075 cm^{-1} in the HCl harmonic, and 0.05 in the (2–0) CO band.

Two 10-cm absorption cells, one monel and the other glass, were employed. Both had sapphire windows of equal transmission. Both cells were measured empty before and after use, in order to corroborate the assumption that the background contribution was negligible.

Measured pressures of HCl and SO_2 were added to the cells. The pressures covered a range of from 0.2 to 20 cm (Hg) of HCl, and from 35 to 132 cm (Hg) of SO_2. These pressure combinations were then measured through both isotopes of each HCl line at room temperature. While scanning a line the grating was rotated by approximately 18 sec of angle per minute of time, which provided an accurate reproduction of spectral energy distribution.

Utilizing the scanning method described above, a suitable spectrum of $CO+CO_2$ was then obtained for various pressure combinations, ranging from 19 to 45 cm (Hg) of CO, and from 42 to 158 cm (Hg) of CO_2.

A mounting method was devised whereby an SO_2-broadened HCl line could be compared with a self-broadened line at the same HCl pressure. This system consisted of merely shifting the cells alternately into and out of the radiation path while the spectrometer was in continuous operation. This method of rapid alternation was used to investigate the pressure shift between the two lines. In this case the result was, effectively, the superposition of one line upon the other.

3. Results

Figure 1 shows a typical self-broadened and SO_2-broadened HCl isotopic doublet. The peak extinction was measured on each HCl^{35} line wherever feasible. Where the observed absorption approached 100 percent, the HCl^{37} line was measured, and the result multiplied by the chlorine isotopic abundance ratio, $\left(\frac{Cl^{35}}{Cl^{37}} \approx 3.07\right)$, to determine the extinction coefficient of the HCl^{35} line in question. This abundance ratio was checked using doublets where both isotopes were well below 100 percent absorption, and seemed to be a good approximation.

The extinction at several values of $|\nu - \nu_0|$ was then calculated from the Lorentz line shape formula eq (1). This equation has been shown by Benedict, Herman, Moore, and Silverman (see ref 1) to be valid far enough from the resonant frequency to render it serviceable in the present work. It was then possible to measure directly on the trace the half-width parameter, γ. This was done at many points on each line corresponding to different extinction percentages.

The average deviation of the several values of γ determined for each line was found to be no more than 2 percent. It should be noted that measurements in all cases were made on both the P and the R branches. The results were found to be well within the same limits for both branches.

As has previously been mentioned, a correction for the slit width was determined using the corrections given by Izatt [8]. These varied from 0.5 percent to 20 percent, depending on the pressure and on the spectral slit width.

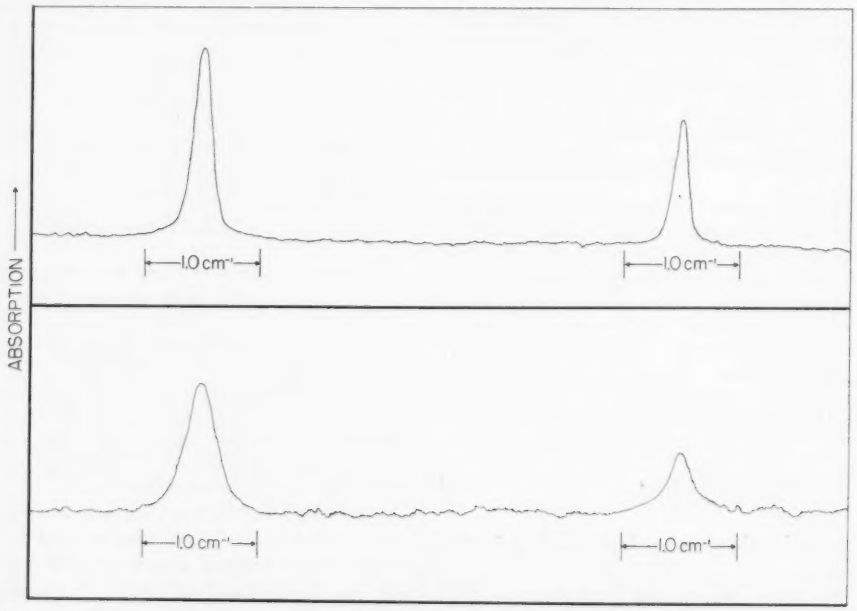

FIGURE 1. *The upper curve shows the* HCl *line R_2 of the 2–0 band with a pressure of 11 cm* (Hg). The lower curve shows the same line of HCl at 11 cm (Hg) pressure with 35 cm (Hg) of SO_2 added.

The values of the half-width parameter given by Benedict et al. (see ref 1) for self-broadened HCl were then employed to determine the effect of SO_2-broadening on the HCl line in question. The equation used was the following:

$$\gamma^0_{(SO_2)} P_{(SO_2)} = \gamma^0_{(tot)} P_{(tot)} - \gamma^0_{(HCl)} P_{(HCl)}. \quad (2)$$

The contribution of the self-broadening term can be seen in table 1. Table 2 gives the average values of $\gamma^0_{(SO_2)}$, where

$$\gamma^0_{(SO_2)} = \frac{\gamma_{(SO_2)}}{P_{(SO_2)}}. \quad (3)$$

The numbers in parentheses in table 2 denote the total number of measurements averaged in each case. A graph of $\gamma^0_{(SO_2)}$ versus $|m|$ is given in figure 2 for both the (1–0) and the (2–0) bands of HCl.

Again using the Lorentz shape formula, the line strengths of several (1–0) HCl doublets were calculated. When corrected for the slit width, these were in general agreement with those published by Babrov et al. [9].

TABLE 1. *Observed half-width, γ, and half-widths corrected for self-broadening for several values of $|m|$*

$\|m\|$	HCl		CO	
	1-0 band		2-0 band	
	1.8 cm HCl + 74.2 cm SO_2		19 cm CO + 57 cm CO_2	
	$\gamma_{(tot)}$	$\gamma_{(SO_2)}$	$\gamma_{(tot)}$	$\gamma_{(CO_2)}$
	cm^{-1}	cm^{-1}	cm^{-1}	cm^{-1}
1				
2	0.253	0.247		
3	.170	.164		
4	.111	.105	0.0823	0.0663
5	.0950	.0896	.0784	.0631
6	.0820	.0775	.0754	.0593
7	.0675	.0638	.0738	.0587
8	.0650	.0620	.0682	.0540
9	.0620	.0595	.0710	.0572
10			.0660	.0513
11			.0628	.0492
12			.0600	.0474

TABLE 2. *Half-widths $\gamma^0_{(SO_2)}$ for* HCl, *and $\gamma^0_{(CO_2)}$ for* CO

$\|m\|$	HCl		CO
	1-0 band	2-0 band	2-0 band
	$\gamma^0_{(SO_2)}$	$\gamma^0_{(SO_2)}$	$\gamma^0_{(CO_2)}$
	cm^{-1} atm^{-1}	cm^{-1} atm^{-1}	cm^{-1} atm^{-1}
1	0.388 (4)		0.122 (10)
2	.262 (6)	0.253 (7)	.110 (12)
3	.173 (6)	.171 (8)	.0967 (12)
4	.116 (6)	.109 (7)	.0901 (10)
5	.0902 (6)	.0852 (2)	.0839 (12)
6	.0760 (6)	.0806 (4)	.0765 (11)
7	.0697 (5)	.0739 (4)	.0736 (12)
8	.0660 (4)	.0734 (2)	.0720 (10)
9	.0610 (4)	.0670 (1)	.0703 (11)
10	.0621 (3)		.0658 (10)
11	.0586 (4)		.0652 (7)
12	.0529 (3)		.0650 (4)
13			.0646 (2)
14			.0606 (3)
15			.0608 (1)

The method described above for HCl was also used in the determination of $\gamma^0_{(CO_2)}$ for several $|m|$ values of the (2–0) CO band. In this calculation the $\gamma^0_{(CO)}$ values employed were those published by Benedict et al. (see ref 3).

The Lorentz shape formula was seen to be valid for $|\nu - \nu_0| < 4$ cm^{-1}, and, as was the case for HCl, no wing correction was included in the values of $\gamma^0_{(CO_2)}$ listed in table 2. These $\gamma^0_{(CO2)}$ values were obtained through a method similar to that employed in the case of HCl. The following equation applies:

$$\gamma^0_{(CO_2)} P_{(CO_2)} = \gamma^0_{(tot)} P_{(tot)} - \gamma^0_{(CO)} P_{(CO)} \quad (4)$$

where the average deviation of the $\gamma_{(tot)}$ was found to be of the same order as that reported for $\gamma_{(tot)}$ in the HCl study ($\leq 2\%$).

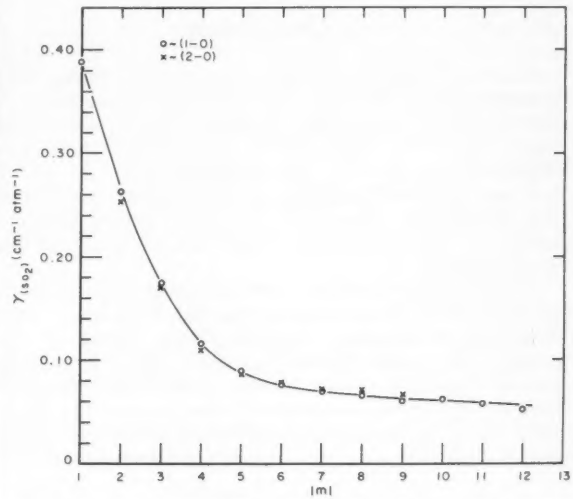

FIGURE 2. *The half-widths, $\gamma^0_{(SO_2)}$, of* HCl *broadened by* SO_2 *plotted as a function of the rotational level,* |m|.

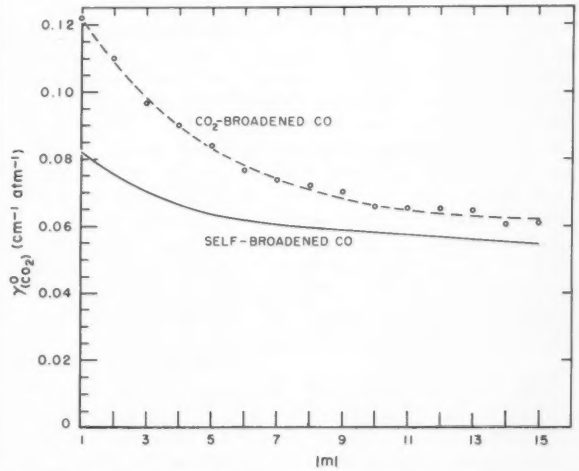

FIGURE 3. *The half-widths, $\gamma^0_{(CO_2)}$, of* CO *broadened by* CO_2 *plotted as a function of the rotational level,* |m|.
Also, self-broadened CO curve, taken from Benedict et al. (see ref 3).

The effect of self-broadening introduced by eq (4) is somewhat larger for CO than it was in the case of HCl, as is evident from table 1.

The average values of $\gamma^{\circ}_{(CO_2)}$ are shown in figure 3, along with the $\gamma^{\circ}_{(CO)}$ self-broadening parameters published by Benedict et al. (see ref 3), for ready comparison.

As has been mentioned, some measurements of CO_2-broadened CO fundamental lines were made. These agreed within ± 5 percent with the $\gamma^{\circ}_{(CO_2)}$ values obtained for the CO (2–0) band. This is well within experimental error, since the presence of unidentified overlapping bands made the fundamental quite difficult to measure.

Throughout this work it has been assumed that the broadening effect is linear with pressure. This was found to be the case, as is illustrated in figure 4.

4. Conclusion

Figures 2 and 3 show a regular correspondence between the half-width broadening parameter and the rotational quantum number, J, as was to be expected. This very definite relationship has been explained by several investigators [10,11]. There was no appreciable difference demonstrated between the broadening effects on the fundamental and the harmonic bands in either of the two molecules under investigation.

Since insufficient data were obtained regarding the pressure shift effect induced on SO_2-broadened HCl lines, no conclusions regarding this aspect of the present work will be drawn at this time. It may be noted, however, that a red shift was observed ($\sim$0.01 cm^{-1}/atm) in some of the lines of the (2–0) HCl band, as has been reported by Hirshfeld, Jaffe, and Kimel [12].

The authors express their gratitude to W. S. Benedict for his many helpful comments and suggestions regarding this paper.

(Paper 66A5–177)

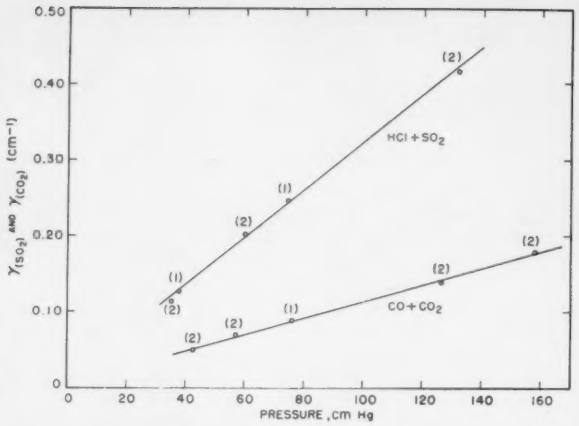

FIGURE 4. *The relationship between half-widths and pressure.*

The HCl+SO_2 line is given for $|m|=2$, and the CO+CO_2 line is given for $|m|=4$. The numbers in parentheses indicate whether the data were obtained from the 2-0 or the 1-0 band.

5. References

[1] W. S. Benedict, R. Herman, G. Moore, and S. Silverman, Can. J. Phys. **34,** 850 (1956).
[2] S. Kimel (Doctorate), Weizmann Inst. of Sci., Rehovoth Israel (1960).
[3] W. S. Benedict, R. Herman, G. Moore, and S. Silverman, Astrophys. J. **135,** 1, 277 (1962).
[4] D. H. Rank, W. B. Birtley, D. P. Eastman, B. S. Rao, and T. A. Wiggins, J. Opt. Soc. Am. **50,** 1275 (1960).
[5] E. K. Plyler and E. D. Tidwell, Z. Electrochem. **64,** 717 (1960).
[6] E. K. Plyler, A. Danti, L. R. Blaine, and E. D. Tidwell, J. Research NBS **64A,** (Phys. and Chem.) No. 1, 29 (1960).
[7] E. K. Plyler and L. R. Blaine, J. Research NBS **62,** 7 (1959).
[8] J. R. Izatt, Progress Rep., J. Hopkins Univ., Lab. of Astrophys. and Phys. Meteorology (1960).
[9] H. Babrov, G. Ameer, and W. Benesch, J. Mol. Spec. **3,** 185 (1959).
[10] P. W. Anderson, Phys. Rev. **76,** 647 (1949).
[11] W. V. Smith and R. Howard, Phys. Rev. **79,** 132 (1950).
[12] M. A. Hirshfeld, J. H. Jaffe, and S. Kimel J. Chem. Phys. **32,** 297 (1960).

JOURNAL OF RESEARCH of the National Bureau of Standards—A. Physics and Chemistry
Vol. 66A, No. 5, September–October 1962

Monolayers of Adipate Polyesters at Air-Liquid Interfaces [1]

Wendell M. Lee, Robert R. Stromberg, and J. Leon Shereshefsky [2]

(June 13, 1962)

The surface pressure-area isotherms at 24.5 °C are reported for poly(ethylene adipate), poly(trimethylene adipate), and poly(propylene adipate), spread as monolayers at air-aqueous interfaces. The monolayers were spread on distilled water and 0.01 *N* HCl, using benzene, chloroform, and acetone as spreading solvents. Poly(propylene adiptate) was the least compressible of the three, and poly(ethylene adipate) the most. Poly(propylene adipate) did not collapse at the highest pressures studied. The spreading characteristics of both poly(ethylene adipate) and poly(propylene adipate) were independent of the amount of material used. The spreading of poly(trimethylene adipate) appeared to depend upon the spreading solvent. The effect of structure on the surface pressure—area isotherms and the specific areas for each polymer are discussed.

1. Introduction

The monolayer properties of a series of linear succinate polyesters, with a number-average molecular weight ($\bar{M}_n$) of the order of 4,500, at air-aqueous interfaces were recently reported [1]. It was shown that the monolayer of poly(ethylene succinate) was highly expanded but that it collapsed at very low surface pressures. Poly(pentamethylene succinate) monolayers were also expanded. They did not collapse with increasing pressure, but the surface compressibility went through a maximum and continued to decrease as the pressure increased. An isomer of this polymer, poly(neopentyl succinate), produced a much less expanded film which collapsed at a surface pressure higher than that observed for collapse or pressure decrease for the other two polymers. It also gave the smallest extrapolated specific area per repeating unit. Other work has been reported on polyesters by Harkins, Carmen, and Ries [2] and Moss [3].

The work reported in this paper is concerned with a surface film balance study of three linear saturated polyesters of adipic acid at the liquid-air interface.

2. Experimental Procedure

The polyesters used in this investigation were: poly(ethylene adipate) $[\text{-O(CH}_2)_2\text{OCO(CH}_2)_4\text{CO-}]_n$, poly(trimethylene adipate) $[\text{-O(CH}_2)_3\text{OCO(CH}_2)_4\text{CO-}]_n$, and poly(propylene adipate) $[\text{-OCH(CH}_3)\text{CH}_2\text{OCO(CH}_2)_4\text{CO-}]_n$. These polymers were prepared by Dr. James Farr, Jr., of the Thiokol Chemical Company and were synthesized from the melt without catalyst. They were purified by reprecipitation from chloroform solution with ethyl ether and dried in vacuum. Some of the bulk properties of these polymers are given in table 1.

The film balance used to study the monolayers of the spread films has been described previously [1]. The water used as a subphase was redistilled from an all-quartz system. The spreading solvents were twice distilled and tested for active impurities by measurements of the surface pressure of the solvent alone. The polymer solutions were spread from micropipets and 10 min usually allowed for solvent evaporation. The average time of an experiment was 1 hr. All measurements were made at 24.5 ±0.5 °C.

TABLE 1. *Bulk properties*

Polymer	Softening point	Molecular weight M_n [a]	Bulk density at 27 °C	Physical state at 23 °C [b]
	°C		g/cm³	
Poly(ethylene adipate)	51	3800	1.3	Crystalline
Poly(trimethylene adipate)	40	4000	1.3	Crystalline
Poly(propylene adipate)	----------	5400	1.2	Viscous liquid

[a] M_n, number average molecular weight determined from supplied end group analysis.
[b] Crystallinity detected by X-ray diffraction.

3. Results

The monolayer properties of poly(ethylene adipate) spread from benzene and chloroform on the two substrates are given in figures 1 and 2. The surface pressure in dynes per centimeter is shown as a function of the specific area of the polymer (area per unit weight). All of the runs shown in figure 1 were obtained using benzene as the spreading solvent. Extrapolation of the linear portion of the curve drawn gives a limiting specific area of 2.6 m²/mg. In order to obtain the entire isotherm 30.36×10^{-3} mg of polymer was used for the region of high surface pressure and 5.50×10^{-3} mg for the region of low surface pressure and large area. Both regions were reproducible as shown by duplicated experiments. The two regions overlapped and a smooth continuous isotherm was obtained.

The available area of the balance for initial spreading of the film was of the order of 800 cm². Using the specific surface area, the larger quantity of polymer corresponds to an area of approximately 790 cm² and the smaller to an area of approximately 145 cm². The isotherm was, therefore, independent of the quantity of material used over this relatively

[1] This work was supported under a project sponsored by the Bureau of Naval Weapons, Department of the Navy.
[2] Howard University, Washington, D.C.

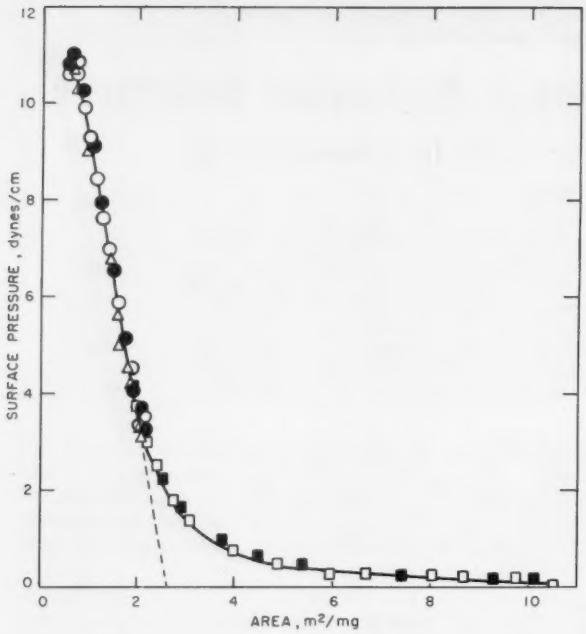

FIGURE 1. *Surface pressure-area isotherm of poly(ethylene adipate) spread from benzene at 24±0.5 °C.*

Distilled water subphase ○, ● 30.36×10^{-3} mg.
□, ■ 5.50×10^{-3} mg.
0.01 *N* HCl subphase △ 30.36×10^{-3} mg.

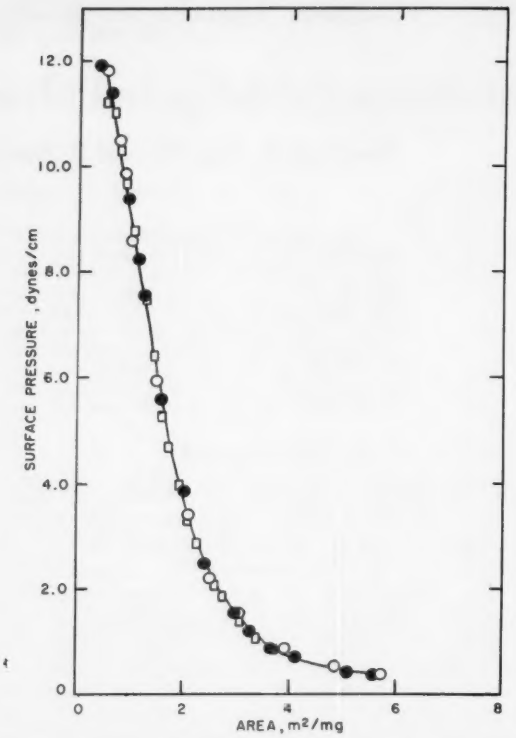

FIGURE 2. *Surface pressure-area isotherm of poly(ethylene adipate) on distilled water at 24±0.5 °C.*

Spread from benzene □ 17.51×10^{-3} mg.
Spread from chloroform ○, ● 12.12×10^{-3} mg.

wide range, which included a quantity near the maximum capacity of the balance. The absence of any change in the isotherm with quantity of material spread suggests that the films were completely spread and existed as monolayers. The use of 0.01 *N* HCl with a *p*H of 2 resulted in the same isotherm as the use of distilled water with a *p*H of 6.5. The collapse pressure of the films spread from benzene was 11.1 dynes per cm, as shown by figure 1. A quantity of polymer intermediate between the two amounts described above also resulted in the same isotherm as those spread from benzene, as shown in figure 2. Films spread from chloroform on distilled water also yielded the identical isotherm, but the collapse pressure was slightly higher, 12 dynes per cm.

The isotherm of poly(propylene adipate) spread from chloroform on distilled water is shown in figure 3. The properties for very dilute surface concentration were not studied for this film. The extrapolated specific area at zero surface pressure was 2.2 m²/mg. Films of this polymer did not collapse. Two quantities were again used to obtain different portions of the isotherm. These two sections overlapped and a smooth isotherm resulted. The spreading characteristics were, therefore, not dependent on the quantity of material deposited, within this range. The larger quantity, 29.94×10^{-3} mg, corresponded to an area of approximately 660 cm² at zero surface pressure, while the smaller quantity corresponded to one-half this amount. This independence on the amount of polymer suggests that the films were monolayers.

Poly(trimethylene adipate) was sensitive to the spreading solvent. Films spread from benzene on 0.01 *N* HCl subphase exhibited the surface characteristics shown by curve A in figure 4. A limiting area of 3.1 m²/mg was obtained from this isotherm. The quantity of polymer spread, 5.47×10^{-3} mg, corresponds to an area of approximately 170 cm², and because of the small quantity should represent a completely spread film.

The effect of the spreading solvent on the characteristics of the film is shown by isotherm B in figure 4. Polymer was spread from acetone solution in two different quantities onto a distilled water subphase. In one case 50λ ($\lambda=10^{-3}$ cm³) and in the other, 100λ were spread, using the same concentration of solution. Within the experimental error, both quantities resulted in the same isotherm, with a smaller specific area. The isotherm showed no signs of expansion to higher specific areas for the smaller quantity of solution spread. Repeat runs for both quantities resulted in the reproducible isotherm shown in figure 4. The fact that the maximum spreading area for the isotherm with the smaller amount of polymer was twice as large as that for the larger amount of polymer appears to indicate the spreading of the polymer with this solvent was complete.

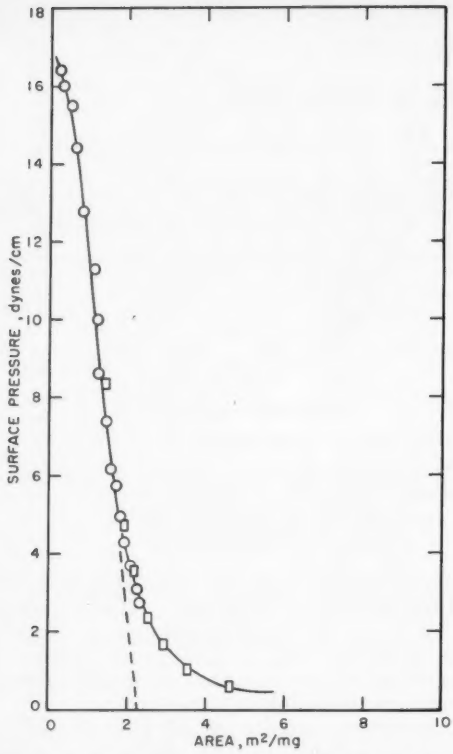

FIGURE 3. *Surface pressure-area isotherm of poly(propylene adipate) on distilled water spread from chloroform at 24.5 ±0.5 °C.*

○, 29.94×10⁻³ mg.
□, 14.95×10⁻³ mg.

4. Discussion

4.1. Physical Properties

In table 2 are given values for the thickness of the monolayers, the energies of compressing the films to collapse or the point of inflection, and compressibilities. The approximate thicknesses of the films were calculated from the bulk density and the limiting specific area of the completely spread film. As seen in table 2 they are within the range of 3 to 4 A and are of a reasonable thickness for monolayers. They fall in approximately the same range as did the succinate polyesters [1], and indicate that these polyesters lie relatively flat on the surface. Integration of the area under the isotherms from very large segment areas to the point of collapse for poly(ethylene adipate) and to the point of inflection for poly(propylene adipate) gives the energy to compress the film to a position of unstability. The energies shown in table 2 are rather high, one being of the order of 700 and the other 800 cal/mole/segment. For the succinate polyesters studied previously [1], only poly(neopentyl succinate) gave an energy above 700, as shown in table 2. Poly(ethylene succinate) gave an energy of 349, and poly(pentamethylene succinate) an energy of 568 cal/mole/segment. The compressibilities given in table 2 were calculated from the equation:

$$K=\frac{A_0-A_1}{A_0\pi_1}$$

where K is the compressibility, A_0 the extrapolated specific area at zero surface pressure, and A_1 the specific area at surface pressure π_1.

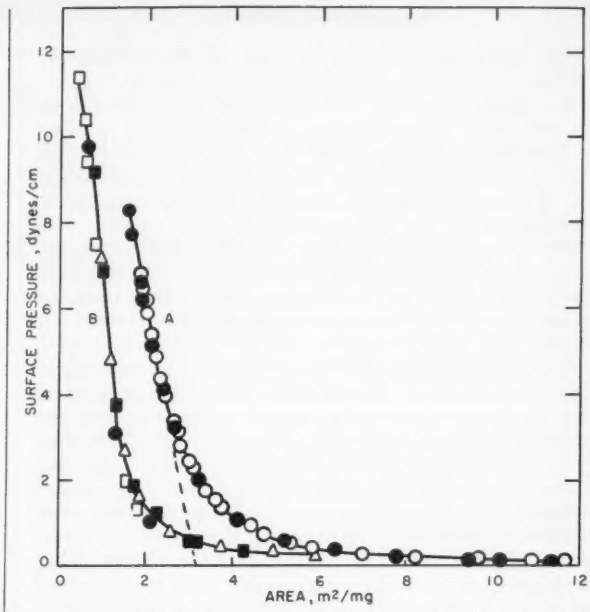

FIGURE 4. *Surface pressure-area isotherm of poly(trimethylene adipate) at 24±0.5°C.*

Curve A Spread from benzene on 0.01 *N* HCl subphase
○, ● 5.47×10⁻³ mg.
Curve B Spread from acetone solution on to distilled water subphase
□, ● 23.39×10⁻³ mg.
■, △ 11.70×10⁻³ mg.

TABLE 2

Polymer	Extrapolated specific area	Area per segment		Energy to compress film to collapse, cal mole⁻¹ segment⁻¹	Compressibility	Thickness at $\pi=0$
		Calculated	Observed			
	m^2/mg	A^2	A^2		$cm/dyne$	A
Poly(ethylene adipate)	2.6	67	75	716	0.067	3.0
Poly(propylene adipate)	2.2	67	68	807	.048	3.8
Poly(trimethylene adipate)	3.1	74	98	-------	.058	2.7
Poly(ethylene succinate)[a]	2.3	55	60 to 70	349	.11	3.1
Poly(pentamethylene succinate)[a]	2.9	74	90	568	.056	2.9
Poly(neopentyl succinate)[a]	2.0	60	63	734	.028	3.9

[a] Reference [1].

4.2. Compressibility

The compressibility values for all the polyesters studied, except for poly(ethylene succinate) [1], are in the range observed for linear polyesters, such as the self ester of the hydroxydecanoic acid studied by Harkins, Carmen, and Ries [2], and poly(vinyl acetate) films studied by Ries, Ahlbeck, and Gabor [4]. The latter polymer contains the ester groups as side chains.

The compressibility data for the adipate monolayers and the succinate monolayers, as reported previously, point to the general observation that the compressibility of the monolayer decreases with the number of carbon atoms in the glycol and acid groups and also with the arrangement of these groups.

Second, it is to be observed that the polyesters with the lower number of carbon atoms between the carboxylic groups have greater compressibilities than those with large numbers, as evidenced by comparison of the compressibilities of poly(ethylene succinate) with poly(ethylene adipate). Similarly the compressibilities of polyesters containing the ethylene glycol grouping have greater compressibilities than those having segments of longer glycols. This is evidenced by a comparison of poly(ethylene adipate) with poly(trimethylene adipate) as well as a comparison of poly(ethylene succinate) with poly(pentamethylene succinate).

Third, it appears that differences in the arrangement of the carbon atoms in the glycol chain also affects the compressibility. Thus, poly(propylene adipate) and poly(trimethylene adipate) differ in their compressibilities in that the branched three carbon group has a lower compressibility than the straight chain arrangement. Similar behavior is observed in a comparison of poly(neopentyl succinate) with poly(pentamethylene succinate).

The spreading of polymer films has been shown by others [2, 5] to be independent of molecular weight. Crisp [5] has shown that polymer films are completely spread when the specific areas are reproducible and independent of the solvent or solution concentration over a moderate concentration range. The spreading of both poly(ethylene adipate) and poly(propylene adipate) were independent of the quantity of material spread, over the concentration range studied, as shown in figures 1 to 3. As completely spread films are assumed to be independent of molecular weight, the surface pressure was plotted as a function of the area of the repeating structural unit. Such isotherms for the three polyesters are given in figure 5. Experimental points from different runs are given on each curve, except those of poly(trimethylene adipate) spread from acetone.

There is a large difference in the isotherm of poly(ethylene adipate), as shown in curve C, figure 5, and that of poly(ethylene succinate) (fig. 5, ref. 1). The increase in the length of the repeating unit by the addition of two methylene groups in the acid changed the collapse pressure from approximately 4 dynes/cm for the succinate to approximately 12 dynes/cm for the adipate polymer. This is very likely due to the greater freedom of orientation of

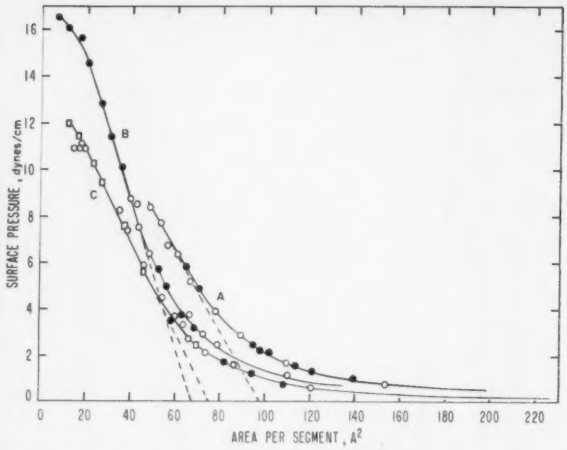

FIGURE 5. *Surface pressure-area isotherms of linear saturated polyesters on aqueous subphases at 24.5±0.5 °C.*
Curve A Poly(trimethylene adipate)
Curve B Poly(propylene adipate)
Curve C Poly(ethylene adipate)

the carbonyls in the interface, resulting in a higher vertical component of the dipole. The extrapolated segment area for the adipate polymer is 75 A^2 and 60 to 70 A^2 for the succinate polymer. These values are somewhat larger than the minimum calculated from molecular models.

The monolayer properties of poly(trimethylene adipate) spread from benzene, curve A, are similar to those of poly(ethylene adipate), curve C, at moderate surface pressures. At all surface pressures studied the segment areas are larger for the poly(trimethylene adipate) than for the poly(ethylene adipate). The extrapolated segment area of 98 A^2 is 23 A^2 larger than the value obtained for the poly(ethylene adipate) which is in good agreement with the cross-sectional area of a long chain hydrocarbon, as established by monolayer measurements.

5. Summary

Differences in the surface pressure—area isotherms of the three adipate polyesters studied were found to be related to differences in the chemical structure. Large differences were also observed between these polyesters and succinate polyesters studied previously. A large difference was observed between the observed and the calculated specific area for the repeating unit of poly(trimethylene adipate). As in the case of the succinate polyesters, one of the adipate polyesters studied did not collapse at high pressures.

6. References

[1] W. M. Lee, J. L. Shereshefsky, and R. R. Stromberg, J. Research NBS **65A** (Phys. and Chem.) No. 1, 51 (1961).
[2] W. D. Harkins, E. F. Carmen, and H. E. Ries, Jr., J. Chem. Phys. **3,** 692 (1935).
[3] S. A. Moss, Jr., J. Am. Chem. Soc. **56,** 41 (1934).
[4] H. E. Ries, Jr., R. A. Ahlbeck, and J. Gabor, J. Colloid Sci. **14,** 354 (1959).
[5] D. J. Crisp, J. Colloid Sci. **1,** 49 (1946).

(Paper 66A5–178)

JOURNAL OF RESEARCH of the National Bureau of Standards—A. Physics and Chemistry

Vol. 66A, No. 5, September–October 1962

Publications of the National Bureau of Standards*

Correction

In the July–August 1962 issue of this Section, the abstract for the paper **Low Temperature Thermometry,** R. P. Hudson, *Book, Experimental Cryophysics, pp. 214–253 (Butterworth & Co., London, England, 1961),* was presented incorrectly. The following abstract refers to this paper:

The principal methods for thermometry in the range 1°K to 90°K are critically reviewed, the discussion covering the physical principles involved, types of apparatus, and factors determining the attainable precision and accuracy. Supplementary data are provided in tables, some within the body of the article and others in appendices to the volume of which the article constitutes a chapter.

Selected Abstracts

Spark-gap flashover measurements for steeply rising voltage impulses, J. H. Park and H. N. Cones, *NBS J. Research* **66C** *(Eng. & Instr.) No. 3, 197 (July–Sept. 1962).*
Dividers made up of special thin ribbon resistors with very low time constants were used for measuring linearly rising chopped impulses with peak voltages up to 300 kv and times to sparkover from 0.03 to 50 microseconds. Total errors were deduced by a combination of computation and experimentation to be probably not greater than 1.5 percent for times to sparkover greater than 0.1 microsecond.

From a large number of oscillograph records data were derived giving a relation between rate of rise (or rise time) and flashover voltage for (1) 12.5 cm diameter spheres spaced 6 cm apart, (2) 25 cm diameter spheres spaced 6 cm, and (3) uniform field electrodes spaced 5 cm. It is recommended that the volt-time curve showing these relations for the 25 cm diameter spheres be used as a reference standard for interlaboratory comparison of measurement methods.

A furnace for thermocouple calibrations to 2,200° C, D. B. Thomas, *NBS J. Research* **66C** *(Eng. & Instr.) No. 3, 255 (July–Sept. 1962).*

A tantalum tube furnace has been constructed to calibrate and investigate the thermoelectric behavior of high temperature thermocouples. The furnace and its associated equipment were designed with emphasis on features that would assure a high degree of accuracy in measurements that are made at high temperatures and also with emphasis on trouble-free performance. Data that were obtained during furnace operation showed that thermocouple depth of immersion into a properly designed blackbody is of considerable importance if a good agreement is to be realized between a calibrated optical pyrometer and a calibrated thermocouple that has been placed in the hot zone of the furnace. High purity helium gas can be used in the furnace to keep thermocouple contamination to a minimum.

Method of measuring emissivities of metals in the infrared, A. G. Maki and E. K. Plyler, *NBS J. Research* **66C** *(Eng. & Instr.) No. 3, 283 (July–Sept. 1962).*

A method of measuring normal spectral emissivities in the infrared region from 1 to 13 μ is described. It consists of comparing the rate of emission of radiant energy from a blackbody with that from the specimen. The two observed radiances are made equal by adjusting the temperatures. An equation is derived for use in calculating the emissivity for the observed temperatures. The main sources of error arise in the measurement of the temperature of the specimen and the temperature of the blackbody. As an example of the method, the normal spectral emissivity of gold has been measured in the spectral range from 4 to 13 μ with temperatures from 550 to 1,000 °K. The emissivity was found to range from 0.014 at 4 μ and 550 °K to 0.0256 at 9 μ and 1,000 °K. A table is included which lists the values of emissivity from 4 to 13 μ and from 550 to 1,000 °K at intervals of 50 °K.

Tables of spectra-line intensities. Part I. Arranged by elements, W. F. Meggers, C. H. Corliss, and B. F. Scribner, *NBS Mono. 32, Pt. I (Dec. 29, 1961) $4.00.*
The relative intensities, or radiant powers, of 39,000 spectral lines with wavelengths between 2000 and 9000 Angstroms have been determined on a uniform energy scale for seventy chemical elements. This was done by mixing 0.1 atomic percent of each element in powdered copper, pressing the powder-mixture to form solid electrodes which were burned in a 10 ampere 220 volt direct-current arc, and photographing the spectra with a stigmatic concave grating while a step sector was rotating in front of the slit. The sectored spectrograms facilitated the estimation of intensities of all element lines relative to copper lines which were then calibrated on an energy scale provided by standardized lamps and all estimated line intensities were finally adjusted to fit this calibration. Comparisons with other intensity measurements in individual spectra indicate that the National Bureau of Standards spectral-line intensities may have average errors of 20 percent, but first of all they provide uniform quantitative values for the seventy chemical elements commonly determined by spectrochemists. These data are presented by element in part I and all 39,000 observed lines are given in order of wavelength in part II.

Analysis of coaxial two-terminal conical capacitor, M. C. Selby, *NBS Mono. 46 (Apr. 6, 1962) 20 cents.*
Adjustable capacitors having electrodes in the form of coaxial cones or frustums have been used on rare occasions in the past; but their potential superiority to other types of capacitors for some important applications have been overlooked. The advantage of this geometry over cylindrical or disk forms is that the practical capacitance range is several times larger. An example cites the capacitance ranges of a disk, cylindrical, and conical type to be 10, 40, and 168 to one, respectively. An approximate equation was derived for this conical capacitor and close agreement is shown between computed and measured values of capacitance versus electrode displacement. Multiple cone and different shape electrodes are suggested to obtain large values of capacitance with an appreciable saving of space and further increased range of capacitance. The electric field is plotted and its construction steps for axial symmetry are given.

Dissociation constant of 2-ammonium-2-methyl-1, 3-propanediol in water from 0 to 50° and related thermodynamic quantities, H. B. Hetzer and R. G. Bates, *J. Phys. Chem.* **66,** *308–311 (1962).*

The base 2-amino-2-methyl-1,3-propanediol, like the closely related compound tris-(hydroxymethyl)-aminomethane, is a solid substance of considerable use as a biological buffer material. The acidic dissociation constant, K_{bh}, of the substituted ammonium ion conjugate to the free base now has been determined at 11 termperatures from 0 to 50° by measurement of the electromotive force of hydrogen-silver chloride cells without liquid junction. The results are given as a function of the temperature (T) in °K. by the equation $-\log K_{bh} = 2952.00/T - 2.2652 + 0.0039092T$. The standard changes of free energy, enthalpy, entropy and heat capacity for the dissociation process have been calculated from the temperature coefficient of the dissociation constant. For the acidic dissociation of 2-ammonium-2-methyl-1,3-propanediol at 25°, the following results were obtained: $\triangle G^0 = 50{,}238$ j. mole^{-1}, $\triangle H^0 = 49{,}860$ j. mole^{-1}, $\triangle S^0 = -1.3$ j. deg.$^{-1}$ mole^{-1}, and $\triangle C_p{}^0 = -45$ j. deg.$^{-1}$ mole^{-1}. For the basic dissociation of 2-amino-2-methyl-1,3-propanediol at 25°, the corresponding quantities are $\triangle G^0 = 29{,}656$ j. mole^{-1}, $\triangle H^0 = 6720$ j. mole^{-1}, $\triangle S^0 = -76.9$ j. deg.$^{-1}$ mole^{-1}, and $\triangle C_p{}^0 = -150$ j. deg.$^{-1}$ mole^{-1}.

Study of electronically excited hydroxyl radicals in the $H+O_3$ atomic flame, H. P. Broida, *J. Chem. Phys.* **36,** *No. 2, 444–448 (Jan. 1962).*

Ultraviolet emission of the $A^2\Sigma^+ \rightarrow X^2\Pi_i$ transition of OH has been observed in low-pressure flames of hydrogen atoms and ozone. In these flames, at pressures near 1 mm Hg, the intensity of this uv emission was found to be directly proportional to the square of the intensity of the rotation-vibration bands in the electronic ground state, $^2\Pi_i$. Under similar conditions, reactions of hydrogen atoms with oxygen atoms or with hydroxyl radicals were found to give too little emission to account for the observed radiation. It is concluded that collisions of two vibrationally excited OH radicals, $^2\Pi_i$, lead to the electronically excited radicals, $^2\Sigma^+$. Approximately 500 photons are emitted by all the vibrationally excited radicals ($v=1$ to 9, $^2\Pi_i$) for each photon emitted in the electronic transition $A\ ^2\Sigma^+ \rightarrow X\ ^2\Pi_i$. Steady state partial pressures of vibrationally excited OH, $^2\Pi_i$, are estimated to be 10^{-7} mm Hg for a total flame pressure of 1 mm.

Theory of thermal diffusion in dilute alloys, R. E. Howard and J. R. Manning, *J. Chem. Phys.* **36,** *No. 4, 910–916 (Feb. 1962).*
A kinetic analysis is made of the thermal diffusion of a dilute impurity in an f.c.c. metal. Expressions are derived for the impurity current, the steady-state Soret gradient, and the mean atom displacement. It is shown how the "heats of transport" appearing in these expressions can be studied experimentally. An extension of the analysis to cases of nonthermal type gradients, in particular, a chemical concentration gradient, is briefly considered.

Hydrogen formation in the gamma-radiolysis of ethylene, P. Ausloos and R. Gorden, Jr., *J. Chem. Phys.* **36,** *No. 1, 5–9 (Jan. 1962).*
The radiolysis of ethylene-d_2 and C_2H_4-C_2D_4 mixtures has been investigated in the gas, liquid, and solid phases. The data indicate that hydrogen may be formed by two distinct molecular-elimination processes: $CH_2CH_2 \rightarrow CH_2C + H_2$ and $CH_2CH_2 \rightarrow CH \equiv CH + H_2$. The effect of xenon and pressure on the yields of H_2, HD, and D_2 in the gas-phase radiolysis of CH_2CD_2 has been investigated. The results for the $(^3P_1)$Hg-sensitized and the 1237 A-photochemical decomposition have been compared with those for radiolysis.

Impurity effects in high purity metal, L. L. Wyman and G. A. Moore, **(Symp. Major Effects of Minor Constituents on the Properties of Materials. Sixty-fourth Annual Meeting ASTM, Atlantic City, N.J. June 26, 1962),** *ASTM Spec. Tech. Publ. No. 304—ASTM Materials Sci. Series 2, 3–16 (June 26, 1961).*
Obtaining metals of the highest possible degree of purity is a problem of major concern in both science and engineering. The determination of impurities, their effects, and control, demand extreme efforts in processing and analysis. Impurities in metals are characterized by the nature of their occurrence and their effects on host metals. Specific examples illustrate impurity effects in a number of currently important applications.

Vibration-rotation interactions in cyanamide; the question of planarity of amides, D. R. Lide, Jr., *J. Mol. Spectroscopy* **8,** *No. 2, 142–152 (Feb. 1962).*
The cyanamide molecule is approximated by a simple model which allows for a large-amplitude out-of-plane vibration of the NH_2 group. The kinetic energy of this model is derived, and the quantum-mechanical problem is formulated. Perturbation expressions suitable for the case where there is a potential hump in the planar configuration are given. Some of the consequences of the vibration-rotation interactions are discussed.

Vacuum ultraviolet photochemistry. III. Primary processes in the vacuum ultraviolet photolysis of water and ammonia, J. R. McNesby, I. Tanaka, and H. Okabe, *J. Chem. Phys.* **36,** *No. 3, 605–607 (Feb. 1962).*
Water and ammonia have each been photolyzed in the absence and presence of C_2D_4 which served to scavenge H atoms. Wavelengths used were: for ammonia, 1849 and 1236 A; for water, 1236 A. Under conditions where H atoms are efficiently scavenged by C_2D_4, the production of H_2 signifies a primary photochemical process giving molecular H_2 directly. It is found that at 1849 A, ammonia decomposes almost entirely to $H + NH_2$. At 1236 A, two primary processes are observed.

$$NH_3 \rightarrow H_2 + NH, \quad \text{(a)}$$
$$NH_3 \rightarrow H + NH_2. \quad \text{(b)}$$

Process (a) is about $\frac{1}{3}$ as probable as process (b). At 1236 A, the photolysis of water proceeds via two primary processes.

$$H_2O \rightarrow H + OH, \quad \text{(c)}$$
$$H_2O \rightarrow H_2 + O. \quad \text{(d)}$$

The probability of process (c) being three times that of process (d). It is suggested that primary process (d) constitutes a reasonable photochemical mechanism for hydrogen formation in the earth's upper atmosphere.

Accuracy of analytical procedures, W. J. Youden, *J. Assoc. Official Agricultural Chemists* **45,** *No. 1, 160–173 (Feb. 1962).*
Most analytical chemistry procedures are expected to give correctly, except for random analytical errors, the amount present. This means that if the amounts found are plotted against the amounts present, the points should lie closely along the line $y=x$ where y is the amount found for a material containing amount x. Some procedures may recover only a constant percentage of the amount present and the best fitting line would be of the form $y=bx$. Other procedures may be subject to a constant error and the appropriate line would correspond to the equation $y=a+x$. A simple statistical technique is described that may be used to ascertain whether the data constitute evidence that the theoretical line, $y=x$, does not adequately represent the relationship between the amount taken and the amount found.
Some remarks on round robins are included.

Other NBS Publications

Journal of Research 66B (Math. & Math. Phys.) No. 2 (Apr.–June 1962) 75 cents.
Hindsight technique in machine translation of natural languages. I. Rhodes and F. L. Alt.
An extension of Jensen's theorem for the derivative of a polynomial and for infrapolynomials. O. Shisha.
Two matrix eigenvalue inequalities. S. Haber.
Graphs for determining the power of Student's *t*-test. M. C. Croarkin.

Journal of Research 6B (Math. & Math. Phys.) No. 3 (July–Sept. 1962) 75 cents.
The first run preceded by a quota. A. J. Goldman and B. K. Bender.
Two theorems on matrices. Morris Newman.
Mill's ratio for multivariate normal distributions. I. R. Savage.
Angle as a fourth fundamental quantity. J. E. Romain.
Invalidity of Meixner's theorem in irreversibile thermodynamics. R. E. Nettleton.
Selected bibliography of statistical literature, 1930 to 1957: VI. Theory of estimation and testing of hypotheses, sampling distributions, and theory of sample surveys. L. S. Deming.

Journal of Research 66C (Eng. & Instr.) No. 3 (July–Sept. 1962) 75 cents.
Measurement of longitudinal spherical aberration in the extra-axial region of lenses. F. E. Washer and W. R. Darling.
Spark-gap flashover measurements for steeply rising voltage impulses. J. H. Park and H. N. Cones. (See above abstracts.)
Evaporated-film electric hygrometer elements. F. E. Jones.
Methods of measuring the resistivities of anisotropic conducting media in situ. S. Rush.
Corrosion of steel pilings in soils. M. Romanoff.
Corrosion rates of ferrous alloys (Fe-Cr and Fe-Cr-Si) measured by polarization technique. W. J. Schwerdtfeger.
A furnace for thermocouple calibrations to 2,200 °C. D. B. Thomas. (See above abstracts.)

Total hemispherical emittance of coated and uncoated Inconel and types 321 and 430 stainless steel. J. C. Richmond and W. N. Harrison.
"Mail Separator" control computer preliminary logical design. S. Henig and E. C. Palasky.
Method of measuring emissivities of metals in the infrared. A. G. Maki and E. K. Plyler. (See above abstracts.)

Journal of Research 66D (Radio Prop.) No. 5 (Sept.–Oct. 1962) 70 cents.
Theory of magneto-telluric fields. J. R. Wait.
Propagation characteristics of magneto-ionic plasma columns. D. Formato and A. Gilardini.
Dielectric loading of electric dipole antennas. J. Galejs.
Possible influence of the ionosphere on the impedance of a ground-based antenna. J. R. Wait.
Some statistical theory for the analysis of radio propagation data. M. M. Siddiqui.
Auroral sporadic-*E* ionization. R. D. Hunsucker and L. Owren.
Comparative study of the correlation of seasonal and diurnal cycles of transhorizon radio transmission loss and surface refractivity. B. R. Bean.
Enhancement of the lunar tide in the noon critical frequency of the F_2 layer over the magnetic equator. R. G. Rastogi.
Scattering from a conducting sphere embedded in a semi-infinite dissipative medium. J. Galejs.
High-frequency scattering from a coated sphere. V. H. Weston and R. Hemenger.
Propagation of spherical waves through an ionosphere containing anisotropic irregularities. K. C. Yeh.

Radiation patterns in the lower ionosphere and Fresnel zones for elevated antennas over a spherical earth, R. G. Merrill and W. V. Mansfield, NBS Mono. 38 (April 2, 1962) 70 cents.
Effect of exposure site on weather resistance of porcelain enamels exposed for three years, D. G. Moore and A. Potter, NBS Mono. 44 (April 10, 1962) 15 cents.
Fire tests of precast cellular concrete floors and roofs, J. V. Ryan and E. W. Bender, NBS Mono. 45 (April 12, 1962) 15 cents.
An ultraviolet multiplet table, C. E. Moore, NBS Circular 488, Sections 3, 4, and 5 (April 6, 1962) Section 3, 60 cents; Section 4, 45 cents; Section 5, 30 cents.
Mean electron density variations of the quiet ionosphere—September 1959, J. W. Wright, L. R. Wescott, and D. J. Brown, NBS Tech. Note 40–7 (PB151399–7) (1962) $1.50.
Mean electron density variations of the quiet ionosphere No. 13; Summary of one year of data, May 1959—April 1960, J. W. Wright, NBS Tech. Note 40–13 (PB151399–13) (1962) $1.50.
Bibliography on auroral radio wave propagation, W. Nupen, NBS Tech. Note 128 (PB161629) (1962) $2.75.
Airborne television coverage in the presence of co-channel interference, M. T. Decker, NBS Tech. Note 134 (PB161635) (1962) $2.00.
Ionosonde observations of artificially produced electron clouds: Firefly 1960, J. W. Wright, NBS Tech. Note 135 (PB161636) (1962) $2.50.
Some problems of fatigue of bolts and bolted joints in aircraft applications, L. Mordfin, NBS Tech. Note 136 (PB161637) (1962) $1.25.
A bibliography of the thermophysical properties of oxygen at low temperatures, J. C. Hust, L. D. Wallace, J. A. Crim, L. A. Hall, and R. B. Stewart, NBS Tech. Note 137 (PB161638) (1962) $2.25.
Vertical cross sections of the ionosphere across the geomagnetic equator, J. W. Wright, NBS Tech. Note 138 (PB161639) (1962) $1.00.
Siting criteria for HF communication centers, W. F. Utlaut, NBS Tech. Note 139 (PB161640) (1962) $1.25.
Atlas of Fourier coefficients of diurnal variation of f_0F_2, W. B. Jones, NBS Tech. Note 142 (PB161643) (1962) $2.50.
Numerical results for the surface impedance of a stratified conductor, C. M. Jackson, J. R. Wait, and L. C. Walter, NBS Tech. Note 143 (PB161644) (1962) $1.25.
Cryogenic temperature measurement with platinum resistance thermometers—Is fixed-point calibration adequate? R. J. Corruccini, NBS Tech. Note 147 (PB161648) (1962) 50 cents.
An introduction to flame photometry and a review of recent studies, M. Margoshes, Phys. Tech. Biological Research **4,** 215–260 (1962).
Congruences for the partition function to composite moduli, M. Newman, Illinois J. Math. **6,** No. 1, 59–63 (Mar. 1962).
Research and the saving of teeth, G. C. Paffenbarger, J. Prostetic Dentistry **12,** No. 2, 369–383 (Mar.-Apr. 1962).
Displacement and strain-energy distribution in a longitudinally vibrating cylindrical rod with a viscoelastic coating, P. Hertelendy, J. Appl. Mech. Trans. ASME **29,** Series E, No. 1, 47–52 (Mar. 1962).
Properties of silico-phosphate cements, J. N. Anderson and G. C. Paffenbarger, Dental Progress **2,** No. 2, 72–75 (Jan. 1962).
Comments on paper by W. D. Westfall, "Prediction of VLF diurnal phase changes and solar flare effect," J. R. Wait, J. Geophys. Research **67,** No. 2, 916–917 (Feb. 1962).
The shape of the geomagnetic field boundary under uniform external pressure, R. J. Slutz, J. Geophys. Research **67,** No. 2, 505–513 (Feb. 1926).
Plating standards and specifications, F. Ogburn, Electroplating Eng. Handb. 2d. ed., Ed. K. Graham, ch. **7,** p. 257–262 (Reinhold Publ. Co., New York, N. Y., 1962).
Surface effect on bond strength of steel beams embedded in concrete, J. O. Bryson and R. G. Mathey, J. Am. Concrete Inst. **59,** No. 3, 397–406 (Mar. 1962).
Inequalities for the permanent function, M. Marcus and M. Newman, Ann. Math. **75,** No. 1, 47–62 (Jan. 1962).
Effect of monomeric reagents on the melting (contraction) and recrystallization of fibrous proteins, L. Mandelkern, W. T. Meyer, and A. F. Diorio, J. Phys. Chem. **66,** 375–376 (1962).
A correction to the exospheric electron density estimate using the nose whistlers of March 19, 1959, J. H. Pope, J. Geophys. Research **67,** No. 1, 412 (Jan. 1962).
Investigation of the spectrophotometric method of measuring the ferric ion yield in the ferrous sulfate dosimeter, K. Scharf and R. M. Lee, Radiation Research **16,** No. 2, 115–124 (Feb. 1962).
Microwave spectrum and nonplanarity of cyanamide, D. J. Millen, G. Topping, and D. R. Lide, Jr., J. Mol. Spectroscopy **8,** No. 2, 153–163 (Feb. 1962).
Long-distance one-hop F_1 propagation through the auroral zone, L. H. Tveten, J. Geophys. Research **66,** No. 6, 1683–1684 (June 1961).
Preparation of and electroplating of uranium, D. E. Couch, Plating **49,** No. 4, 363–367 (Apr. 1962).
Tensile strength and modulus of elasticity of tooth structure and several restorative materials, R. L. Bowen and M. S. Rodriguez, J. Am. Dental Assoc. **64,** No. 3, 378–387 (Mar. 1962).
Vacuum microbalance techniques, R. F. Walker, Editor, Volume **2,** 179 pages, Proc. Conf. at the National Bureau of Standards, Apr. 20–21, 1961 (Plenum Press, New York, N. Y., 1962).
First pulsed radio soundings of the topside of the ionosphere, R. W. Knecht and T. E. Van Zandt, J. Geophys. Research **66,** No. 9, 3078–3081 (Sept. 1961).
Cryogenics and nuclear physics, R. P. Hudson, Science **134,** 1733–1736 (Dec. 1961).
Vacuum ultraviolet photochemistry. II. Photolysis of ethylene, H. Okabe and J. R. McNesby, J. Chem. Phys. **36,** No. 3, 601–604 (Feb. 1962).
Experimental study of the stark broadening of the balmer lines H_γ, W. L. Wiese, D. R. Paquette, and J. E. Solarski, Proc. Fifth Intern. Conf. Ionization Phenomena in Gases, Munich, pp. 907–912 (North Holland Publ. Co., Amsterdam, The Netherlands, 1961).
Internal magnetic fields in nickel-rich nickel-cobalt alloys, L. H. Bennett and R. L. Streever, Jr., J. Appl. Phys. Suppl. **33,** No. 3, 1039–1094 (Mar. 1962).
Strong blast waves in spherical, cylindrical and plane shocks, D. L. Jones, Phys. of Fluids **4,** No. 9 (Sept. 1961).
Approximations to the moments of the sample median, M. M. Siddiqui, Ann. Math. Stat. **33,** No. 1, 157–168 (Mar. 1962).

Kinetic equation for plasmas with collective and collisional correlations, C. M. Tchen, Proc. Fifth Conf. on Ionization Phenomena in Gases, Munich, pp. 825–841 (North Holland Publ. Co., Amsterdam, The Netherlands, 1961).

Plasma with net charge, J. L. Jackson, D. B. Levine, and R. A. Piccirelli, Phys. of Fluids **5,** No. 2, 250–251 (Feb. 1962).

Solubility product phenomena in hydroxypatite-water systems, H. M. Rootare, V. R. Deitz, and F. G. Carpenter, J. Colloid. Sci. **17,** No. 3, 179–206 (Mar. 1962).

Worldwide patterns of ionospheric blackout occurrence, V. Agy and K. Davies, J. Atmospheric and Terrest. Phys. **23,** 202–205 (Dec. 1961).

Fluorescence and rotational relaxation of OH radicals in flames, T. Carrington, Eighth Symp. (Intern.) on Combustion, pp. 257–262 (The Williams & Wilkins Co., Baltimore, Md., 1960).

Refraction effects of large-scale ionospheric irregularities observed at Boulder, Colorado, R. S. Lawrence and J. L. Jespersen (Proc. 2d Intern. Space Science Symp., Florence, Italy, Apr. 10–14, 1961), Space Research II, 258–276 (North Holland Publ. Co., Amsterdam, The Netherlands, Apr. 1961).

Physical properties of 113 domestic marbles, A. Hockman, Architectural Record, pp. 192–193 (Apr. 1962).

On the nature of equatorial slant sporadic *E*, R. Cohen, K. L. Bowles and W. Calvert, J. Geophys. Research **67,** No. 3, 965–972 (Mar. 1962).

A survey of carbon-carbon bond lengths, D. R. Lide, Jr., Tetrahedron **17,** 125–134 (1962).

I. Strange sounds in the atmosphere, R. K. Cook, Sound-Its Uses and Control **1,** No. 2, 12–16 (Mar–Apr. 1962).

An aluminum magnet cooled with liquid hydrogen, J. R. Purcell, Proc. Intern. Conf. on High Magnetic Fields, Mass. Inst. Tech., Cambridge, Mass., Nov. 1–4, 1961, pp. 166–169 (Mass. Inst. Tech. Press, Cambridge, Mass., and John Wiley & Sons, Inc., New York, N.Y., 1962).

Possible solar flare effects in the *F* region of the ionosphere, R. W. Knecht and K. Davies, Nature **192,** No. 4800, 347–348 (Oct. 1961).

Microwave structure determinations on tertiary butyl acetylene and tertiary butyl cyanide, L. J. Nugent, D. E. Mann, and D. R. Lide, Jr., J. Chem. Phys. **36,** No. 4, 965–971 (Feb. 1962).

Static dielectric constant of rutile (TiO_2), 1.6–1060 °K, R. A. Parker, Phys. Rev. **124,** No. 6, 1719–1722 (Dec. 1961).

Translational energy accommodation in the nickel-chlorine surface reaction, J. D. McKinley, J. Phys. Chem. **66,** 554–555 (Mar. 1962).

Auroral-zone geomagnetic micropulsations with periods of 5 to 30 seconds, W. H. Campbell and S. Matshushita, J. Geophys. Research **67,** No. 2, 555–573 (Feb. 1962).

Some problems of color identification, K. L. Kelly, J. Am. Inst. Architects **37,** No. 3, 80–82 (Mar. 1962).

Lorentz corrections in rutile, R. A. Parker, Phys. Rev. **124,** No. 6, 1713–1719 (Dec. 1961).

Some observations of 2.89 Mc/s equivalent antenna temperatures at the auroral zone, C. G. Little, G. M. Lerfald, and R. Parthasarathy, J. Atmospheric and Terrest. Phys. **23,** 275–286 (Dec. 1961).

The structure of regions of coronal-line emission, J. T. Jefferies, C. W. Pecker, and R. N. Thomas, Astrophys. J. **135,** 653–655 (Mar. 1962).

A digital ray-tracing program for ionosphere research, R. S. Lawrence and D. J. Posakony, (Proc. 2d Intern. Space Science Symp., Florence, Italy, Apr. 10–14, 1961), Space Research **II,** 258–276 (North Holland Publ. Co., Amsterdam, The Netherlands, Apr. 1961).

Electrical properties of nonstoichiometric semiconductors, J. H. Becker and H. P. R. Frederikse, J. Appl. Phys. Suppl. **33,** No. 1, 447–453 (Jan. 1962).

Pulsed radio soundings of the topside of the ionosphere in the presence of spread *F*, R. W. Knecht and S. Russell, J. Geophys. Research **67,** No. 3, 1178–1182 (Mar. 1962).

Recent studies on rutile (TiO_2), H. P. R. Frederikse, J. Appl. Phys. Suppl. **32,** No. 10, 2211–2215 (Oct. 1961).

The resistive transition in Mb_3Sn, D. Cline, R. H. Kropschot, V. Arp, and J. H. Wilson, Proc. Intern. Conf. on High Magnetic Fields, Mass. Inst. Tech., Cambridge, Mass., Nov. 1–4, 1961, pp. 580–583 (Mass. Inst. Tech., Press Cambridge, Mass., and John Wiley & Sons, Inc., New York, N.Y., 1962).

Electronic conduction in rutile (TiO_2), H. P. R. Frederikse, W. R. Hosler and J. S. Becker, Proc. Intern. Conf. Semiconductor Phys., Prague, Czechoslovakia, pp. 868–871 (1960).

Structure and photodetachment spectrum of the atomic carbon negative ion, M. L. Seman and L. M. Branscomb, Phys. Rev. **125,** No. 5, 1602–1608 (Mar. 1962).

Modulated photoelectric measurement of vibration, V. A. Schmidt, S. Edelman, E. R. Smith and E. T. Pierce, J. Acoust, Soc. Am. **34,** No. 4, 455–458 (Apr. 1962).

A high mode tunable cavity for microwave-gas interactions, A. J. Estin, Rev. Sci. Instr. **33,** 369–371 (Mar. 1962).

Propagation of the low frequency radio signal, J. R. Johler, Proc. IRE 50, 404–427 (Apr. 1962).

**Publications for which a price is indicated (except for Technical Notes) are available only from the Superintendent of Documents, U.S. Government Printing Office, Washington 25, D.C. (foreign postage, one-fourth additional). Technical Notes are available only from the Office of Technical Services, U.S. Department of Commerce, Washington 25, D.C. (order by PB number). Reprints from outside journals and the NBS Journal of Research may often be obtained directly from the authors.*

U.S. GOVERNMENT PRINTING OFFICE:1962

UNIVERSITY MICROFILMS INC
EDITORIAL DEPARTMENT
313 NORTH FIRST ST
ANN ARBOR MICH
SJR-A OCT

UNITED ST
GOVERNMENT PRINTING OFFICE
DIVISION OF PUBLIC DOCUMENTS
WASHINGTON 25, D.C.

OFFICIAL BUSINESS

PENALTY FOR PRIVATE USE TO AVOID PAYMENT OF POSTAGE, $300 (GPO)

JOURNAL OF RESEARCH of the National Bureau of Standards Vol. 66A, No. 5 September–October 1962
A. Physics and Chemistry

Contents

Page

Calorimetric calibration of an ionization chamber for determination of X-ray total beam energy. John S. Pruitt and Steve R. Domen. 371

Zinc oxide as a standard substance in the solution calorimetry of portland cement. Edwin S. Newman. 381

Nuclear optical model analysis of neutron elastic scattering for calcium. Randall S. Caswell. 389

Pyrolysis of some polyvinyl polymers at temperatures up to 1,200 °C. Sidney Straus and Samuel L. Madorsky. 401

Lattice frequencies and rotational barriers for inorganic carbonates and nitrates from low temperature infrared spectroscopy. R. A. Schroeder, C. E. Weir, and E. R. Lippincott. 407

Foreign gas broadening of the lines of hydrogen chloride and carbon monoxide. Earle K. Plyler and Robert J. Thibault. 435

Monolayers of adipate polyesters at air-liquid interfaces. Wendell M. Lee, Robert R. Stromberg, and J. Leon Shereshefsky. 439

Publications of the National Bureau of Standards. 442

For sale by the Superintendent of Documents, U.S. Government Printing Office, Washington 25, D.C. Price 70 cents (single copy). Subscription price: $4 a year; 75 cents additional for foreign mailing.

UNITED STATES GOVERNMENT PRINTING OFFICE, WASHINGTON : 1962